

# REPORT DOCUMENT PAGE

Form Approved  
OMB NO. 0704-0188

Public reporting burden for this collection of information is estimated to average 1 hour per response, including the time for reviewing instructions, searching existing data sources, gathering and maintaining the data needed, and completing and reviewing the collection of information. Send comment regarding this burden estimate or any other aspect of this collection of information, including suggestions for reducing this burden to Washington Headquarters Services, Directorate for Information Operations and Reports, 1215 Jefferson Davis Highway, Suite 1204, Arlington, VA 22202-4302, and to the Office of Management and Budget, Paperwork Reduction Project (0704-0188), Washington, DC 20503.

1. AGENCY USE ONLY (LEAVE BLANK)		2. REPORT DATE AUGUST, 2001		3. REPORT TYPE AND DATES COVERED Final Progress Report: <del>Jul August</del> 1, 1998-June 30, 2001	
4. TITLE AND SUBTITLE Lateral Migration Radiography Image Signature for the Detection and Identification of Buried Land Mines				5. FUNDING NUMBERS  ARO Grant DAAG-55-98-1-0400	
6. AUTHORS Edward T. Dugan Alan M. Jacobs					
7. PERFORMING ORGANIZATION NAME(S) AND ADDRESS(ES) Department of Nuclear and Radiological Engineering 202 NSC, P.O. Box 118300 University of Florida Gainesville, FL 32611				8. PERFORMING ORGANIZATION REPORT NUMBER	
9. SPONSORING / MONITORING AGENCY NAME(S) AND ADDRESS(ES) U.S. Army Research Office P.O. Box 12211 Research Triangle Park, NC 27709-2211				10. SPONSORING / MONITORING AGENCY REPORT NUMBER  Proposal NO. 33830- <del>MA-LMD</del> <b>6-CI-LMD</b>	
11. SUPPLEMENTARY NOTES The views, opinions and/or findings contained in this report are those of the author(s) and should not be construed as an official Department of the Army position, policy or decision, unless so designated by other documentation.					
12A. DISTRIBUTION/AVAILABILITY STATEMENT  Approved for public release; distribution unlimited				12B. DISTRIBUTION CODE  AUG 29 2001	
13. ABSTRACT Lateral migration radiography (LMR), a new form of Compton Backscatter x-ray imaging, is applied to the detection and identification of buried land mines. Uncollimated detectors provide images that are due primarily to single-scatter photons from the soil surface or near-surface. Collimated detectors provide images that are due primarily to multiple-scatter photons from the near-surface or sub-surface. Noise removal and image enhancement techniques including simple weighted filters, Weiner filters, optimal filters and neural networks have been successfully employed on LMR images. Information from both the uncollimated and collimated detector images is used to effectively remove surface clutter and enhance mine detection and identification. An innovative rotating collimator for the x-ray source has been developed to provide rapid side-to-side scanning of the source beam without having to move the x-ray generator in this direction. Acquisition of detailed images of a 40 cm by 40 cm area takes under 30 seconds. The construction and testing of a portable LMR system for out door mine detection was completed. This system includes the x-ray generator; rotating source collimator; large area scintillator detectors; system frame assembly; motors and sensors for side-to-side and front-to-rear scanning; x-ray generator scan and data acquisition and processing systems; a standoff-to-vehicle IR modem communication system; and a portable electric generator power system. System weight (not including the vehicle) is about 160 kg, but this initial portable system has been significantly over-designed; system weight for a prototype should be in the range of 80 kg. Power requirement for this system can be as low as 150 watts and will not exceed 800 watts. This portable system successfully acquired images of mines buried in an indoor soil box and then in out-of-door tests conducted near the University of Florida campus. The system will be used on the Army land mine detection test lanes at Fort A.P. Hill in Virginia in August or September, 2001.					
14. SUBJECT TERMS LANDMINE DETECTION, COMPTON BACKSCATTER X-RAY IMAGING, LATERAL MIGRATION RADIOGRAPHY, IMAGE PROCESSING, SURROGATE LAND MINES, LANDMINE CONFIRMATION SENSOR, LAND MINE IDENTIFICATION				15. NUMBER OF PAGES <b>124</b>	
				16. PRICE CODE	
17. SECURITY CLASSIFICATION OR REPORT  <b>UNCLASSIFIED</b>	18. SECURITY CLASSIFICATION OF THIS PAGE  <b>UNCLASSIFIED</b>	19. SECURITY CLASSIFICATION OF ABSTRACT  <b>UNCLASSIFIED</b>	20. LIMITATION OF ABSTRACT  <b>UL</b>		

NSN 7540-01-280-5500

STANDARD FORM 298 (REV. 2-89)  
Prescribed by ANSI Std. Z39-18  
298-102

20011023 047

# **Lateral Migration Radiography Image Signatures for the Detection And Identification of Buried Land Mines**

**Final Technical Report  
ARO Grant Number  
DAAG-55-98-1-0400**

**By**

**Edward Dugan  
Alan Jacobs**

**DISTRIBUTION STATEMENT A**  
Approved for Public Release  
Distribution Unlimited

**NUCLEAR AND RADIOLOGICAL ENGINEERING DEPARTMENT  
UNIVERSITY OF FLORIDA  
Gainesville, FL 32611  
August, 2001**

## Table of Contents

Statement of Problem Studied .....	1
Summary of Important Results.....	3
List of Publications and Technical Reports.....	16
Scientific Personnel.....	17
Appendix I – Doctoral Dissertation: Fundamental Analysis and Algorithms for Development Of a Mobile Fast-Scan Lateral Migration Radiography System.....	18

### Statement of Problem Studied

A series of buried landmine detection measurements using a novel x-ray Compton backscatter imaging (CBI) method were performed at the University of Florida in 1998 using 12 actual antitank and antipersonnel mines. These tests were conducted indoors using a soil box and an old x-ray therapy machine for the x-ray source. The resulting images were stunning in their definitive detail. The signatures were so unique, that it was apparent that this approach could provide not only for reliable mine detection, but also for mine type identification. The mine's exterior shape, combined with the interior air volumes yield vivid, easily recognized signatures. The image data provides information on the mine size and shape, (x, y) location and depth-of-burial (DOB).

The new CBI method developed at the University of Florida and used to obtain the signatures of the live mines has been given the name lateral migration radiography (LMR). Unlike conventional CBI techniques which utilize only single-scatter photons, LMR uses both multiple- and single-scattered photons. LMR requires two types of properly configured detectors. Uncollimated detectors image primarily single-scatter photons while collimated detectors image predominately multiple-scatter photons. This allows for the generation of two separate sets of images, one containing primarily surface or near-surface features and the other also containing subsurface features. These two image sets make LMR useful for imaging and identifying objects to depths of several x-ray photon mean free paths (~10 cm) even in the presence of surface clutter.

The first task under this work was the purchase of a compact, high intensity, state-of-the-art, low-noise, DC x-ray generator to replace the old x-ray therapy machine. A related task was to develop special, large area scintillator detectors, including special compact photomultiplier tubes and associated electronics and combine these with the new x-ray generator to obtain an efficient LMR imaging system. A second task was to construct simulated or dummy mines that accurately mock up the internals of actual mines, including especially void spaces. Commercially available dummy mines, developed primarily for E&M methods, were poor surrogates for the LMR method because the casing materials used did not have a good match in atomic number, or Z, with the materials in actual mines.

The next task was to determine the effect of the angle of incidence with the soil of the x-ray source beam on mine signatures and image quality. Some of the work with the actual mines suggested that having the source beam strike the soil at an angle different than 90° could lead to enhanced images and to increased DOB for mine detection. To expedite this evaluation, Monte Carlo simulations were to be performed, in conjunction with experiments, to determine these effects. Experiments and Monte Carlo simulations were also to be used to establish limits and conditions under which LMR signatures can be used to detect and identify buried land mines.

An important task of this research was to develop an image processing approach or hierarchy for utilizing the multiple sets of LMR images for mine detection. A related task was the development of specialized LMR image processing, enhancement and target recognition algorithms. As a proof of principle of mine detection with LMR, a final task was the construction and testing, out-of-doors, of a portable LMR land mine detection system.

## Summary of Important Results

Lateral Migration Radiography (LMR), a new form of x-ray Compton backscatter imaging (CBI), is applied to the detection and identification of buried landmines. Unlike conventional CBI techniques which utilize only single-scatter photons, LMR uses both multiple- and single-scatter photons. The LMR imaging modality requires two types of properly configured detectors. Uncollimated detectors image primarily single-scatter photons while collimated detectors image predominantly multiple-scatter photons. This allows for the generation of two separate images, one containing primarily surface features and the other also containing sub-surface features. These two images make LMR useful for imaging and identifying objects to depths of several mean free paths (to about 10 cm for landmines in typical soils), even in the presence of unknown surface clutter.

A compact, high intensity, state-of-the-art x-ray generator was purchased from Lorad. The x-ray output range is 10 to 160 kV @ 0.1 mA to 5.0 mA with a 800 watt maximum power level. The optimal x-ray spectrum for mine detection in typical soils is 125 to 150 kVp. Consideration of the x-ray intensity requirement for good image contrast and desirable image acquisition times for the humanitarian de-mining application leads to an x-ray generator power level requirement of 100 to 200 watts. The new generator possesses good reproducibility and very little noise compared to the old medical therapy x-ray generator that was used previously to obtain LMR landmine images. Results with the Lorad x-ray generator show a significant improvement in LMR image quality compared to results obtained with the old generator.

Surrogate mines were purchased commercially. These mines were designed to simulate actual land mines in size, shape, and internal structural details. The emphasis on the materials used in these mines is to give mass densities and electrical properties similar to those of real mines. The electrical properties are of special importance for E&M methods of detection. For LMR detection, the proper size, shape, mass density and internal void details are all important. Also critical, however, is the atomic number,  $Z$ . The LMR images obtained using these commercially purchased surrogate mines were not consistent with the LMR image results obtained using the real mines. Some of the observed differences were suspected to be due to not having a good match in  $Z$ . Consequently, we had surrogate mines machined locally using acrylic (lucite-L) and acetal (delrin). These mines were designed to reproduce plastic mine characteristics essential for LMR imaging, including  $Z$ . LMR image results have shown that void spaces in mines are especially responsible for the unique signatures that allow for mine identification as well as detection. A detailed description of the work with the surrogate and simulated mines can be found in the Technical Report "Lateral Migration Radiography Image Signatures for the Detection and Identification of Buried Land Mines" (see Item 2 in the List of Publications and Reports) that was done under this research grant.

An image processing approach has been developed that makes use of the physics associated with the formation of the collimated and uncollimated detector images. Of great importance here are the different responses of the collimated and uncollimated detectors to given objects

or features. For buried objects, the front collimated detector image shows a shift to the rear and the rear collimated detector image shows a shift to the front. The magnitude of this shift is related to the object depth-of-burial (DOB). Surface-laid objects show no such shift in the collimated detector images. Objects in uncollimated detector images show no shifts, whether they are buried or surface-laid. Metal objects show intensity decreases relative to the soil in both detector type images and plastic mines show intensity increases relative to the soil in both detector type images. Potholes or large voids show an intensity increase in collimated detector images and an intensity decrease in uncollimated detector images. A negative slope in the soil surface yields and intensity decrease in the direction of motion in the uncollimated detector image and an intensity increase in the direction of motion in the collimated detector image. An adaptive logic is used that performs addition and/or subtraction of normalized sets of collimated and uncollimated detector images in a manner dictated by correlating the observed intensity behavior in the different images. The resulting image is then passed through a filter that maximizes the signal-to-noise ratio. This approach is very effective at removing surface clutter and/or slopes in the soil and in distinguishing mines from non-mine buried objects. A detailed description of this image processing approach, including image results, can be found in the Technical Report "Lateral Migration Radiography Image Signatures for the Detection and Identification of Buried Land Mines" (see Item 2 in the List of Publications and Reports) that was done under this research grant.

An innovative rotating collimator for the x-ray source beam was designed and constructed. The function of this collimator is to achieve side-to-side scanning motion for the beam without requiring any movement in this direction of the x-ray generator itself. Because this collimator simplifies the system movement required for image acquisition, there are reduced vibrations and stresses on the system, improved reproducibility in locating image pixels and faster image scanning speed. Monte Carlo simulations have identified distortions introduced by the rotating collimator in the acquired images; because these are known, they can be compensated for in the image processing software. With the rotating source collimator, a 40 cm by 40 cm soil region has been scanned and images acquired in 20 seconds. The power level was 650 watts. Good image quality can be achieved at 100 watts, but the scan time is then increased. For operation at 130 watts, the time required to scan a 40 cm by 40 cm soil area is 100 seconds, which is still good. The rotating source collimator is what allows LMR to achieve high speed image acquisition. A detailed description of the rotating source collimator can be found in the Technical Report "Lateral Migration Radiography Image Signatures for the Detection and Identification of Buried Land Mines" (see Item 2 in the List of Publications and Reports) that was done under this research grant.

To go along with the high speed scan capability that is achieved with the rotating source collimator, a high speed image display capability has been incorporated into the data acquisition system. This allows the image to be displayed, line-by-line, real-time, as it is acquired. This ability is useful so that a rapid decision can be made if it is necessary to rescan an area. A specialized LMR image processing and image enhancement package using Matlab has also been developed for post-processing data on a non real-time basis. The package includes standard, simple low pass filters, as well as a Weiner adaptive low pass filter; histogram equalization which can be useful for deep-buried mines when image contrast is low; linear combination

techniques which work with both the collimated and uncollimated detector images to remove surface features and/or identify types of buried objects on the basis of their different responses in the two different detector types; optimal filters which maximize signal-to-noise ratio in a specified region and can be useful for deep-buried mines; and neural networks which have been found useful both for removing surface-laid objects and for identifying deep-buried mines. The neural network used is a very simple, feed forward network that employed only three sets of images during the learning step. The success of this simple neural network is very encouraging and further efforts in this area should be very productive. A detailed description of the image processing and image enhancement package developed for this project can be found in the Technical Report "Image Processing Techniques for Lateral Migration Radiography Land Mine Images (see Item 5 in the List of Publications and Reports).

The final phase of this project included the development and testing of a portable LMR system for out-of door land mine detection. Components and systems include: 1) a rotating x-ray source collimator; 2) collimated and uncollimated scintillator detectors; 3) system frame assembly; 4) detector and x-ray generator support platform; 5) motors and sensors for side-to-side and front-to-rear scanning; 6) x-ray generator and data acquisition control and processing programs; 7) IR modem and communication programs for stand-off control of the system; and 8) a Honda generator power supply. The above items were first tested individually and then as an integrated system. This portable assembly was initially positioned over the indoor soil box and successfully used to acquire images of buried, simulated anti-personnel, anti-vehicle and anti-tank mines. The system was then tested out-of-doors for several weeks at a farm about 20 miles south of the University of Florida campus. Final out-of-door testing is expected to occur at Fort A.P. Hill in late August or September, 2001.

The overall dimensions of the portable system are about 2 m (from front to back) by about 1.8 m (from side to side) by about 1.4 m from top to bottom. The Unistrut steel support frame is about 2 m x 1m x 1m. The overall system weight is about 160 kg, but this initial system has been significantly over designed, especially with regard to the lead shielding and size of the detectors. It should be reasonable to build a prototype LMR land mine detection system with a system weight in the range of 80 kg. A breakout of the weight for the principal components of this initial system is as follows:

lead shielding and aluminum support platform	35	kg
detector assemblies		
(scintillator material and mounting frame)	30	kg
unistrut steel frame	28	kg
x-ray generator	16	kg
steel rail assemblies for front to back motion	11	kg
two motor assemblies and lead screw	8	kg
rotating collimator	5	kg
fork lift channel assemblies	<u>27</u>	<u>kg</u>
Total	160	kg



Figures 1 through 4 show the main portions of the portable LMR land mine detection system before being mounted on its movable vehicle. The long green cylinder shown in the four figures is the Lorad160 kVp X-ray generator. Figure 1 shows a front view of the assembly and the larger diameter, short green cylinder at the front end of the x-ray generator is the rotating source collimator. The flat (circular) ends of the rotating collimator are silver; the source collimator can also be seen in all four figures. The black belt which connects to a motor that drives the rotating source collimator can be seen best in Figures 1 and 4. Figure 4 is a rear view of the assembly. The rotating source collimator provides for a side-to-side scanning of about 0.5 m on the soil surface, without having to reposition the system.

The lead-lined shield box that surrounds the x-ray generator can be seen in all four figures. In Figure 1, the front end of the box is removed; the front end of the box is in place in Figures 2, 3 and 4. Figure 3 is a side view of the system. The dark green (Unistrut) steel support frame bars can be seen in all four figures. The diagonal support frame bars are not in place in Figure 1.

Two of the three detector assemblies, mounted to the bottom of the frame, can be seen in all four figures. The front collimated detector and the central uncollimated detector are in place. The rear collimated detector, which is not in place, goes behind the central uncollimated detector. The front detector collimator lead fin is best seen in the side view in Figure 3.

The cylindrical steel rods along which the system moves to achieve the front-to-rear scanning are seen in all four figures, but show best in Figure 4. A second motor assembly is used to achieve the 0.6 m front-to-rear scanning ability, without having to reposition the system.

The green rectangular box shown at the rear of the assembly in Figure 1 is the x-ray generator controller. The two rectangular boxes shown in the foreground in Figure 4 (rear of the system) are the two motor controllers/power supplies. In all four figures, the system is seen to be resting on yellow horses. Considering the green metal (Unistrut) frame portion of the system in Figures 1, 2, 3 and 4, the overall dimensions are: from front-to-back 6.6 ft (~2 m); from side-to-side about 3 ft (~0.9 m); and from top-to-bottom at the rear of the frame also about 3 ft (~0.9 m). The detectors and mounting assembly extend about 1.6 ft (~0.5 m) below the green frame. Figure 5 shows the completed LMR land mine detection system mounted on its transportation vehicle.

The LMR mine detection system shown in Figure 5 was used to obtain images out-of-doors using the simulated land mines developed under this grant. Front and rear collimated detector images for a 15 cm diameter anti-vehicle land mine for the cases where the mine was laid on the surface and buried at 1.3 cm and 2.5 cm depths-of-burial are shown in Figures 6, 7 and 8, respectively. The shown scan fields are 49.2 cm x 54 cm and the horizontal and vertical axes markings in these figures are distances in cm. The total active scan time for these images was about 30 seconds and the total time for image

acquisition was about one minute. These images were taken under very poor conditions; the soil was saturated following days of heavy rains.

In Figure 6, the surface-laid mine casts a shadow. This shadow is behind the mine in the front detector image and in front of the mine in the rear detector image. The central void in the mine leads to a high intensity area at the front edge of the mine in the front detector image and a high intensity area at the rear edge of the mine in the rear detector image. These phenomena are explained in Chapter 2 of the doctoral dissertation that is included as Appendix I of this report. This doctoral dissertation, completed by Zhong Su under this research program, is titled "Fundamental Analysis and Algorithms for Development of a Mobile Fast-Scan Lateral Migration Radiography System."

Because the images in Figures 7 and 8 are for buried rather than surface-laid mines, there is no shadow effect and no front edge or rear edge high intensity area in the mine image resulting from the central void. Instead, the front collimated detector image of the mine is shifted to the rear and the rear collimated detector mine image is shifted forward. This lateral migration shifting phenomena is a key signature of LMR and is explained in Chapter 2 of Zhong Su's dissertation in Appendix I.

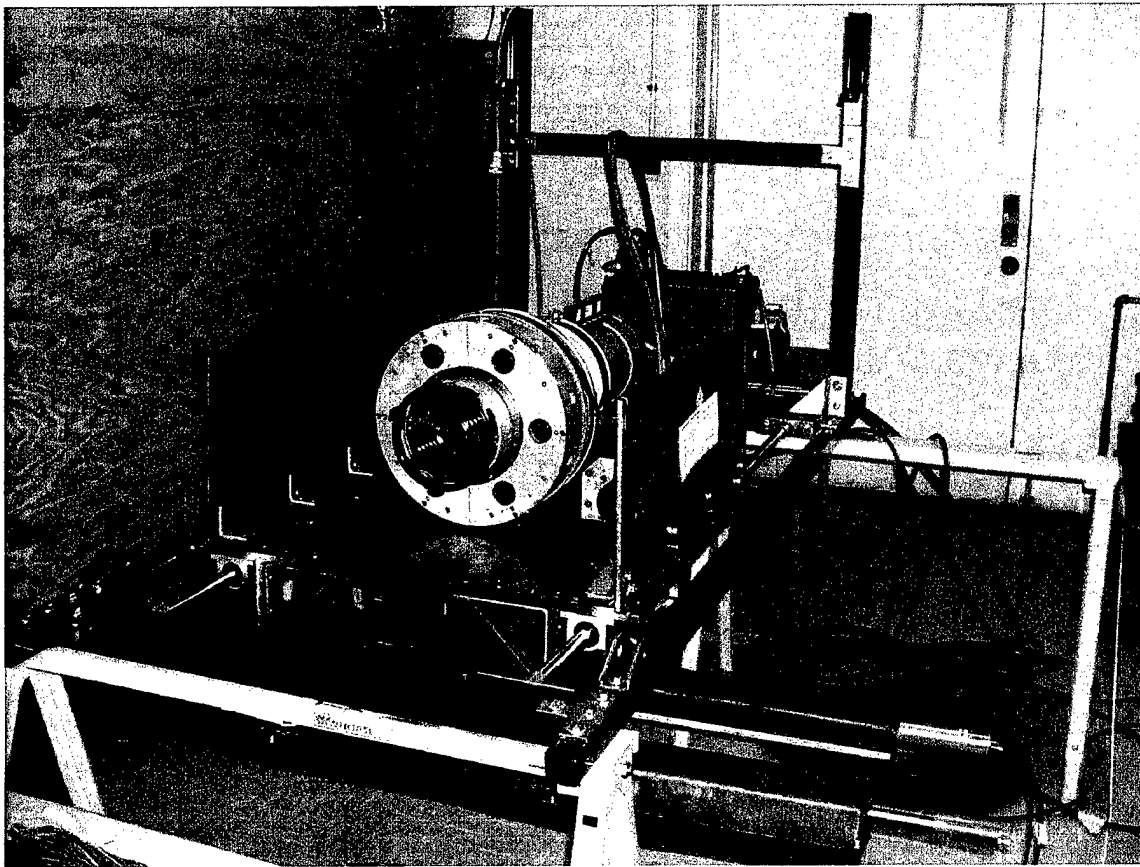


Figure 1 LMR Land Mine Detection System - View from the Front (with front end of lead shield box removed).

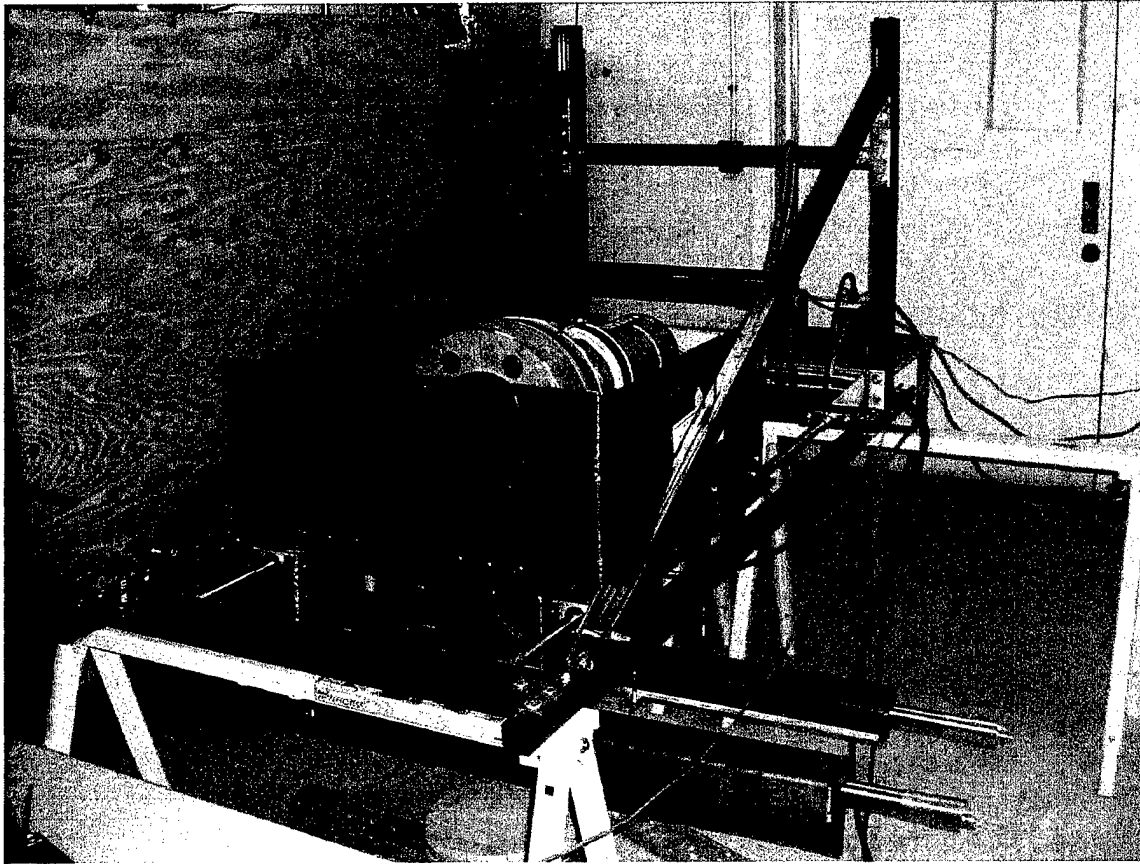


Figure 2 LMR Land Mine Detection System – View from Front (with front end of lead shield box in place).

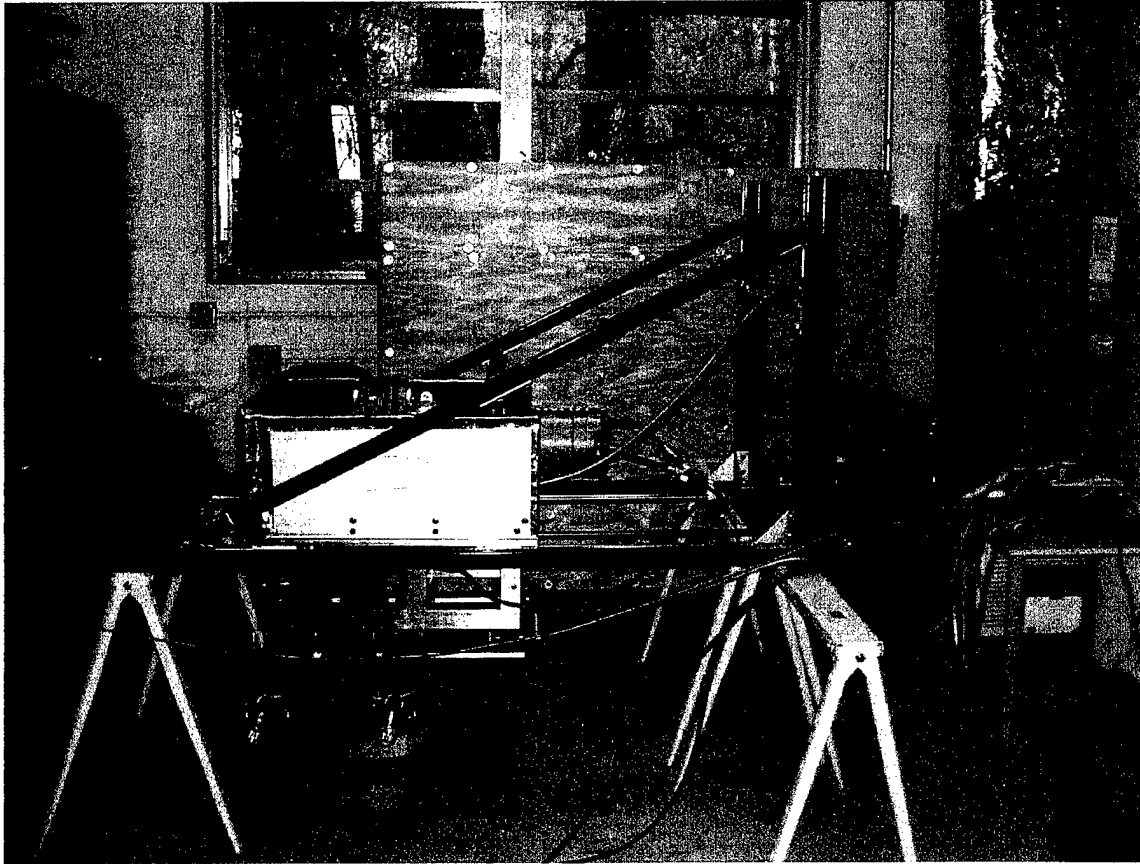


Figure 3 LMR Land Mine Detection System – View from the Side.

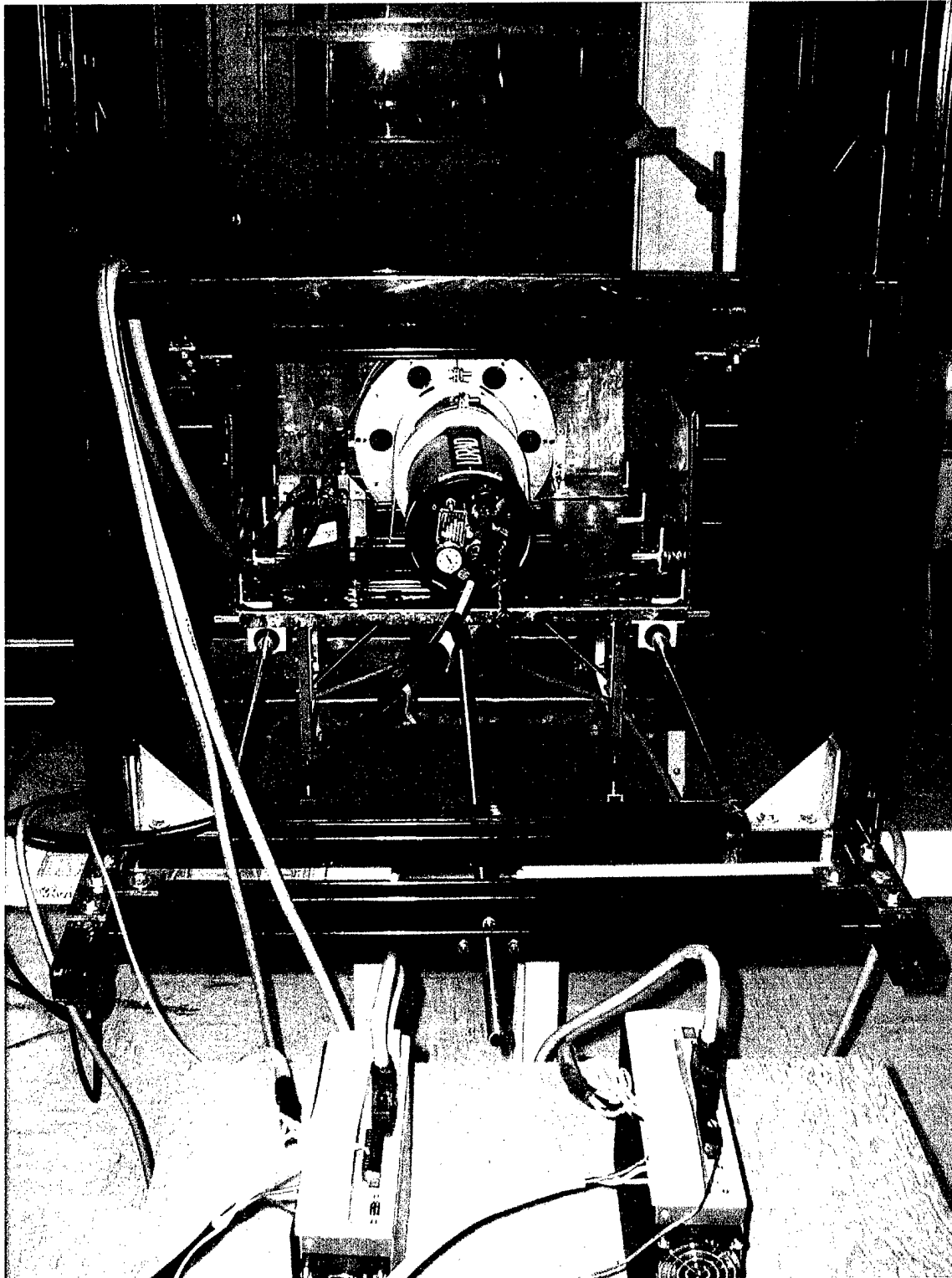


Figure 4 LMR Land Mine Detection System - View from the Rear.



Figure 5 LMR Land Mine Detection System Mounted on its Transportation Vehicle.

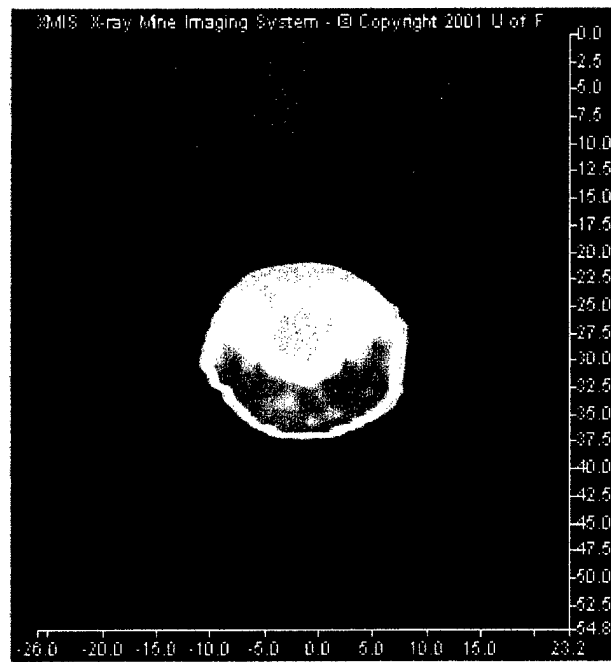
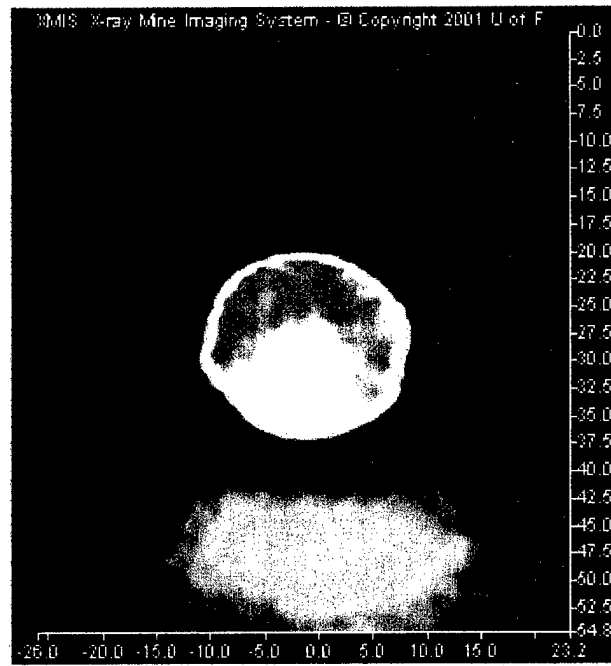


Figure 6. Front and rear collimated detector images of 15 cm diameter simulated anti-vehicle land mine laid on the soil surface (49.2 cm x 54 cm scan field).



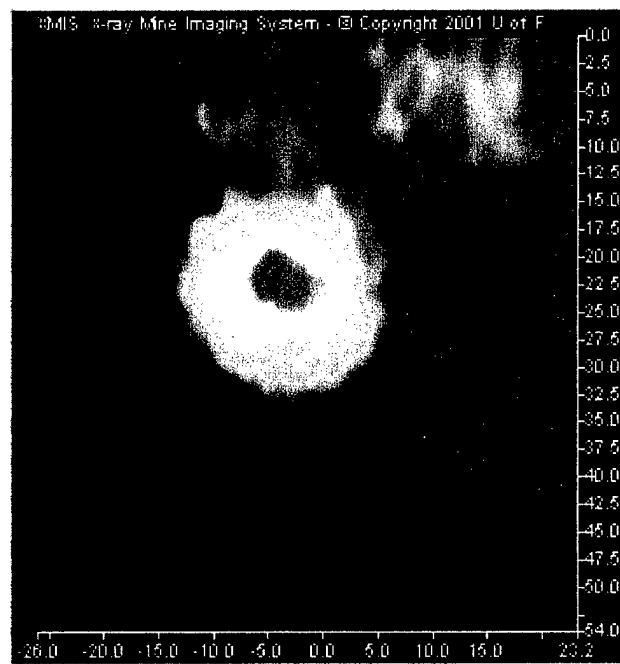
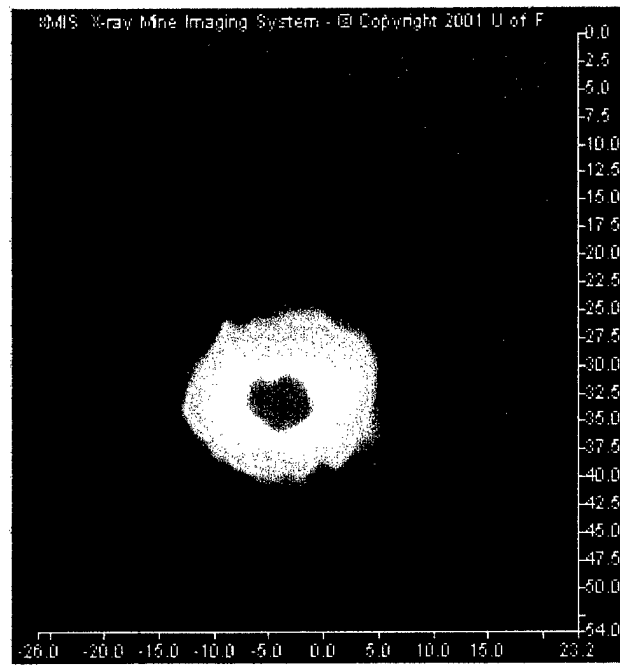


Figure 7. Front and rear collimated detector images of 15 cm diameter simulated anti-vehicle land mine with a 1.3 cm depth of burial (49.2 cm x 54 cm scan field).

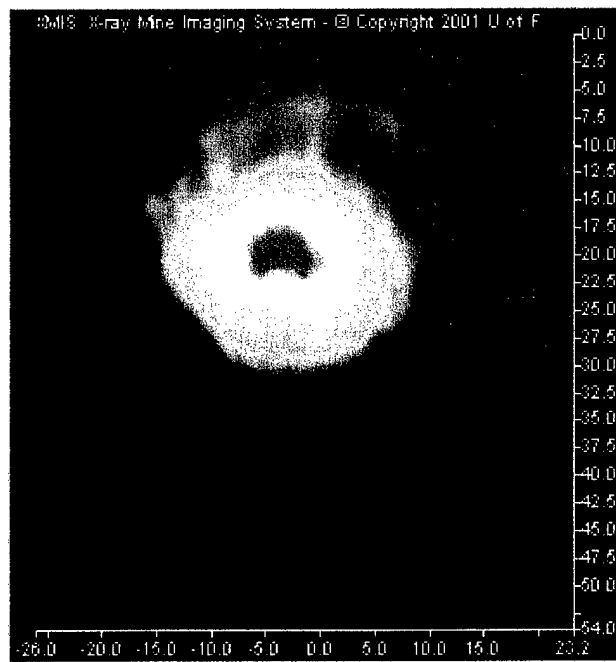
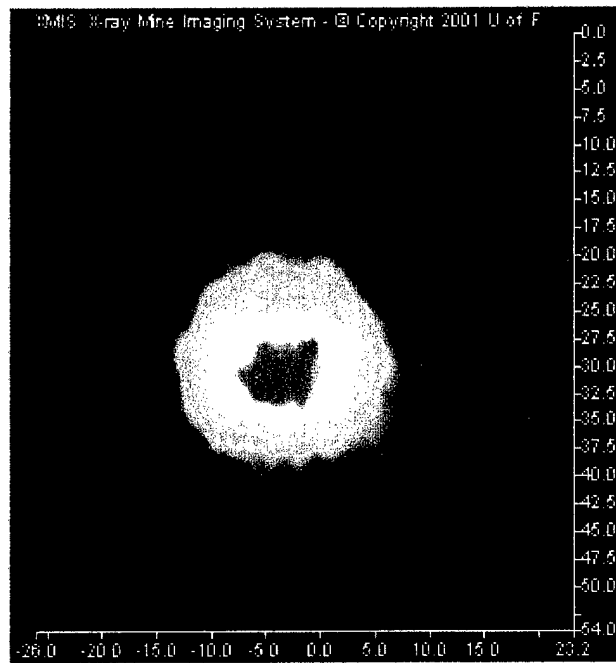


Figure 8. Front and rear collimated detector images of 15 cm diameter simulated anti-vehicle land mine with a 2.5 cm depth of burial (49.2 cm x 54 cm scan field).

### List of Publications and Reports

1. C. Wells, Z. Su, J. Moore, E. Dugan and A. Jacobs, "Lateral Migration Radiography Measured Image Signatures for the Detection and Identification of Buried Landmines," SPIE Proceedings on Detection And Remediation Technologies for Mines and Minelike Targets IV, Vol. 3710, pp 906-916, April, 1999.
2. Dugan, E. and Jacobs, A., "Lateral Migration Radiography Image Signatures for the Detection and Identification of Buried Landmines," Technical Report, ARO Grant No. DAAG-55-98-1-0400, University of Florida, Gainesville, Florida, January, 2000.
3. Su, Z., Jacobs, A., Dugan, E., Wells, C., Allard, A., Carriveau, G., "A Practical Land Mine Detection Confirmation System Based on X-ray Lateral Migration Radiography," Fifth Symposium on Technology and the Mine Problem, Monterey, CA, April, 2000.
4. Wells, C., Su, Z., Allard, A., Salazar, S., Dugan, E., and Jacobs, A., "Suitability of Simulated Landmines for Detection Measurements Using X-ray Lateral Migration Radiography," SPIE Proceedings on Detection And Remediation Technologies for Mines and Minelike Targets V, Vol. 4038, pp , Orlando, FL, April, 2000.
5. Allard, A, Dugan, E. and Jacobs, A., "Image Processing Techniques for Lateral Migration Radiography Land Mine Images," Technical Report, ARO Grant Number DAAG-55-98-1-0400, University of Florida, Gainesville Florida, June, 2000.
6. Su, Z., Jacobs, A. , Dugan, E. and Ekdahl, D, "X-ray Lateral Migration Radiography System and Its Application in Land Mine Detection," Proceedings of SPIE 45<sup>th</sup> Annual Meeting, Symposium on Optical Science and Technology, San Diego, July, 2000.
7. Well, C. "Contributions To Measurement Systems for Land Mine Detection and Nondestructive Testing Using Lateral Migration Radiography," Masters Degree Research Project, University of Florida, Gainesville, Florida, August, 2000.
8. Su, Z., Jacobs, A., Dugan, E., Howley, J. and Jacobs, J. "Lateral Migration Radiography Application to Land Mine Detection, Confirmation and Classification," *Optical Engineering*, Vol. 39, No.9, pp 2472-2479, September, 2000.
9. Su, Zhong, "Fundamental Analysis and Algorithms for Development Of A Mobile Fast-Scan Lateral Migration Radiography System," Ph. D. Dissertation, University of Florida, Gainesville, Florida, August, 2001

Scientific Personnel:

Edward T. Dugan, Ph.D., PI  
Alan M. Jacobs, Ph.D., co-PI  
Dan Ekdahl, Electronics Technician  
Zhong Su, Graduate student  
Christopher Wells, Graduate student  
Anthony Allard, Graduate student  
Laurent Houssay Graduate student  
Robert Smith, Graduate student

Degrees Received:

Christopher Wells, Masters in Nuclear Engineering  
Zhong Su, Ph.D. in Nuclear Engineering

Report of Inventions: None

Technology Transfer:

None yet. If the tests at Fort A.P. Hill in August or September, 2001, are successful, there is definite interest, both here and outside the U.S., in developing LMR for humanitarian mine detection applications, especially as a confirmation sensor. Also, NVESD at Fort Belvoir is contracting to use our system to investigate spatially correlated false alarms that have occurred over the years using different detection systems on the land mine test lanes at Fort A.P. Hill

In addition, as a result of this research, the idea of extending the principles of LMR to the detection of flaws and defects in materials and structures has received support from the DOE in the form of a 2 year \$200 K research grant. Applications are to be investigated for which other techniques are unsatisfactory and where LMR, because of its unique features, may be expected to be successful. An example is in the detection of delaminations in certain carbon-carbon composites. Preliminary experiments and Monte Carlo simulations are very promising. Thus, a technology transfer may occur not only for land mine detection using LMR, but also for the detection of flaws and defects in materials and structures.

## **Appendix I**

### **Doctoral Dissertation**

FUNDAMENTAL ANALYSIS AND ALGORITHMS FOR  
DEVELOPMENT OF A MOBILE FAST-SCAN  
LATERAL MIGRATION RADIOGRAPHY SYSTEM

FUNDAMENTAL ANALYSIS AND ALGORITHMS FOR DEVELOPMENT OF A  
MOBILE FAST-SCAN LATERAL MIGRATION RADIOGRAPHY SYSTEM

By

ZHONG SU

A DISSERTATION PRESENTED TO THE GRADUATE SCHOOL OF THE  
UNIVERSITY OF FLORIDA IN PARTIAL FUFILLMENT OF THE REQUIREMENT  
FOR THE DEGREE OF DOCTOR OF PHILOSOPHY

UNIVERSITY OF FLORIDA

2001

## ACKNOWLEDGMENTS

The author sincerely appreciates his academic advisor, Dr. Alan Jacobs, for the guidance and financial support. The author is indebted to the rest of the committee, Dr. Edward Dugan and Dr. Samim Anghaie, Dr. Charles Hooper and Dr. John Harris, for their guidance and help. The author also thanks Dan Ekdahl and Laurent Houssay for their help.

The author also thanks Raton Technologies Research, Inc., and the U.S. Army Research Office for providing financial support (ARO Grants DAAG –55-98-1-0400 and DAAG55-98-C-0069) for conducting this research.

The author also acknowledges his parents, Mr. and Mrs. Su, and his wife, Lily, for their understanding and unselfish support.

## TABLE OF CONTENTS

	<u>page</u>
ACKNOWLEDGMENTS .....	ii
ABSTRACT .....	v
CHAPTERS	
1 INTRODUCTION .....	1
2 LATERAL MIGRATION RADIOGRAPHY .....	4
Principles	
LMR Signature	
Lateral Migration Shifting	
Shadowing Effect	
Air Volume	
3 X-RAY BEAM ROTATING COLLIMATOR AND THE RESULTING IMAGING PHYSICS .....	21
Other Beam Formation Technologies	
Imatron X-ray Generator	
Multiple Cathode X-ray Generator	
Rotating Cylindrical Collimator with Helical Slots	
X-ray Beam Rotating Collimator	
Constitution of the Rotating Collimator	
Physical Analysis	
Imaging Physics of the Rotating Collimator	
Skewed Images	
Non-uniform Speed of X-ray Scanning on the Soil Surface	
Variation of X-ray Illumination Spot Size	
Definition of Resolution	
Raster Direction Squeezing Effect	
Compton Interaction Angular Difference	
4 ROTATING COLLIMATOR UNIQUE IMAGE ACQUISITION ALGORITHMS AND IMAGE ANALYSIS .....	39
Image Acquisition Algorithm	
Analysis	
Sampling Methods	



Image Analysis	
Linear Asymmetric Weighting Algorithm	
Comparisons of Measured Images and MCNP Images	
Image Processing	
5 GENERAL LMR IMAGE PROCESSING AND PATTERN	
RECOGNITION ALGORITHMS .....	51
Image Enhancement	
Image Segmentation	
Image Calculation	
Surface Feature Removal	
Subsurface Object Location and Depth Estimation	
Object Recognition	
6 MOBILE FAST-SCAN LMR MODULE .....	70
General Mechanical Design and System Composition	
X-ray generator	
X-ray Beam Rotating Collimator	
Detector Material and Position	
Detector Material: Scintillator vs Sodium Iodine	
Uncollimated Detector Positioning	
Detector Electronics and Electromagnetic Interference Shielding	
Motion Control and Data Acquisition Synchronization	
Platform Repositioning and Safety Switches	
7 SUMMARY AND CONCLUSION .....	89
APPENDICES	
A MATLAB CODES OF IMAGE PROCESSING AND	
PATTERN RECOGNITION .....	95
B LABVIEW MOTION CONTROL AND DATA ACQUISITION	
PROGRAM ILLUSTRATIONS .....	112
C RADIATION FIELD SURVEY OF THE LMR	
FAST-SCAN MODULE .....	118
D RASTER SCAN RESOLUTION IMPROVEMENT ALGORITHMS .....	119
REFERENCES .....	122
BIOGRAPHICAL SKETCH .....	124

Abstract of Dissertation Presented to the Graduate School  
of the University of Florida in Partial Fulfillment of the  
Requirements for the Degree of Doctor of Philosophy

FUNDAMENTAL ANALYSIS AND ALGORITHMS FOR DEVELOPMENT OF A  
MOBILE FAST-SCAN LATERAL MIGRATION RADIOGRAPHY SYSTEM

By

Zhong Su

May 2001

Chair: Alan M. Jacobs

Major Department: Nuclear and Radiological Engineering

Lateral migration radiography (LMR) is a unique x-ray Compton backscatter imaging (CBI) technique to image surface and subsurface, or internal structure of an object. An x-ray pencil beam scans the interrogated area and the backscattered photons are registered by detectors which have varying degrees of collimation.

In early LMR applications, either the LMR systems or the imaged objects are moved on a rectangular grid, and at each node, the systems register backscattered photon energy deposition as pixel intensity in acquired images. The mechanical movement of the system or objects from pixel to pixel causes prolonged image scan time with a high percentage of system dead time. To avoid this drawback, a particular x-ray beam formation technique is proposed and analyzed. A corresponding mobile, fast-scan LMR system is designed, fabricated and tested. The results show a two orders-of-magnitude reduction in image scan time compared with those of previous systems.

The x-ray beam formation technique, based on a rotating collimator in the LMR system, implements surface line scan by sampling an x-ray fan beam. This rotating

collimator yields unique imaging effects compared to those for an x-ray beam with fixed collimation and perpendicular incidence: 1) the speed of the x-ray beam spot on the scanned surface is not uniform; 2) constant movement of the x-ray beam spot changes the resolution in the image raster direction; 3) x-ray beam spot size changes with location on the scanned surface; 4) the object image shows a squeezed effect in the raster scan direction; 5) under a uniform background, the Compton scatter angular distribution causes the x-ray backscatter field to be stronger, when the x-ray beam has greater incidence angle; and 6) the x-ray illumination spot trace on the scanned surface is skewed. The physics generating these effects is analyzed with Monte Carlo computer simulations and/or measurements. Image acquisition and image processing algorithms are developed and applied to acquired images to eliminate the undesirable effects. The images acquired with this system also have the general characteristics of LMR images: 1) displacement of object image center from the true object center exists for subsurface objects in the collimated detector images; 2) shadowing effects occur for objects that protrude above the scanned surface. 3) scanned objects with air volumes present greater contrast in the acquired images than those without air volumes. Image processing and object recognition algorithms are developed and applied to the LMR images to enhance the image quality, to remove surface clutter, and to obtain depth information of subsurface objects.

The physical analysis of the x-ray beam rotating collimator and the development of the corresponding mobile fast-scan LMR system and its image acquisition and processing algorithms show that LMR is a proven technique for fast, mobile object surface and subsurface examination.

## CHAPTER 1 INTRODUCTION

Lateral migration radiography (LMR)<sup>1</sup> is a new Compton backscatter imaging (CBI)<sup>2,3,4,5,6,7</sup> method. By detecting the reflected photons from an examined object, surface and subsurface images are formed. Traditional CBI uses x-rays as the source to illuminate the area of interest and the backscattered photons are detected. The backscattered photons include both once-collided photons and multiple-collided photons, but only the once-collided photons are considered as the signal in the traditional CBI. If a scatter volume is isolated by a highly restrictive source and detector collimators (relatively small apertures collimate both the radiation source and the detectors), there are very few once-collided photons to be detected. To get relatively good photon statistics, the required power of the x-ray generator is enormous or the illumination time is prohibitively long. In contrast to the traditional CBI, the LMR utilizes a different modality setup and detects multiple-collided photons as an additional signal to provide more information about the detected objects. Furthermore, the relatively non-restrictive detector collimators in LMR enable large area detectors to be employed which means that more backscattered x-ray photons are registered in a relatively short period of time. Therefore, LMR requires less x-ray power and provides more usable information to the user in a relatively small time interval. The LMR images have unique characteristics compared to the traditional CBI images.

In early LMR systems<sup>8</sup>, a perpendicular incidence x-ray pencil beam was employed to scan the imaged surface. Depending on the mobility of the LMR system and

imaged objects, either the x-ray generator and detector assembly or the imaged objects were moved on a two dimensional grid to achieve an image scan for each pixel. These designs not only required certain space for the system to move from pixel to pixel, but also have a significant portion of the total imaging time as dead time because of the assembly movement. In order to achieve a fast image scan, a new x-ray beam formation technique that uses an x-ray beam rotating collimator<sup>9</sup> is analyzed and implemented. In this system, the image raster scan is achieved through continuous sampling of an x-ray fan beam generated with the rotating collimator. This replaces the motion in the raster scan direction of the x-ray generator and detector assembly or of the imaged objects. The LMR system with the x-ray beam rotating collimator has unique imaging physics. Some of the effects introduced by the rotating collimator on image acquisition and image formation include the following: the speed of the x-ray beam spot on the scanned surface is not uniform; constant movement of the x-ray beam spot changes the resolution in the image raster direction; x-ray beam spot size changes with location on the scanned surface; the object image shows a squeezed effect in the raster scan direction; under a uniform background, the Compton scatter angular distribution causes the x-ray backscatter field to be stronger, when the x-ray beam has a greater incidence angle; and the x-ray illumination spot trace on the scanned surface is skewed. In this work, data acquisition algorithms and image processing algorithms are developed to compensate for or correct some of these effects.

The LMR images have some unique features compared to other x-ray radiography images. They include displacement of the object center in the image from the true object center (hereafter named lateral migration shifting), a surface-protruding-object

shadowing effect, and significant image contrast enhancement from objects with air volumes. These features appear both in the images of the LMR systems with fixed x-ray beam collimation and those with rotating collimation. All of these features can be utilized to obtain information about the imaged objects: lateral migration shifting indicates subsurface objects present in the imaged area; the shadowing effect indicates that an object is laid on or protrudes above the scanned surface; air volumes enhance the contrast and indicate the internal structure of the imaged objects to help in object recognition. Image processing and object recognition algorithms are developed to utilize these features to accomplish image enhancement, surface clutter removal, object recognition, and parameter estimation. The image enhancement algorithms minimize image noise to improve image quality. The surface clutter removal algorithm utilizes the correlation between images from detectors with different collimation to eliminate surface clutter. In the particular application of LMR land mine detection, land mine parameter estimation and mine recognition algorithms calculate the depth-of-burial of the mine based on the amount of lateral migration shifting and mine-to-soil ratio of the images; and template matching techniques are used to distinguish mine from nonmine objects.

For demonstration purposes, a mobile fast scan LMR system with the x-ray beam rotating collimator is developed and tested in one LMR application area, land mine detection. The results show that LMR is a proven technology for mobile and fast examination of surface and subsurface objects.

## CHAPTER 2 LATERAL MIGRATION RADIOGRAPHY

### **Principles**

Lateral migration radiography is a CBI technique. CBI employs detector(s) to register Compton backscatter x-ray photons from the imaged objects. As illustrated in Figure 1, photons which have experienced one collision and multiple collisions are both registered by the detector. The once-collided photons are usually scattered from surface or shallow subsurface material, so they carry substantial surface feature and shallow subsurface information. The multiple-collided photons carry both surface feature and relatively deep subsurface feature information because of their multiple interaction paths. With reference to Figure 1, there are several parameters of the CBI setup which directly affect the performance of the system: the distance  $H$  from the detector lower surface to the scanned surface, beam to detector gap  $D$  and detector width  $W$ . With fixed  $D$  and  $W$ , varying  $H$  varies the solid angle subtended by the detector area to the x-ray beam interaction volume, and therefore, varies total energy deposition of the backscattered x-ray photons in the detector. Similarly, with fixed  $H$  and  $D$ , varying  $W$  varies total energy deposition of the backscattered x-ray photons in the detector; with fixed  $H$  and  $W$ , increasing  $D$  reduces the backscattered x-ray photon total energy deposition because of the reduction of the solid angle. If multiple-collided photons are interrogated, a collimator can be employed to prevent the majority of once-collided photons from entering the detector (Figure 2a). For the once-collided photons, the average Compton interaction locations are usually within a mean-free-path length below the imaged surface. So, given

an interaction volume location, collimator length can be calculated based on simple geometry (Figure 2b).

$$\frac{C}{H+d} = \frac{W}{W+D} \rightarrow C = \frac{W}{W+D} * (H+d)$$

This collimator does not prevent the once-collided photons originating from deeper locations than the location used for collimator length calculation from entering the detector.

In LMR, both detector setups in Figure 1 and Figure 2 are used and serve different purposes in the system (hereafter referred to as the uncollimated detector and collimated detector, respectively (Figure 3)). The uncollimated detector primarily registers once-collided photons which carry substantial surface feature information. The collimated detector predominately registers multiple-collided photons which carry both surface feature and subsurface feature information. This functionality is achieved by optimizing the collimators of the collimated detector. Depending on the number of detectors of each type, the setup of an LMR system varies. The setup for one uncollimated detector and one collimated detector is shown in Figure 3a and the setup of two detectors for each detector type is shown in Figure 3b.

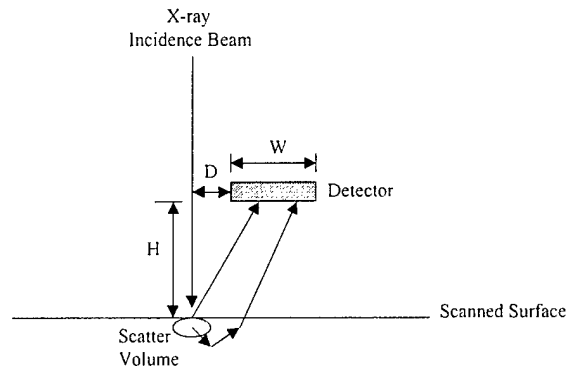


Figure 1. Compton backscatter imaging illustration and the backscatter photon paths.



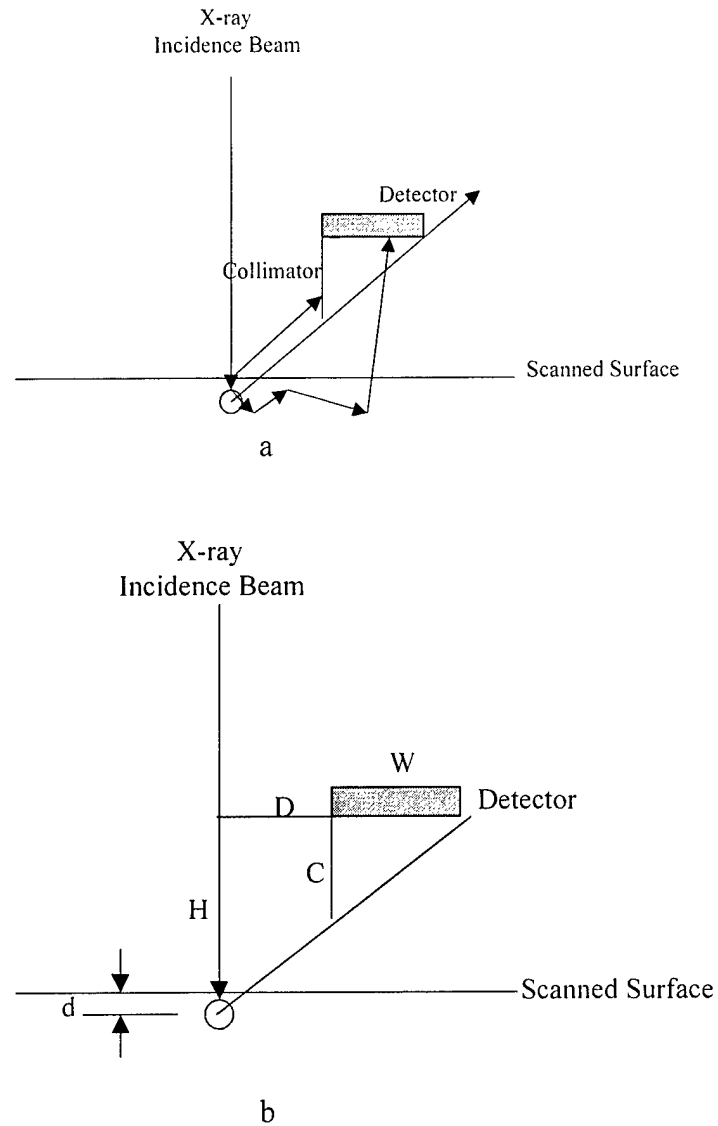
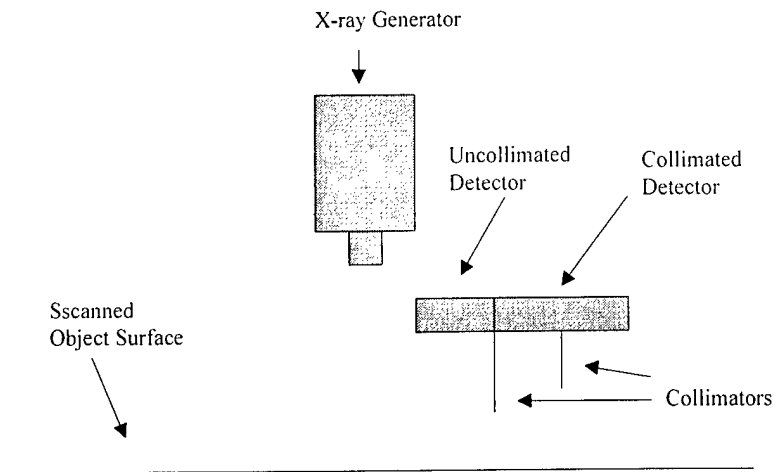
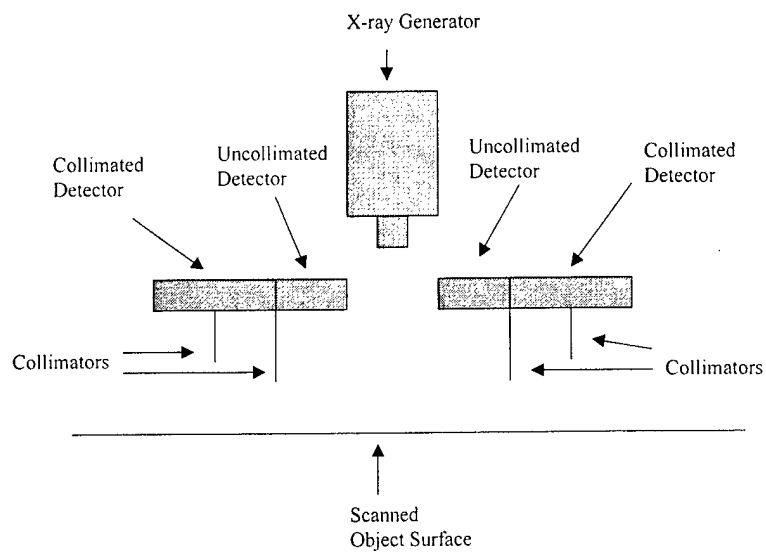


Figure 2. Illustration of the geometry between x-ray beam, scatter volume, collimator and detector. a) Illustration of the backscattered photon paths; b) Geometry for collimator length calculation.



a



b

Figure 3. LMR system setup illustration. a) One uncollimated detector and one collimated detector setup; b) Two uncollimated detector and two collimated detector setup.

Certain variations of the setups in Figure 3 are also worth discussing, e.g., x-ray beam angular incidence (Figure 4). Defining the two orthogonal directions in Figure 4 as the raster scan direction and the frame scan direction, there are two fundamental x-ray beam varying angular incidence cases: one has angular variation along the raster scan direction and the other has angular variation along the frame scan direction. In the frame scan direction case, the varying x-ray beam angular incidence completely changes the geometry of the scatter volume, collimator and detector, so the preferred functionality of each type of detector cannot be achieved. In the raster scan direction case, the geometry of the scatter volume, collimator and detector is still retained which means that the functionality of each type of detector can still be achieved. Therefore, the x-ray beam with varying angular incidence in the raster scan case is applied to a new LMR system. Details of the LMR system in which the x-ray beam has varying angular incidence in the raster scan direction are analyzed in Chapter 3.

For the x-ray energies of interest in the LMR system (130 to 180 kVp x-ray spectra with mean x-ray energies of around 40 to 60 keV)<sup>10</sup> two kinds of significant interactions exist: 1) Compton scatter and 2) the photoelectric effect. In Compton scatter, the photon is elastically scattered and there is energy transferred from the photon to the electron. The relative probabilities of these interactions is a function of the effective (average local) atomic number ( $Z$ ) and electron density of the material. Therefore, materials with different  $Z$  numbers and different electron densities have different intensity values in the LMR images.<sup>11</sup> In the photoelectric effect, the photon is absorbed and an electron is emitted. For an x-ray photon energy of about 50 keV or lower, the

higher  $Z$  materials have higher photoelectric effect cross sections and lower Compton scatter cross sections. For low  $Z$  materials, it is just the opposite. Therefore, when the

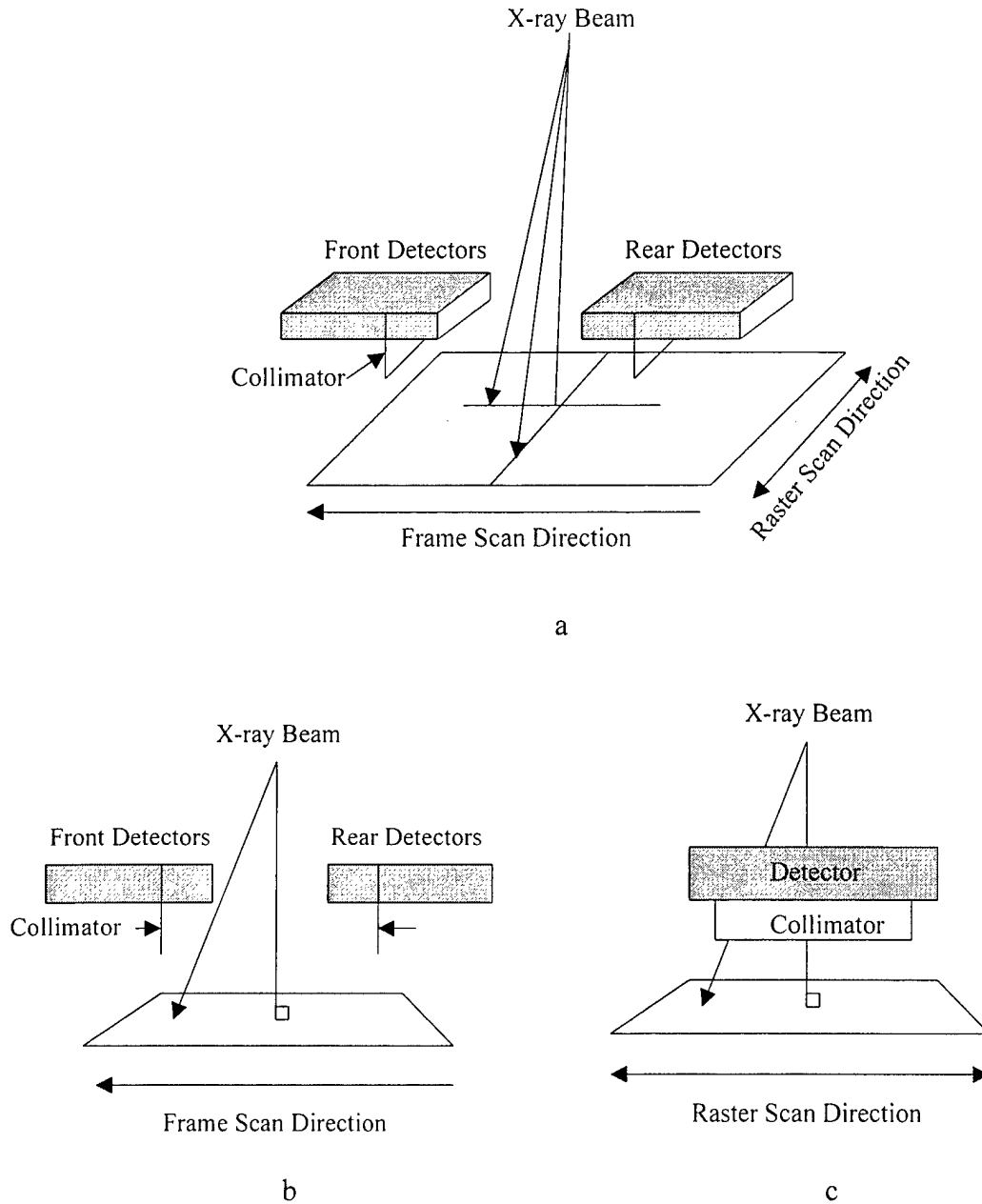


Figure 4. Illustration of x-ray beam angular incidence cases. a) Perspective view; b) X-ray beam angular incidence in frame scan direction; c) X-ray beam angular incidence in raster scan direction.

LMR images high  $Z$  material, such as metal, the majority of the x-ray illumination photons are absorbed by the material through the photoelectric effect and few photons are scattered via the Compton interaction. Thus, metallic materials have low intensity values in the LMR images. On the contrary, low  $Z$  materials, for example, plastic, have a lower  $Z$  number and medium electron density. When plastic is imaged by LMR, a great number of x-ray illumination photons have Compton interactions and some of the photons are backscattered to and registered by the LMR detectors. Thus, in the LMR images, a low  $Z$  material is represented by a high intensity value. In LMR, an extremely low density material contained in a high density material presents an important LMR image feature which is utilized extensively in pattern recognition. The extremely low density material, e.g., air, possesses low cross sections for both the photoelectric effect and Compton scatter and essentially allows x-ray photons to pass through without having many interactions; the photons have a very large mean-free-path in the material. When this material is within a high density material, the photon interaction field in this compound material is significantly different than that of a uniform high density material. Therefore, the LMR images exhibit great differences for these two cases and these differences indicate that heterogeneity exists in the scanned material. As an example, faults or delaminations in multi-layer materials create air gaps in them. When the materials are imaged by LMR, the parts with faults or delaminations present different intensities than the parts without in the acquired images, and these intensity differences indicate defects in the examined material.

In the physical process of LMR, uncollimated detector(s) predominantly register once-collided photons and some multiple-collided photons. The once-collided photons have Compton interactions with electrons of the imaged materials and each of these photons has only one Compton interaction in its history. Therefore, the first-collision photons bear the information of the imaged materials, (i.e., the Compton interaction cross sections and electron densities) and contribute to the total photon energy deposition in the uncollimated detector(s). Photons at different energy levels have different mean-free-paths in different materials, but only about one mean-free-path depth of the imaged material interacts with photons registered by the uncollimated detectors. Therefore, features of the surface and about one mean-free-path thick subsurface layer of the imaged material are detected by the LMR uncollimated detector(s). While for the collimated detector(s), mainly multiple-collided photons and a few once-collided photons are registered. The multiple-collided photons generally come from within a couple of mean-free-path thick subsurface layer of the imaged material which interacts with incident photons and scattered photons. As multiple-collision photons laterally migrate through the imaged material, structured electron density variations in the material modify the diffusing field. These photons, predominantly detected by the collimated detector(s), can emphasize the discontinuities of different regions in the material. Therefore, the collimated detector images show the contrast of the transport media as traversed by the photons in directions transverse to the source beam. (hence, the designation LMR).

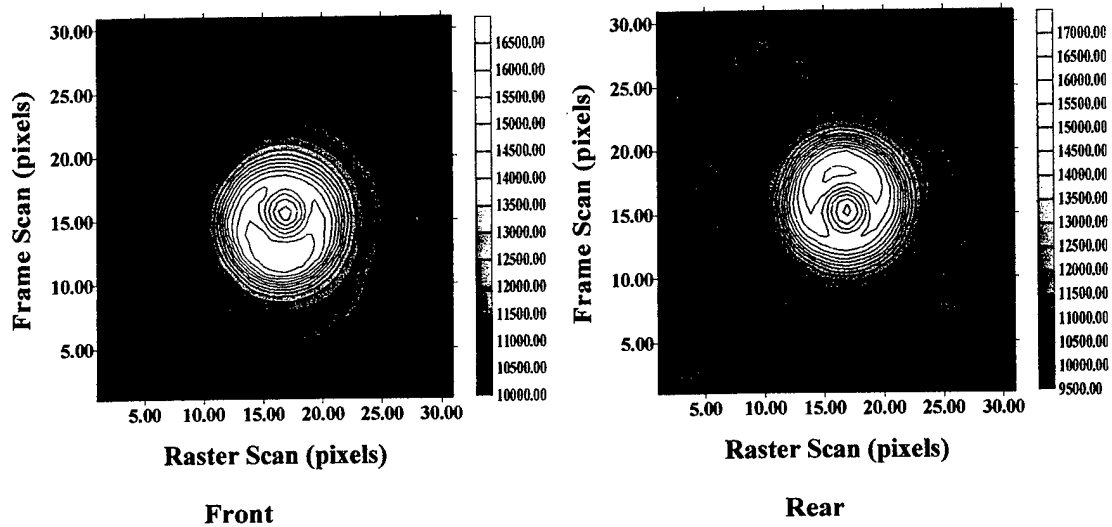
## **LMR Signatures**

### **Lateral Migration Shifting**

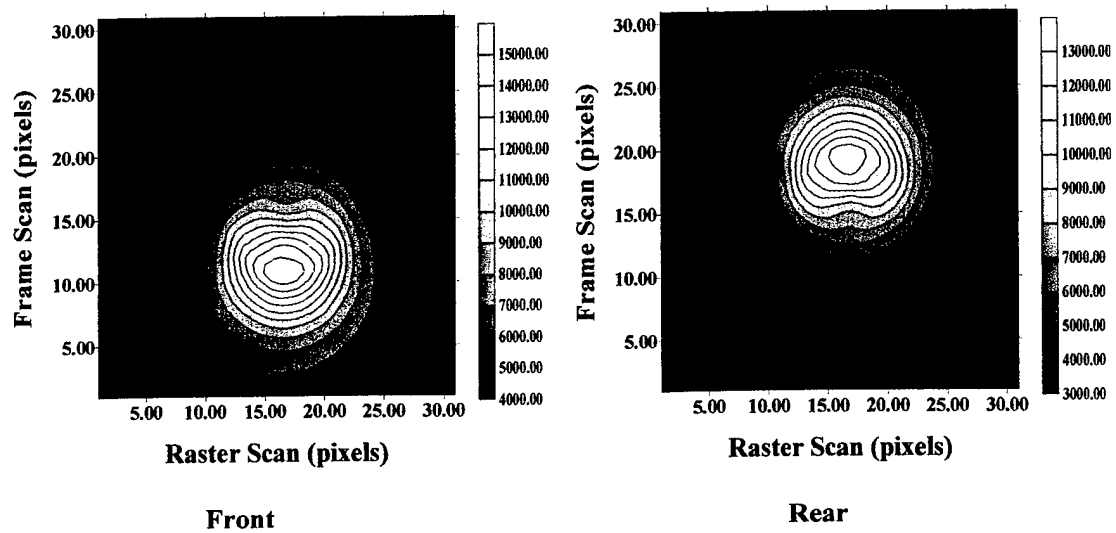
Monte Carlo numerical simulations and the actual LMR image acquisition measurements have demonstrated the different ways in which the uncollimated and the collimated detectors function in an LMR system and form the basis of the physical phenomena discussed in the previous section as well as the discussion of the origin of LMR image contrast. Photon lateral migration is very prominent in the collimated detector images.

Because of the photon lateral migration in the media, there is lateral migration shifting in the collimated detector images of the scanned subsurface objects. If the LMR system setup is as in Figure 3b, the object shift directions in the front and rear detector images are backward and forward respectively. This shift increases with object depth relative to the scanned surface, and is thereby a measure of the object depth. In order to explain the process of lateral migration shifting, one of the LMR applications, land mine detection, is used as an example. However, the lateral migration shifting exists in all LMR applications. In this dissertation, all the specific LMR images are from the LMR land mine detection application.

In the collimated detector images of Figures 5 and 6, lateral migration shifting exists in both the front and rear detector images and their shifts are opposite. For a plastic mine with the Compton scatter cross section greater than that of the soil, the number of multiple-collided photons detected from the plastic mine is greater than that from the soil and this causes the intensity increase in the images. Among the multiple-collided photons, those migrating through the mine have a higher probability of being registered



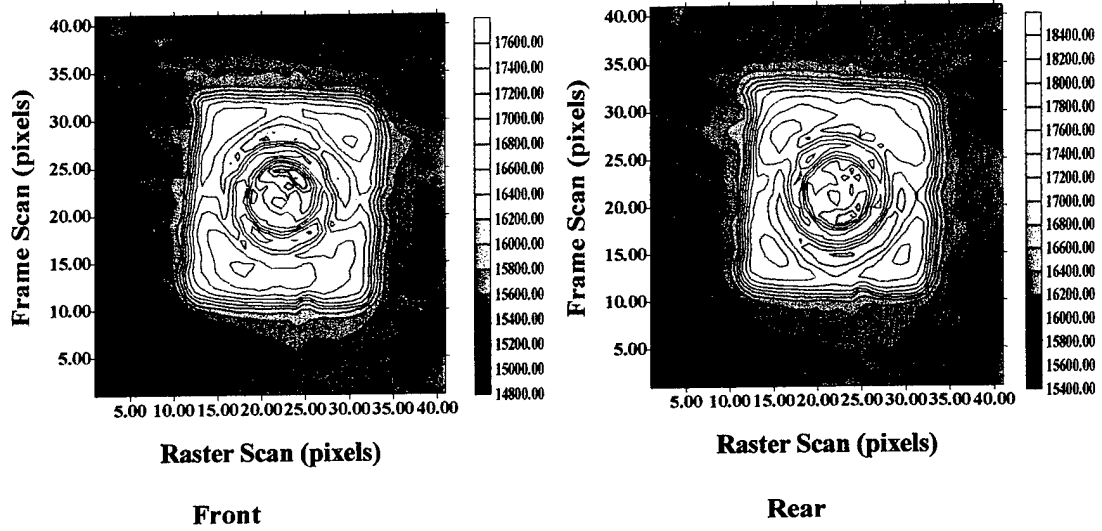
Uncollimated Detector Images



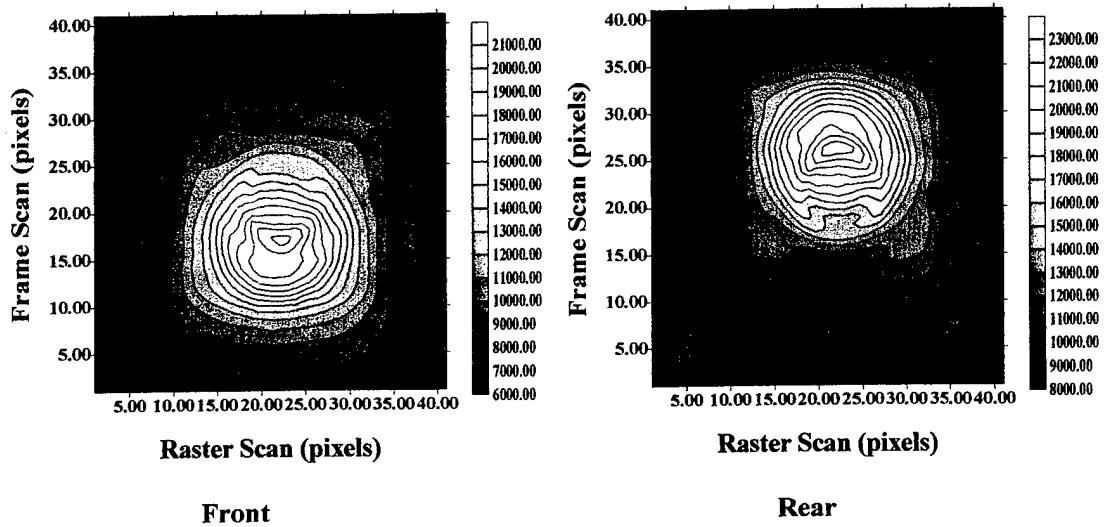
Collimated Detector Images

Figure 5. VS-1.6 antipersonnel mine, 2.5 cm depth-of-burial, 15 mm resolution.





Uncollimated Detector Images



Collimated Detector Images

Figure 6. M19 antitank mine, 2.5 cm depth-of-burial, 15 mm resolution.

by detectors. Therefore, during x-ray beam scanning, as the mine is initially encountered, the front collimated detector registers a higher intensity than the rear collimated detector.

Similarly, when x-ray scanning is on the final encountered mine edge, the rear detector registers more Compton scatter photons than the front detector. Due to this behavior, the highest intensity in the front collimated detector image tends to show up earlier than the physical center of the mine, which appears as backward shifting. In the rear collimated detector image the opposite happens. This shifting increases as the depth-of-burial of the land mine increases; therefore, the depth-of-burial of the mine can be estimated from the amount of shifting (see Figure 7). Analysis of the data of Figure 7, by estimating the difference between centers of highest intensity area, shows there are about 3.6 pixels of lateral migration shifting in the 2.5 cm depth-of-burial collimated detector images, and about 4.4 pixels of lateral migration shifting in the 5.0 cm depth-of-burial collimated detector images.

### **Shadowing Effect**

Shadowing effects are the result if the object protrudes above the scanned surface blocking some of the Compton scatter photons. As the x-ray beam scans toward the object, some of the Compton scatter photons emitted from the surface cannot reach the front detectors because of blocking by the object. Similarly, as the x-ray beam moves away from the object, some of the Compton photons are blocked so they cannot be registered by the rear detectors. Therefore, the shadows are behind the object in the front detector images and in front of the object in the rear detector images. The shadows are roughly symmetric about the raster direction axis in both the uncollimated detector images and collimated detector images. If the object is flush with or underneath the scanned surface, there is no shadowing effect in the acquired LMR images.

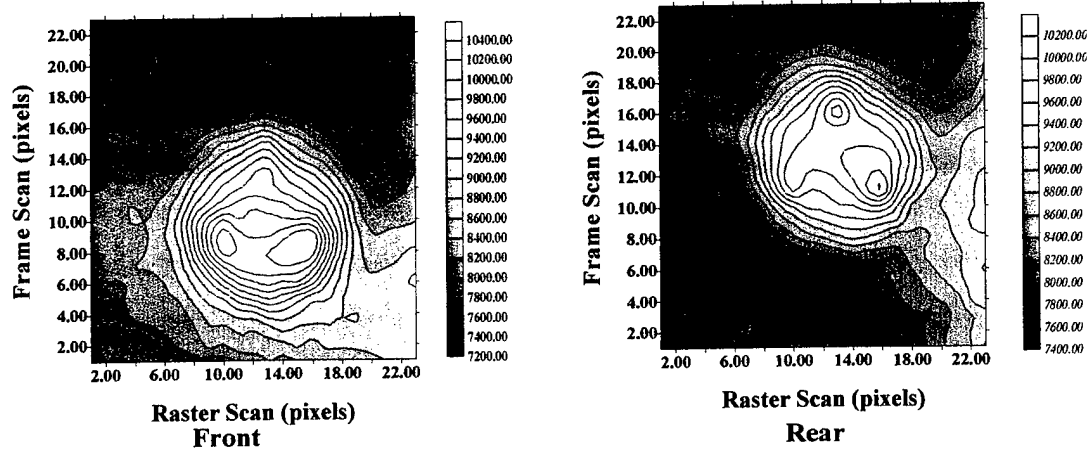
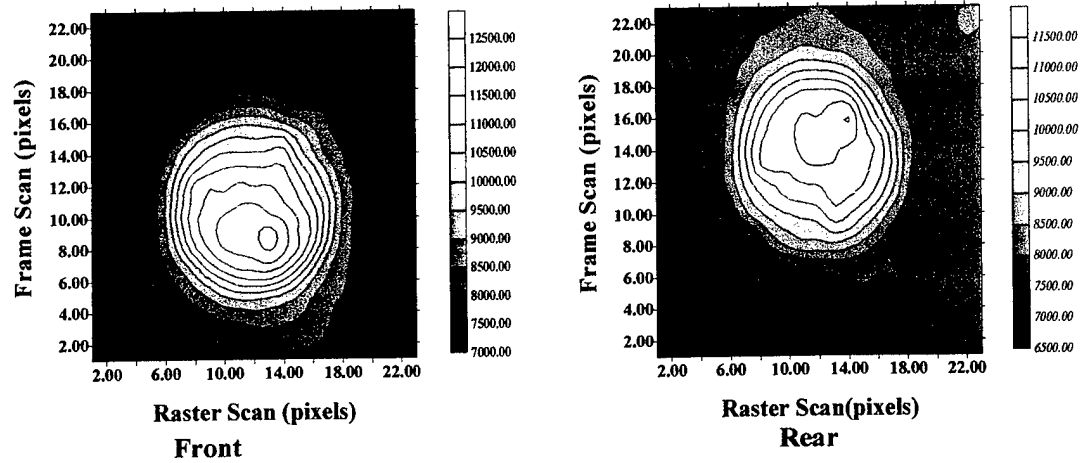


Figure 7. TMA-4 mine with 2.5 cm resolution.

As an example, in Figure 8, the shadows clearly accompany the mine images of both the collimated and uncollimated detectors. In actual deployment, antipersonnel mines are usually placed either on the soil surface or with a shallow depth-of-burial (i.e., normally not more than a few millimeters of soil overlay). The surface-laid land mines can be easily recognized by both the shadowing effects and the vivid air volume signature

(discussed in the next section) in combination with the mine's geometric shape in the LMR images. In contrast, the shallow buried mine emphasizes the air volume signatures and has no mine case shadow (Figure 9).

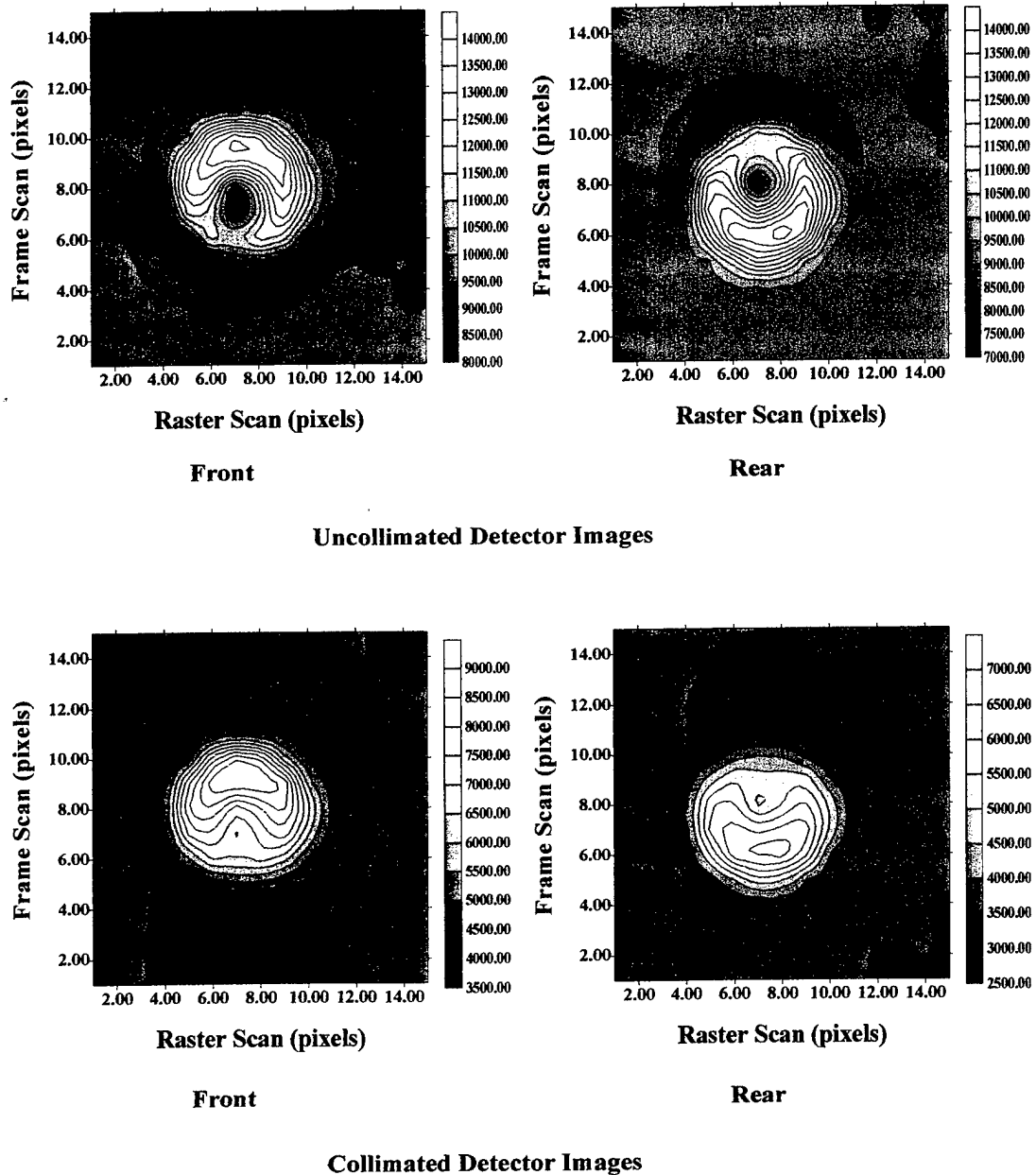


Figure 8. TS/50 antipersonnel mine, on surface, 15 mm resolution.

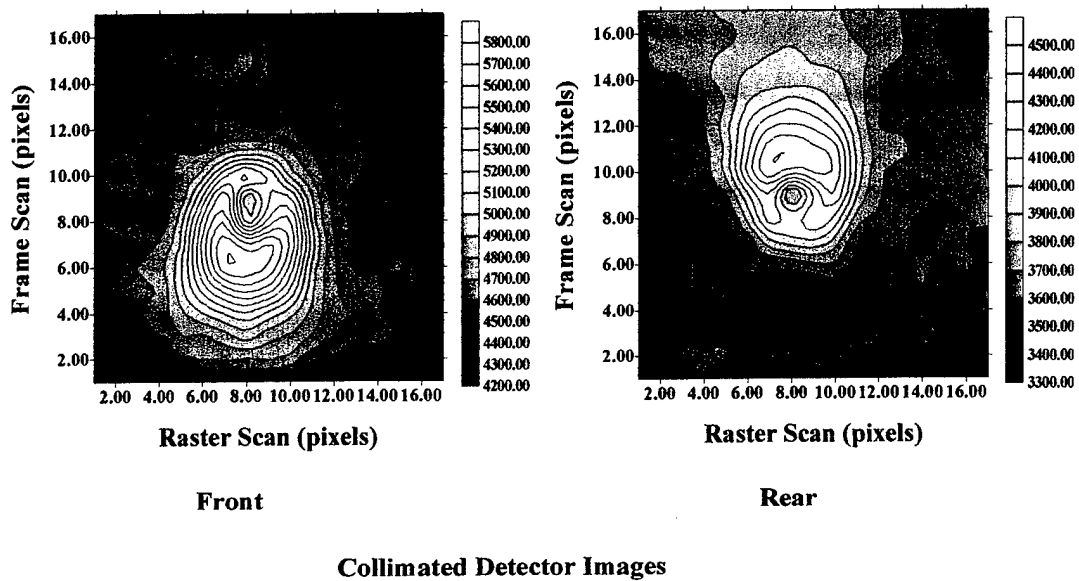
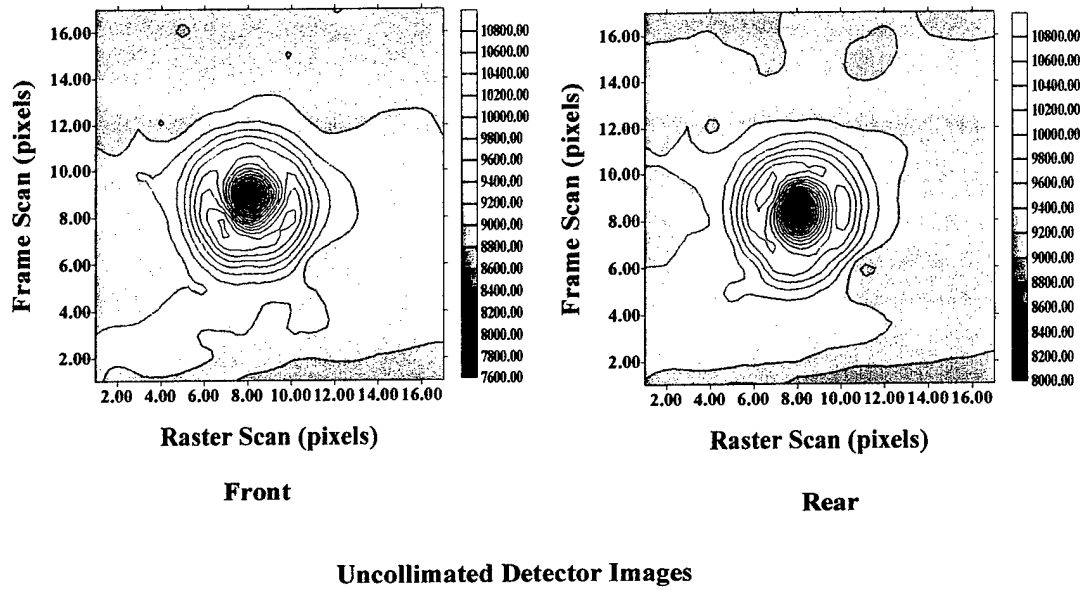


Figure 9. TS/50 antipersonnel mine, flush depth-of-burial, 15 mm resolution.

### Air Volume

Air allows free flight of x-ray photons. The existence of air volumes in scanned objects dramatically modifies the once-scattered photon exit paths as well as the multiple-

scattered photon migration paths, when compared to objects without air volume. When the x-ray beam is directly scanning over the air volumes, the photons which pass through the object material without any interaction will interact with the bottom or side wall of the air volume. The solid angles subtended by the LMR detectors for these photons are smaller than those of the photons interacting with an object without air volume. For all the photons at the first-collision sites, the probability of not being registered by the uncollimated detectors is higher when air volume is present than for the case of the object without air volume. As a consequence, an intensity decrease occurs at the location of the center of the air volume in the uncollimated detector images (see Figures 5 and 6). When the x-ray beam is scanning the material at the edge of the air volumes, photons scattered in the direction of the air volume will have a higher probability of being registered by the uncollimated detectors than the photons emitted in the direction of the object material. Therefore, there are high intensity areas right at the edge of the air volume and they occur at the front and back edge of the air volume in the rear and front uncollimated detector images, respectively (see Figures 5 and 6). For multiple-collided photons, the physical existence of the air volume modifies the photon field in the transport media. But because the air volume essentially gives free flight to the migrating photons and the multiple scattering of photons tends to average out the effect of the air volume, there is diffused evidence of the air volume in the collimated detector images. Therefore, in Figures 5 and 6, the collimated detector images clearly show evidence of the air volumes but do not include the singular definition shown in the uncollimated detector images.

In LMR land mine detection images, the inner air volume shapes combined with the outer geometric shapes of the land mines yield key signature features for land mine

detection and identification.<sup>12</sup> For detonator operation, every land mine has at least one fuse well to accommodate the fuse, detonator and booster. This fuse well, essentially an air volume with some plastics or metals, shows up clearly and uniquely in the LMR images.

## CHAPTER 3 X-RAY BEAM ROTATING COLLIMATOR AND THE RESULTING IMAGING PHYSICS

### **Other Beam Formation Technologies**

In Chapter 2, the LMR systems illustrated are systems with fixed collimation of the x-ray beam output. Using these systems to implement LMR, the whole assembly of the x-ray generator and detectors must move on a two dimensional grid and sample the x-ray backscattered field at each node to form the LMR image matrices. This LMR image acquisition scheme has some disadvantages. First, a majority of the total image scanning time is used to move the x-ray generator and detector assembly from pixel to pixel. For example, scanning a 60 cm by 60 cm area with 1.5 cm resolution using this type of system takes about 2 hours. Of this two hours, only about 5 minutes are for actual image acquisition time. So the system dead time is about 95 percent. This not only wastes time, but also prohibits LMR from being used in some time critical applications, e.g., land mine detection. Besides the high dead time percentage, the above type of system also requires a large volume of space for the system to move in both the raster scan and frame scan directions.

Over the past several years, based upon the need for fast scans and the advances of technology, some new methods to improve LMR image scan times were tried, or proposed, but failed because of either technology or financial difficulties. Among them were the Imatron x-ray generator,<sup>13</sup> the multiple cathode x-ray generator,<sup>14</sup> and the rotating cylindrical collimator with helical slots.



### **Imatron X-ray Generator**

One way to reduce the total LMR scan time is replacing the raster scan movement of the generator detector assembly by designing a new type of x-ray generator whose output can cover the entire raster length. Imatron Inc. designed and manufactured an x-ray generator, Imatron, to implement this task. In the Imatron, one large rectangular anode whose length covers the entire raster direction length is bombarded by a continuous beam of electrons. The electron beam is electromagnetically moved to sweep along a certain path which is synchronized with the system forward motion speed to provide an x-ray illumination spot on the scanned surface. In final tests, the Imatron could not provide consistent pixel-to-pixel x-ray illumination intensity; therefore, it was not acceptable as part of a fast scan LMR system.

### **Multiple Cathode X-ray Generator**

As another way to raster scan the imaged area without physical movement of the LMR system, a multiple cathode x-ray generator design was proposed by Bio-Imaging Research, Inc. In this design, there are multiple cathodes and one long common anode. The axis of the common anode is parallel to the image raster direction. By switching each cathode on and off sequentially, the x-ray output from the common anode sequentially scans the imaged surface area and, therefore, achieves an image raster scan with electronic switching which takes little time compared with that of the mechanical movement of the whole LMR assembly. Because of financial difficulties, this multiple cathode x-ray generator was not perfected.

### **Rotating Cylinder with Helical Slots**

Since designing and making a new x-ray generator requires tremendous technological and financial resources, using an off-the-shelf x-ray generator and designing a device to implement the raster scan is also considered. One of these devices is a rotating cylinder with helical slots to collimate the x-ray beam and at the same time, realize image raster scan (Figure 10). The design of this device was presented by Bio-Imaging Research, Inc. When this collimator is used in the LMR system, the axis of the cylinder should be parallel to the image raster scan direction. From the x-ray generator focal spot, part of the projection from the two slots of the cylinder overlaps and forms an x-ray illumination spot on the scanned surface. When the cylinder rotates, the spot moves along the raster scan direction. However, this design has an apparent drawback: half of the cylinder rotation time is dead time, so there is no x-ray illumination spot on the scanned surface during this period. Therefore, new x-ray beam rotating collimator design is presented in the following sections which has no dead time in LMR imaging.

### **X-ray Beam Rotating Collimator**

As another way to accomplish LMR fast scan and at the same time keep relatively good image quality, an x-ray beam rotating collimator is designed and its imaging physics is thoroughly studied. It provides fast scan with no dead time and only requires current x-ray generator and x-ray detector technologies.

### **Constitution of the Rotating Collimator**

This rotating collimator consists of two coaxial cylinders with proper slots opened in the cylinder wall. The inner cylinder is located coaxial with the x-ray tube head keeping the center of the slot aligned with the center of the x-ray output window. Outside

of this cylinder, the other cylinder has 10 equally separated holes aligned in the same section circle (see Figure 11). Thus, there are 36 degrees between adjacent holes, which at some time interval during rotation are within 40 degrees of the emerging x-ray fan beam collimated by the inner cylinder. These two cylinders together make a collimator which can achieve the raster scan in a continuous mode with no dead time. Therefore, system movement in the frame scan direction can be continuous to maximize the fast scan potential of the rotating collimator. The speed of the raster scan can be easily adjusted by changing the speed of the rotating collimator to meet different image scan requirements, i.e., image scan time and good image quality. Figure 12 shows the cross section view of the rotating collimator.

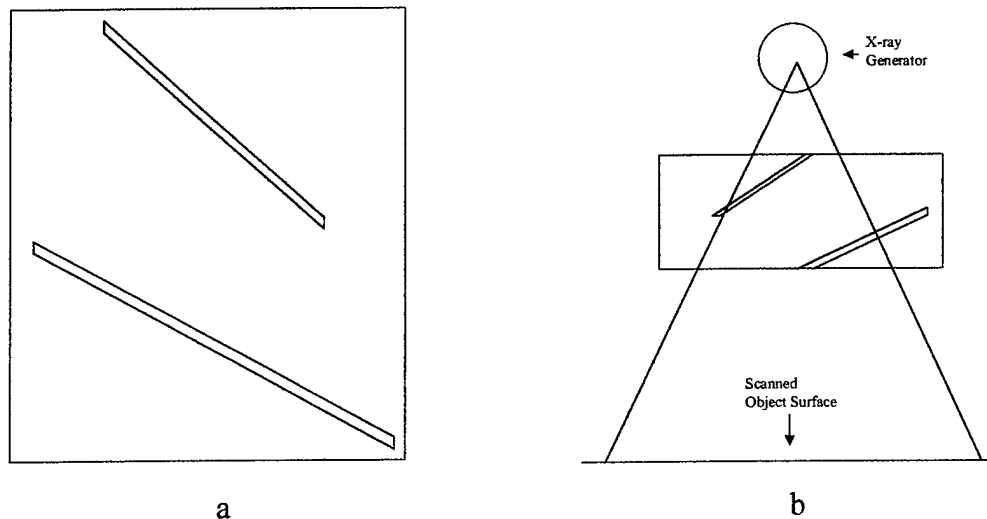


Figure 10. Illustration of rotating cylinder with helical slots. a) Extended view of the cylinder; b) Application setup.

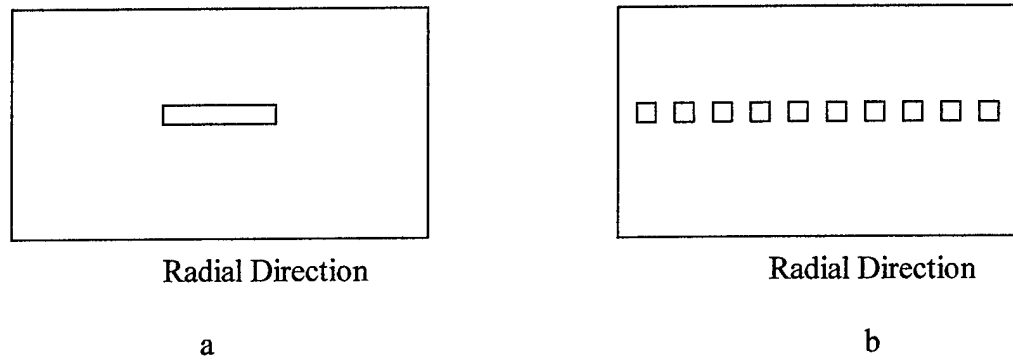


Figure 11. Illustration of rotating collimator concept (extended view). a) Inner Cylinder; b) Outer Cylinder.

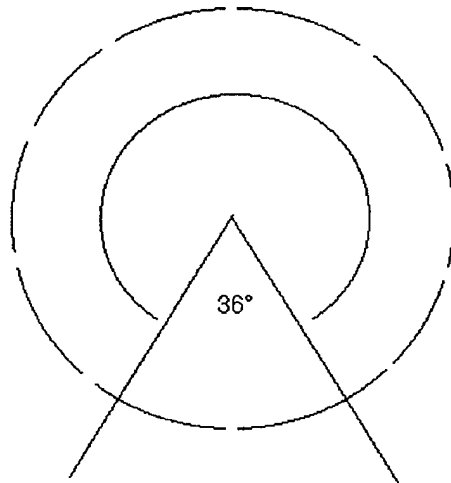


Figure 12. Cross section view of the rotating collimator.

### Physical Analysis

With the rotating collimator, the LMR system setup is not dramatically different from previous LMR systems. In this embodiment, a detector array of two collimated and one uncollimated detectors is used (the setup is shown in Figure 13). Only one

uncollimated detector is used because there is no dramatic difference between the signals of two uncollimated detectors which mainly register surface features of scanned objects.

Even though the x-ray beam scan in the raster direction with the rotating collimator is different from those of previous LMR systems, the x-ray beam rotating collimator system images have all the major LMR signatures: the lateral migration shifting, the surface protruding object shadowing effect and the air volume contrast enhancement.

Multiple-collided photons laterally migrate through the media and are registered by the collimated detectors. At the photon first collision sites, the diffusion paths are influenced by the x-ray beam angular incidence from the rotating collimator. But after multiple collisions, the initial influences are essentially erased and there is little difference in average energy deposition between the x-ray variable angular incidence case and the perpendicular incidence case. For the surface protruding object shadowing effect, the objects still block once-collided or multiple-collided photons as they attempt to pass through the objects. However, the Compton scattering angular difference may affect the total number of photons blocked by the objects. Similarly, air volumes do not significantly affect the diffusion paths of the photons from the x-ray beam rotating collimator compared with those of the x-ray beam perpendicular incidence case. However, the x-ray beam rotating collimator does physically implement the raster scan in a quite different manner than for the fixed collimator, perpendicular beam incidence case and it does affect the LMR imaging physics and corresponding image acquisition and image processing schemes. In the following sections, the LMR imaging physics are studied.

### Imaging Physics of the Rotating Collimator

Using the x-ray beam rotating collimator, the raster scan is no longer the same as when the x-ray beam has perpendicular incidence. When the rotating collimator rotates at a certain speed, the speed of the x-ray beam spot on the scanned surface is a function of the angle of the x-ray beam incidence. Furthermore, the spot size on the scanned surface changes as the x-ray beam incidence angle changes. Because of continuous movement of the x-ray beam spot on the scanned surface during the image data acquisition, resolution in the image raster scan direction is not the same as that in the image frame scan direction. Studies of the x-ray beam angular incidence show there is also an image raster direction squeezing effect and a Compton interaction angular difference effect. When the LMR system is moving forward synchronously with the speed of x-ray beam rotating collimator, the x-ray spot trace on the scanned surface is skewed.

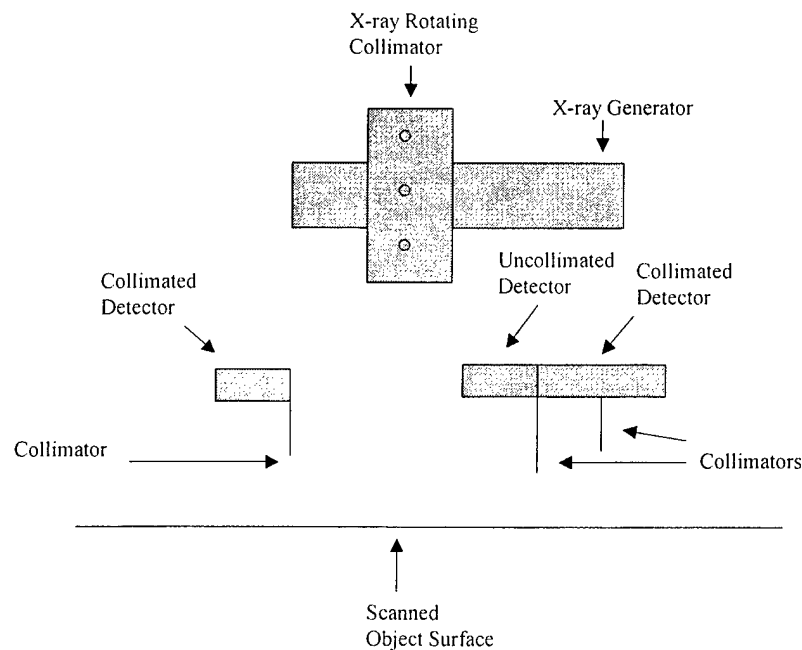


Figure 13. LMR system setup with x-ray beam rotating collimator.

### Skewed Images

During the image acquisition process, the x-ray beam rotating collimator is rotating while there is simultaneously constant frame movement of the x-ray generator and detector assembly; this combination of movements affects the resulting images. The trace of the x-ray beam spot on the scanned surface, as shown in Figure 14, is skewed to the upper right corner of the scanned area. This image distortion can be corrected by interpolation of the original data on a rectangular image grid.

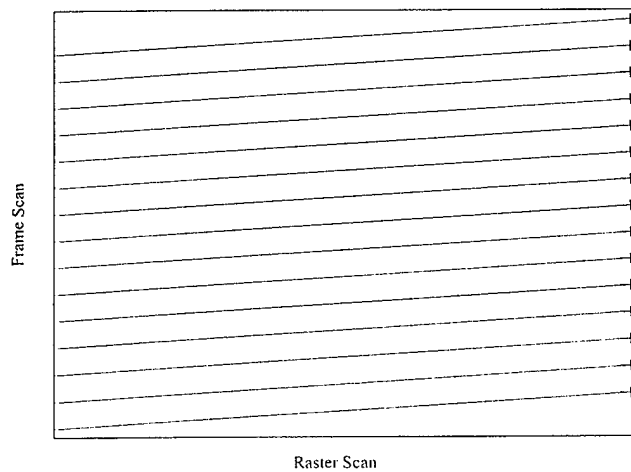


Figure 14. X-ray beam trace on the soil surface.

### Non-uniform Speed of X-ray Scanning on the Soil Surface

While the rotating collimator is rotating at a constant speed, the x-ray spot on the ground moves at a non-uniform speed.

When using this rotating collimator, the speed of the x-ray beam spot on the scanned surface has to be obtained to realize uniform illumination of each pixel. In Figure 15,  $V_c$  is the horizontal speed of the pixel when the x-ray beam has perpendicular

incidence and  $V_p$  is the horizontal speed of some other pixels on the raster scan line. The speed of  $V_p$  is derived as follows:

$$PC / h = \tan(\theta) \rightarrow V_p = h * \omega / \cos^2(\theta) = V_c / \cos^2(\theta)$$

where  $\omega$  is the angular speed of the rotating collimator.

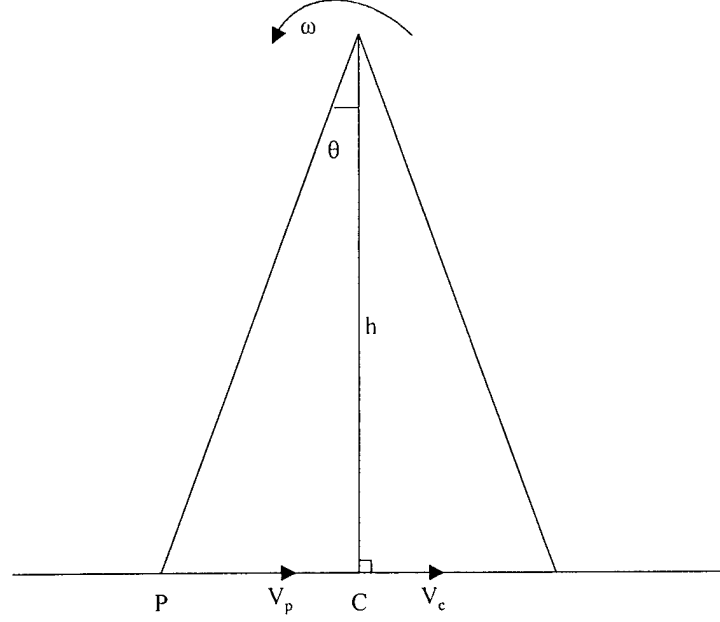


Figure 15. X-ray spot surface speed calculation diagram.

As indicated in the above derivation, the speed  $V_p$  of the x-ray spot at any location in a raster scan line is not a constant speed but a function of the x-ray beam incidence angle. When the x-ray generator is set at a certain voltage and current level, for a fixed size area at different locations along the raster scan line, a different amount of x-ray illumination occurs at different locations because of different x-ray dwell times on the given size area. Therefore, normalization algorithms need to be employed to ensure uniform illumination for each pixel.



### **Variation of the X-ray Illumination Spot Size**

For the illumination case where the x-ray beam always has perpendicular incidence to the scanned surface, the beam spot shape on the scanned surface is not changed. However in the case of the x-ray beam rotating collimator, with the changing of the beam incidence angle, the beam spot size varies accordingly. When the x-ray beam is away from the perpendicular incidence position, the beam spot on the scanned surface tends to be elongated in the beam raster scan direction. As the x-ray spot gets further away from the location of x-ray beam perpendicular incidence, the width of the beam spot becomes greater. If the spot area at perpendicular incidence is  $A$  and the x-ray incidence angle is  $\theta$ , the area of the x-ray spot at any location along the raster line is  $A/\cos(\theta)$ .

### **Definition of Resolution**

In the x-ray perpendicular incidence case, the data acquisition is executed when the system is still. Therefore, the definition of resolution is the exact size of the x-ray spot on the scanned surface. In the x-ray beam rotating collimator case, the continuous motion of the x-ray spot during the raster scan leads to a different definition of resolution in the raster scan direction than for the x-ray beam perpendicular incidence case.

In LMR, a certain number of photons are needed to illuminate each pixel to have reasonable photon quantum statistics. And to reach this number, a certain time is required to illuminate the pixel. Given the x-ray generator power and its focal spot distance to the ground, the required illumination time for a certain area by the LMR system is calculated as follows:

$$\text{x-ray effective power, } P \text{ (watts)} * \text{dwell time, } T_d \text{ (second/pixel)} = A \text{ (joule/pixel)}$$

where x-ray effective power = x-ray power \* (D / focal spot height)<sup>2</sup>

→  $T_d = [ A \text{ (joule/pixel)} / (\text{x-ray effective power in watts}) ] \text{ seconds.}$

A (joule/pixel) is the energy representation of the reasonable photon number required for good statistics. (i.e., yields approx. 10,000 detected photons per pixel)

D is a standard perpendicular distance from focal spot to the scanned surface.

First, the raster scan line is divided into squares called nominal pixels. Then the rotating collimator rotates constantly at a certain angular speed. Since a certain time is required to illuminate an area with a certain number of photons, during this period of time, the x-ray spot has traveled a certain distance BC or DE (Figure 16). Then the total illuminated area during this period of time, hereon named a real pixel, is greater than that of a nominal pixel, with a longer length in the raster scan direction. Therefore, the resulting image will have different resolution for the two orthogonal directions.

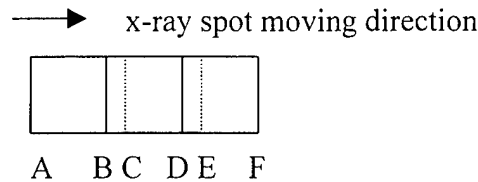


Figure 16. Illustration of the resolution definition.

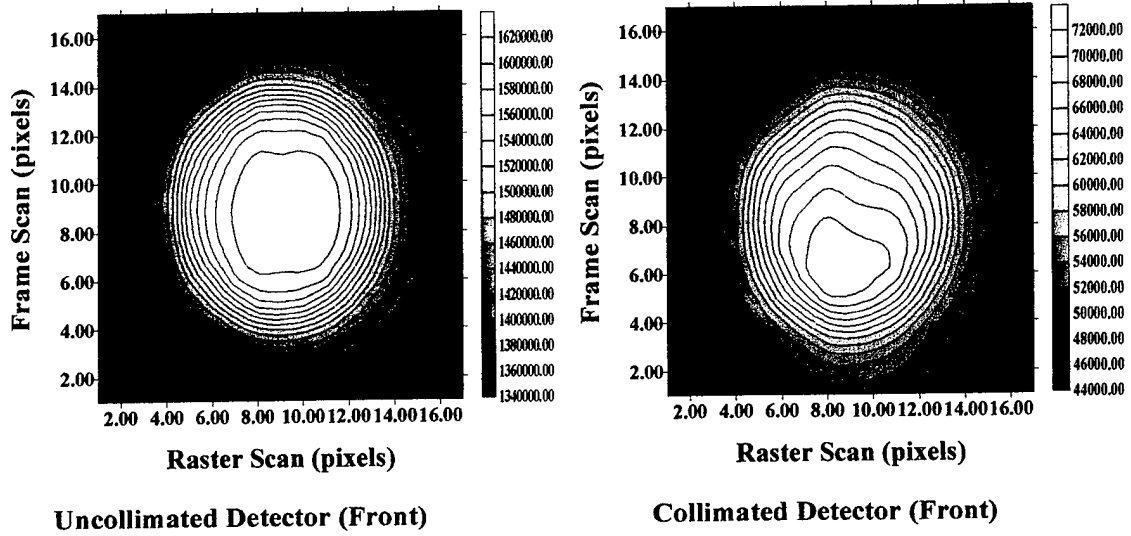
### Raster Direction Squeezing Effect

As the result of using the x-ray beam rotating collimator as part of the LMR system, the image formation is different than that of the case where the beam always has perpendicular incidence. In order to analyze the effect of the x-ray beam rotating collimator on the acquired images, several MCNP<sup>15</sup> simulations (Monte Carlo computer

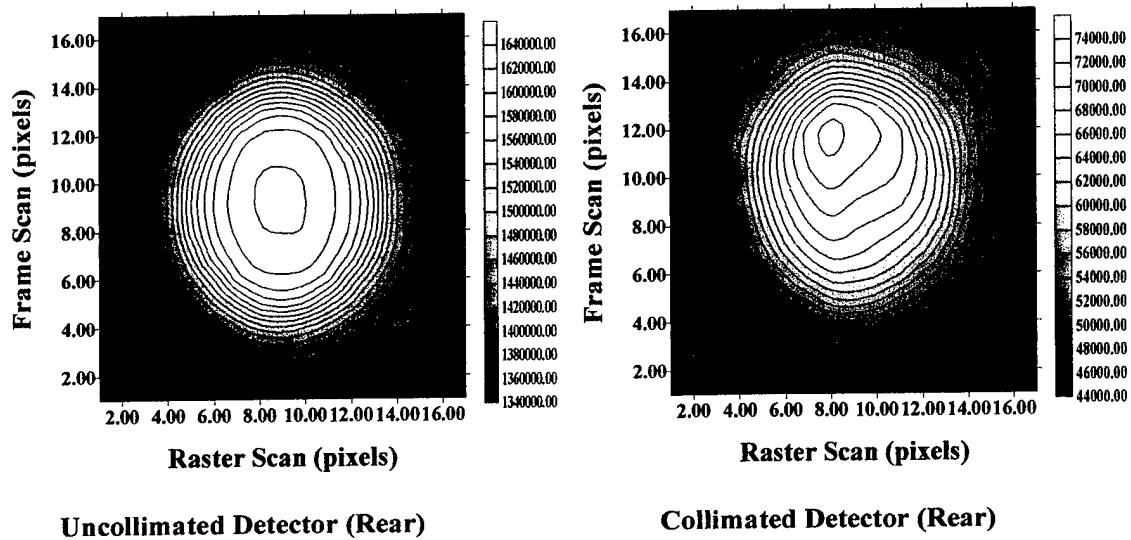
simulations) of buried land mines under x-ray beam angular incidence are carried out. The acquired images or data show different mine burial situations which include a 2.5 cm, 5 cm and 7.5 cm depth-of-burial cases as well as a uniform background with no mine buried case.

In Figure 17, the 2.5 cm depth-of-burial case, the mine is located at the center of the scanned area. This mine is a solid dummy mine which has no air space. The intensity decrease from the center of the object is not isotropic; in the raster scan direction, the decrease is relatively faster at the same distance from the center than that in the frame scan direction. This is named a raster direction squeezing effect. With an increase in the depth-of-burial, this effect gets much more noticeable. This can be seen in Figure 18 and Figure 19.

Geometric analysis shows, the cause of the squeezing effect is related to geometric projection between the pixel location and the real x-ray interaction location. In the LMR system, image pixel locations are defined by the x-ray beam locations on the scanned surface. For the case of an x-ray beam incident perpendicular to the scanned surface, the point where the x-ray beam vertical projection hits the object has the same pixel coordinate location as the source. For an x-ray beam with angular incidence from the rotating collimator, the incidence beam location on the soil and the location of where the x-ray beam interacts with the object, except for perpendicular incidence, have different coordinates. Because x-ray beam angular incidence is in the raster scan direction, the geometric length of a buried object in the raster direction is represented by a smaller length in the acquired images. In Figure 20, DE is the length in an LMR image, while AB, the actual length, is greater than DE.

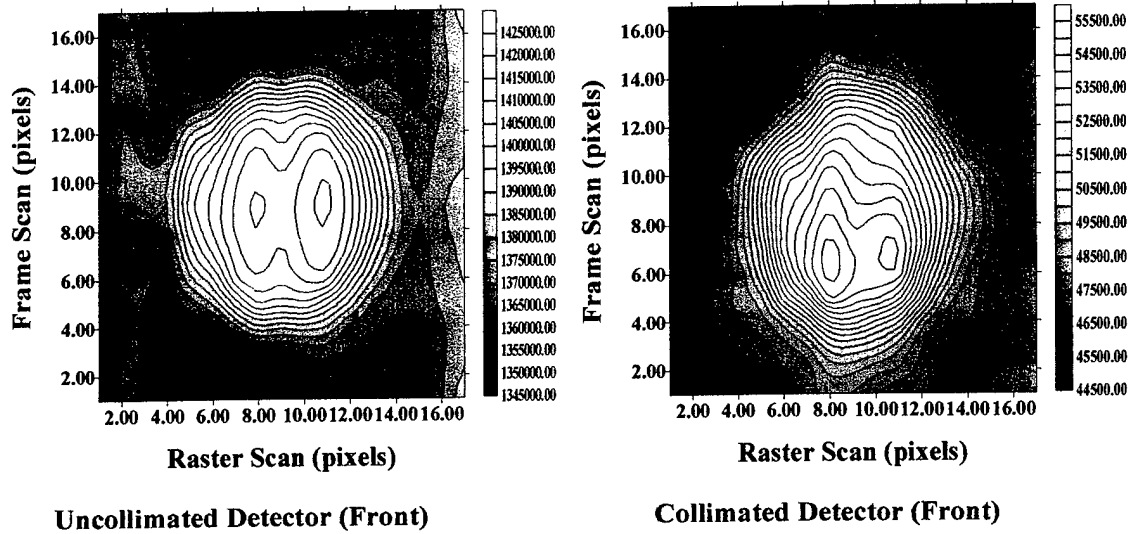


Dummy Mine, 2.5 cm DOB, 1.5 cm Pixel Size

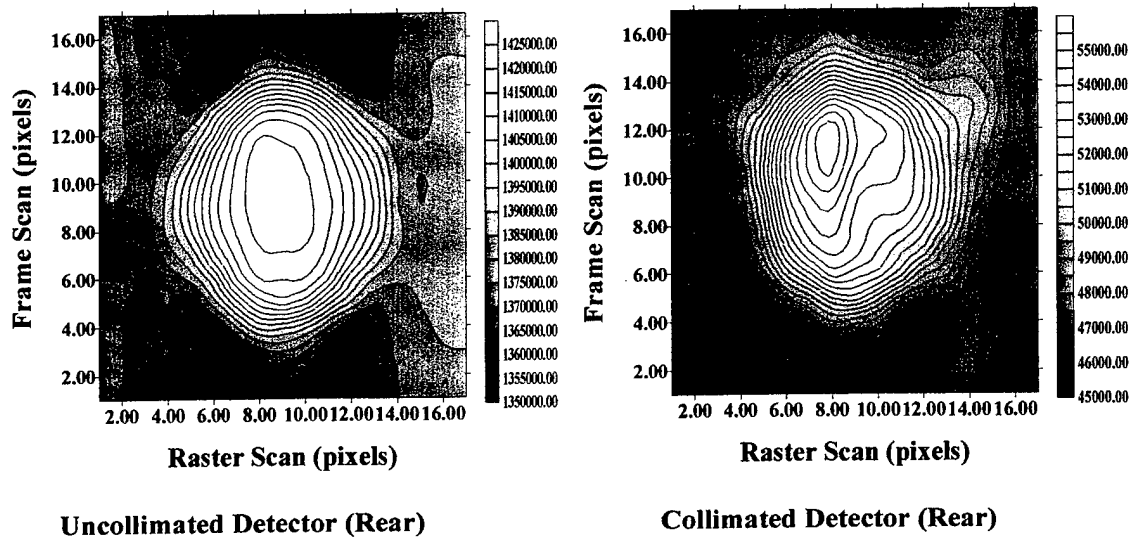


Dummy Mine, 2.5 cm DOB, 1.5 cm Pixel Size

Figure 17. MCNP simulation images under x-ray beam angular incidence  $-2.5\text{cm}$  DOB.

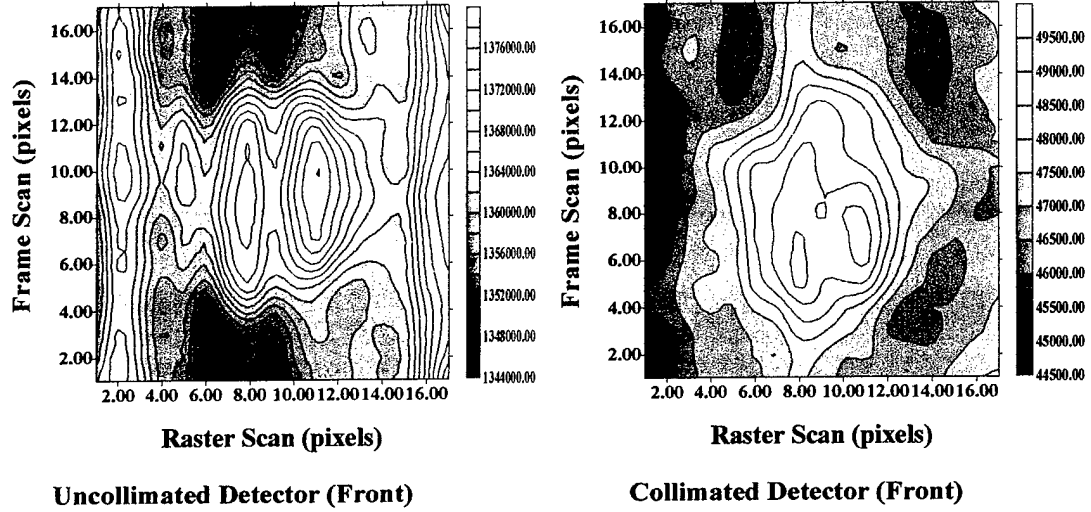


**Dummy Mine, 5.0 cm DOB, 1.5 cm Pixel Size**

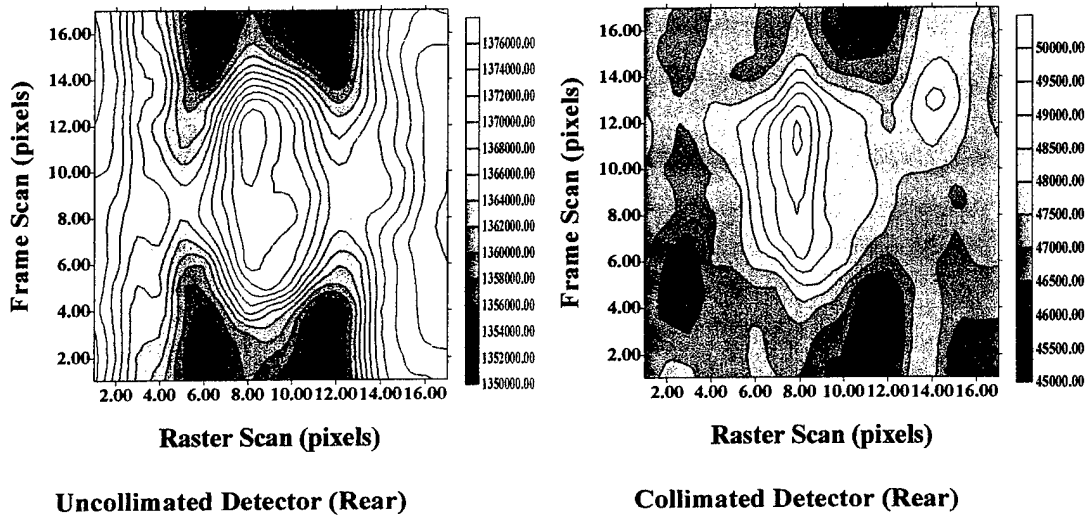


**Dummy Mine, 5.0 cm DOB, 1.5 cm Pixel Size**

Figure 18. MCNP simulation images under x-ray beam angular incidence -5 cm DOB.



**Dummy Mine, 7.5 cm DOB, 1.5 cm Pixel Size**



**Dummy Mine, 7.5 cm DOB, 1.5 cm Pixel Size**

Figure 19. MCNP simulation images under x-ray beam angular incidence  $-7.5$  cm DOB.

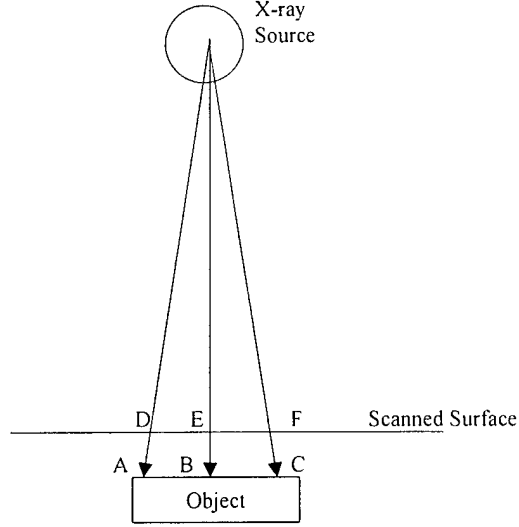


Figure 20. Illustration of raster direction scanning and its distortion in LMR images by x-ray beam angular incidence.

### Compton Interaction Angular Difference

In Figure 19, the 7.5 cm burial case, there are high intensity edges along the left and right end of the uncollimated detector images. This shows that there is another mechanism behind the image formation, the Compton interaction angular distribution. When x-ray photons interact with the electrons of the object and surrounding material, the angular distribution of the scattered x-ray photon is predicted by the Klein-Nishina formula, which is presented as the differential scattering cross section  $d\sigma/d\Omega$ :

$$\frac{d\sigma}{d\Omega} = Zr_0^2 \left( \frac{1}{1 + \alpha(1 - \cos\theta)} \right)^2 \left( \frac{1 + \cos^2\theta}{2} \right) \left( 1 + \frac{\alpha^2(1 - \cos\theta)^2}{(1 + \cos^2\theta)[1 + \alpha(1 - \cos\theta)]} \right)$$

where  $\alpha = hv/m_0c^2$ ,  $Z$  is atomic number,  $r_0$  is the classical electron radius and  $\theta$  is the scattering angle.

When the x-ray photon is at a high energy level, forward scattering is dominant. The major part of the x-ray spectrum used in LMR system is in the range of 40 to 60 keV,

which has a slightly forward preference in the photon scattering distribution. This anisotropy will result in an intensity difference of backscattered photons when the case of x-ray beam perpendicular incidence is compared with the case of x-ray beam variable angular incidence. This can be seen in the MCNP simulation image data of the uniform background case. Since there is no heterogeneous object in the scanned area, theoretically the signal intensity of each pixel should be approximately the same. In the uncollimated detector image data of the angular incidence case (Table 1), there is clear evidence that when the x-ray beam approaches a greater scanning angle, the backscattering signal is higher. The signal difference between the x-ray beam at the (0,0) position and the (0,8) position is about 1.7 % while the standard deviation of the data is about 0.1 %. This means that the 1.7 % signal difference is definitely not from the statistical fluctuation of the simulation and very probably it is from the Compton scattering angular distribution. For the uncollimated detector image data of the x-ray beam perpendicular incidence case (Table 2), the signal difference is about 0.4 % and has the same standard deviation as the angular incidence case.

When a subsurface object has shallow depth, the signal is much greater than the variation caused by the Compton interaction angular difference. As the object depth is greater, the signal-to-noise ratio approaches one and the Compton interaction angular preference effect shows up in the image. The reason this effect shows clearly in uncollimated detector data is that uncollimated detectors register predominantly once collided photons which carry the signature of the different Compton interaction angular difference effect associated with the x-ray beam incident angle. The multiple collided photons, which are registered mostly by collimated detectors, have experienced several



Compton interactions and the initial difference of Compton interaction angular difference caused by different x-ray incidence angles has been greatly smoothed out. As shown in Table 1, the collimated detector signal difference is about 0.7 %, the standard deviation is about 0.3 %, and there is no clear sign of the Compton interaction angular difference effect because multiple collided photons are mainly registered by the collimated detectors.

Table 1. Half raster scan line data of uniform background under x-ray beam angular incidence.

Position	Front Collimated Detector		Rear Collimated Detector		Front Uncollimated Detector	
	Energy Deposition	Relative Error	Energy Deposition	Relative Error	Energy Deposition	Relative Error
0,0	7.84E-10	0.0027	7.84E-10	0.0025	2.30E-08	0.0007
0,1	7.88E-10	0.0028	7.87E-10	0.0026	2.30E-08	0.0007
0,2	7.90E-10	0.0029	7.86E-10	0.0026	2.30E-08	0.0007
0,3	7.87E-10	0.003	7.85E-10	0.0025	2.30E-08	0.0007
0,4	7.87E-10	0.0027	7.84E-10	0.0026	2.31E-08	0.0007
0,5	7.88E-10	0.0026	7.89E-10	0.0026	2.31E-08	0.0007
0,6	7.90E-10	0.0028	7.91E-10	0.0027	2.32E-08	0.0007
0,7	7.88E-10	0.0028	7.88E-10	0.0027	2.33E-08	0.0007
0,8	7.89E-10	0.0028	7.91E-10	0.0027	2.34E-08	0.0007

Table 2. Half raster scan line data of uniform background under x-ray beam perpendicular incidence.

Position	Front Collimated Detector		Rear Collimated Detector		Front Uncollimated Detector	
	Energy Deposition	Relative Error	Energy Deposition	Relative Error	Energy Deposition	Relative Error
0,0	7.87E-10	0.0027	7.84E-10	0.0025	2.30E-08	0.0007
0,1	7.86E-10	0.0028	7.85E-10	0.0025	2.30E-08	0.0007
0,2	7.84E-10	0.0029	7.83E-10	0.0025	2.30E-08	0.0007
0,3	7.86E-10	0.0028	7.81E-10	0.0025	2.30E-08	0.0007
0,4	7.86E-10	0.003	7.81E-10	0.0025	2.29E-08	0.0007
0,5	7.86E-10	0.0029	7.82E-10	0.0025	2.29E-08	0.0007
0,6	7.84E-10	0.0026	7.81E-10	0.0025	2.29E-08	0.0007
0,7	7.82E-10	0.0028	7.80E-10	0.0026	2.29E-08	0.0007
0,8	7.80E-10	0.0028	7.79E-10	0.0026	2.29E-08	0.0007

## CHAPTER 4 ROTATING COLLIMATOR UNIQUE IMAGE ACQUISITION ALGORITHMS AND IMAGE ANALYSIS

### Image Acquisition Algorithms

#### Analysis

As discussed in Chapter 3, non-uniform speed of the x-ray beam raster scan on the imaged surface and beam spot size variation along the raster scan line are two of the effects that affect the image data acquisition scheme. Definition of resolution in the raster direction of acquired images is a key to understanding the resolution difference between the raster scan direction and motion direction. Two different image data acquisition algorithms are studied and tested based on different objectives. The first data acquisition algorithm is based on a uniform x-ray illumination area. In this scheme, sampled data points are assigned to different pixels according to their corresponding physical locations. This scheme causes non-uniform illumination among different pixels which can be mathematically compensated for after the image acquisition. The second data acquisition algorithm is based on uniform x-ray illumination time for each pixel. This scheme causes non-uniform pixel size along the raster scan direction which increases the complexity of the definition of resolution in the image raster scan direction. The first scheme is used in the image data acquisition process.

In the raster scan of image acquisition, the x-ray beam spot has a non-uniform speed on the scanned surface. It observes the following relationship:

$$V_p = V_c / \cos^2(\theta)$$

where  $\theta$  is x-ray beam incidence angle relative to perpendicular incidence (see Figure 15).

The speed of the x-ray beam spot is a function of its location. It scans faster at locations away from perpendicular incidence. However, the data acquisition card can only sample detector signals at a certain constant rate. If uniform pixel size is preferred, because of the non-uniform speed of the x-ray spot on the scanned surface, the data acquisition time for each pixel must be different. Then, the x-ray illumination of each pixel is different, which means that image distortion (artificial intensity variation) is introduced into images. By the same token, if uniform data acquisition time is preferred, the corresponding scanned area of each data acquisition time interval is not uniform which means that non-uniform image resolution in the image raster direction is introduced. These two cases are analyzed in the following sections.

## **Sampling Methods**

### **Uniform pixel size scheme**

In this scheme, the underlying principle is that images should have uniform resolution along the raster scan direction. Assume the x-ray beam rotating collimator angular speed is  $\omega$ , the data acquisition rate is  $f$ , x-ray output power is  $p$ , pixel illumination intensity is  $I$  and the number of sampled data points for each pixel is  $n$ . (for all other parameters, refer to Figure 21). Following is a development of pixel illumination intensity as a function of pixel location.

$$\Delta x = x_{i+1} - x_i = h * (\tan(\theta_{i+1}) - \tan(\theta_i)) = \text{constant}$$

$$\Delta \theta = \theta_{i+1} - \theta_i = \arctan(x_{i+1}/h) - \arctan(x_i/h)$$

$$\omega = \Delta \theta / \Delta t \quad \rightarrow \quad \Delta t = \Delta \theta / \omega = [\arctan(x_{i+1}/h) - \arctan(x_i/h)] / \omega$$

$$I = p * \Delta t = p * [\arctan(x_{i+1}/h) - \arctan(x_i/h)] / \omega$$

$$n_i = f * [\arctan(x_{i+1}/h) - \arctan(x_i/h)] / \omega$$

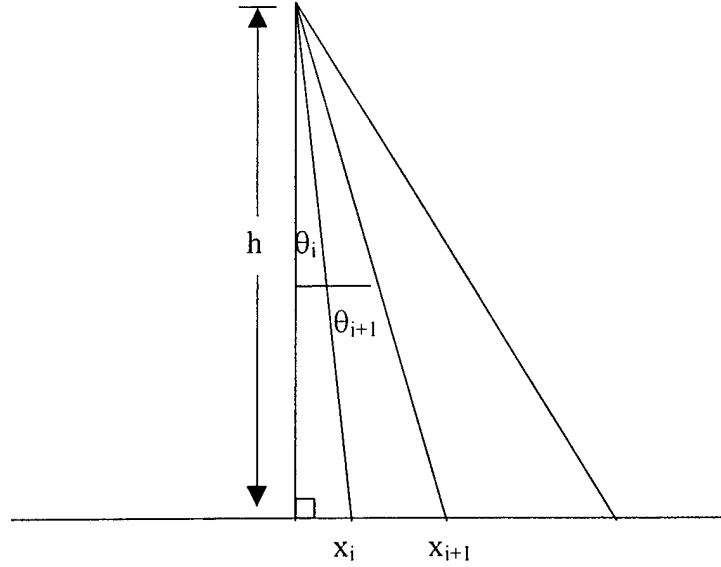


Figure 21. X-ray incidence geometry

The above development assumes that the x-ray beam spot size is constant at different x-ray beam angular incidences. In reality, the x-ray beam spot size changes as the x-ray incidence angle changes. It is elongated as the x-ray beam moves away from the perpendicular incidence. Therefore, by using the above data acquisition scheme, acquired images still have non-uniform pixel size along the image raster scan direction. To achieve uniform pixel size along each raster scan line, the above data acquisition scheme needs to be modified to accommodate pixel elongation at different x-ray incidence angles. The following is the development.

$C$  = constant, the length of the x-ray beam spot of perpendicular incidence

$X$  = total length along raster scan line

$M = X / C$ , is total number of pixels

$$\Delta x = x_{i+1} - x_i = C * \cos(\theta_i) = C * \{h / \sqrt{h^2 + x_i^2}\}, \text{ where } x_1 = 0$$

$$\Delta \theta = \theta_{i+1} - \theta_i = \arctan(x_{i+1}/h) - \arctan(x_i/h)$$

$$\Delta t = \Delta \theta / \omega = [\arctan(x_{i+1}/h) - \arctan(x_i/h)] / \omega$$

$$= \{\arctan(x_i + C * [h / \sqrt{h^2 + x_i^2}]) - \arctan(x_i/h)\} / \omega$$

$$n_i = f * \{\arctan(x_i + C * [h / \sqrt{h^2 + x_i^2}]) - \arctan(x_i/h)\} / \omega$$

As indicated by the above development, the pixel illumination intensity indeed is a function of pixel location. The pixel illumination intensity is higher near the center of an image than at the edges. This artificial pixel illumination intensity variation needs to be corrected to achieve uniform pixel size and pseudo-uniform pixel illumination. The correction function is obtained by first normalizing the pixel illumination intensity values and then taking their reciprocals. Multiplying each correction coefficient by the corresponding pixel value yields a backscatter field from uniform pixel illumination.

### **Uniform illumination time scheme**

In this scheme, there is a uniform time period for each pixel which means uniform x-ray illumination for each pixel. However, the size of each pixel is not uniform; pixels away from perpendicular incidence are larger than ones near it. This is shown in the following development.

From Chapter 3,  $V_p = V_c / \cos^2(\theta)$  where  $V_c = h * \omega$ . Define  $S$  as the pixel length along the raster direction,  $\theta$  as the x-ray fan beam angle,  $N$  as the total number of pixels. And all other parameters refer to Figure 21.

$$\Delta \theta_i = (\theta_{i+1} - \theta_i) = \theta / N = \text{constant, angle subtended by each pixel to the x-ray focal spot}$$

$$\Delta t = t_{i+1} - t_i = \text{const} = (\theta_{i+1} - \theta_i) / \omega, \quad t_1 = 0$$

$$S = \int_i^{i+1} V_p dt = \int_i^{i+1} V_p \frac{dt}{d\theta} d\theta = h * \int_{\theta_i/\omega}^{\theta_{i+1}/\omega} 1/\cos^2(\theta) d\theta$$

$$S = h * [\tan(\theta_{i+1}) - \tan(\theta_i)]$$

The pixel elongation effect along the raster direction has the following relationship:

$$S_p = S_c / \cos(\theta)$$

$S_c$  is raster direction length of x-ray beam spot under perpendicular incidence

$S_p$  is raster direction length of x-ray beam spot under angular incidence

Therefore,  $S_p = h * [\tan(\theta_{i+1}) - \tan(\theta_i)] / \cos(\theta_i)$ .

The above development shows that the raster length of each pixel is a function of the x-ray beam incidence angle. In this uniform illumination scheme, the non-uniform pixel size can not be corrected. The artificial resolution difference along the raster scan is always in the acquired images. Comparing the two data acquisition schemes, the uniform pixel size scheme has a clear advantage. It not only has uniform pixel size, but also has uniform x-ray illumination intensity for each pixel after applying the correction algorithm. Therefore, the uniform pixel size data acquisition scheme is used in the measurements.

### Image Analysis

Though the uniform pixel size data acquisition scheme is used in measurements and the image raster direction has uniform resolution, there is still a resolution difference between the raster scan direction and the frame scan direction in the image. As discussed in Chapter 3, the x-ray beam spot on the scanned surface for the perpendicular incidence case is defined as the nominal pixel, and a real pixel is always greater than the nominal

pixel along the raster direction because of the movement of the x-ray beam spot caused by the rotating collimator. This resolution difference of two orthogonal directions can not be eliminated because the x-ray beam spot needs to move to scan. However, the resolution difference can be reduced to a certain level through a data processing algorithm.

### Linear Asymmetric Weighting Algorithm

For the uniform pixel size data acquisition scheme, when suitable parameters are selected, a real pixel size is twice as big as that of a nominal pixel along the raster scan direction. And two adjacent real pixels have an overlap of the size of one nominal pixel (Figure 22). Sampled data points for each real pixel are summed to represent the intensity of backscattered x-ray photons.

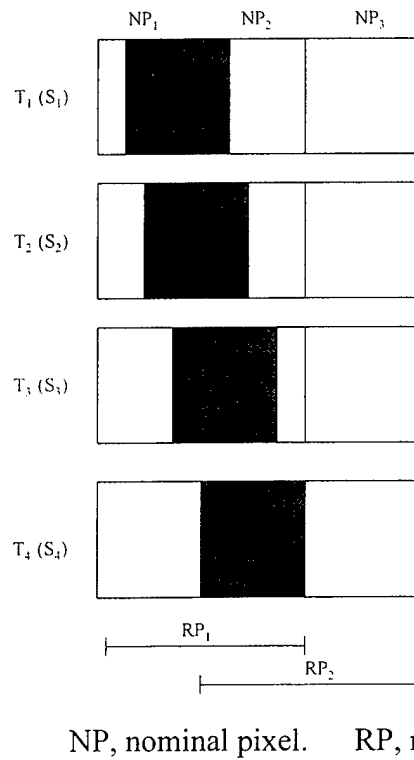


Figure 22. Nominal pixel and real pixel relation geometry.

In Figure 22, sample  $S_i$  corresponds to time  $T_i$ . Thus, each sample relates to a certain x-ray illumination spot on the scanned surface. Using the uniform pixel size scheme, when the x-ray illumination spot fills the second nominal pixel precisely, the first real pixel scan is finished and all the samples of the real pixel are summed together as the first nominal pixel image intensity in the acquired images. Similar events happen for the second real pixel and there is one nominal pixel area overlap between the two real pixel scans. This means that in each nominal pixel image intensity, there is always information contributed from its adjacent nominal pixel, and the later samples in the real pixel scan has more information from the second nominal pixel than from the first one. In order to reduce the information content from second nominal pixel, a linear asymmetric weighting algorithm is introduced to process the sampled data of each raster scan. As illustrated in Figure 23, this algorithm gives more weight to samples containing more information from the first nominal pixel and gives less weight to samples containing more information from the second nominal pixel. In this way, information from the first nominal pixel is emphasized. There is some, but very limited resolution improvement in the raster direction in Figure 24, which shows collimated detector images of a 15 cm diameter plastic surrogate mine buried 2.5 cm deep in soil. In the rotating collimator, a V-belt is employed to drive the rotating collimator. The belt slips during the rotation of the rotating collimator which presents a certain level of randomness in the raster line of the acquired images. This randomness, even though is not significant to distort the acquired image in a dramatic fashion, it can affect the performance of the algorithm. However, the above algorithm is not the best one to improve the image resolution, a linear symmetric weighting algorithm is developed and presented in appendix D.



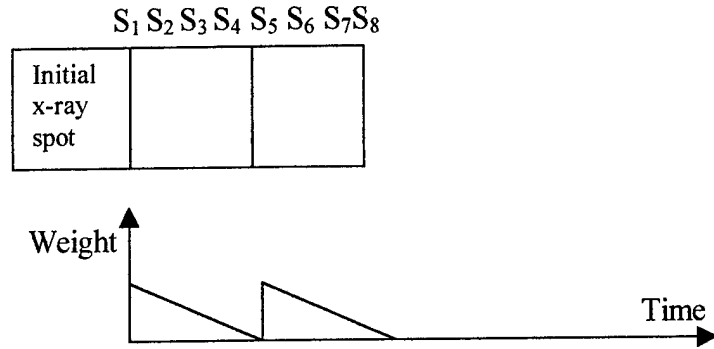


Figure 23. Illustration of linear asymmetric weighting algorithm.

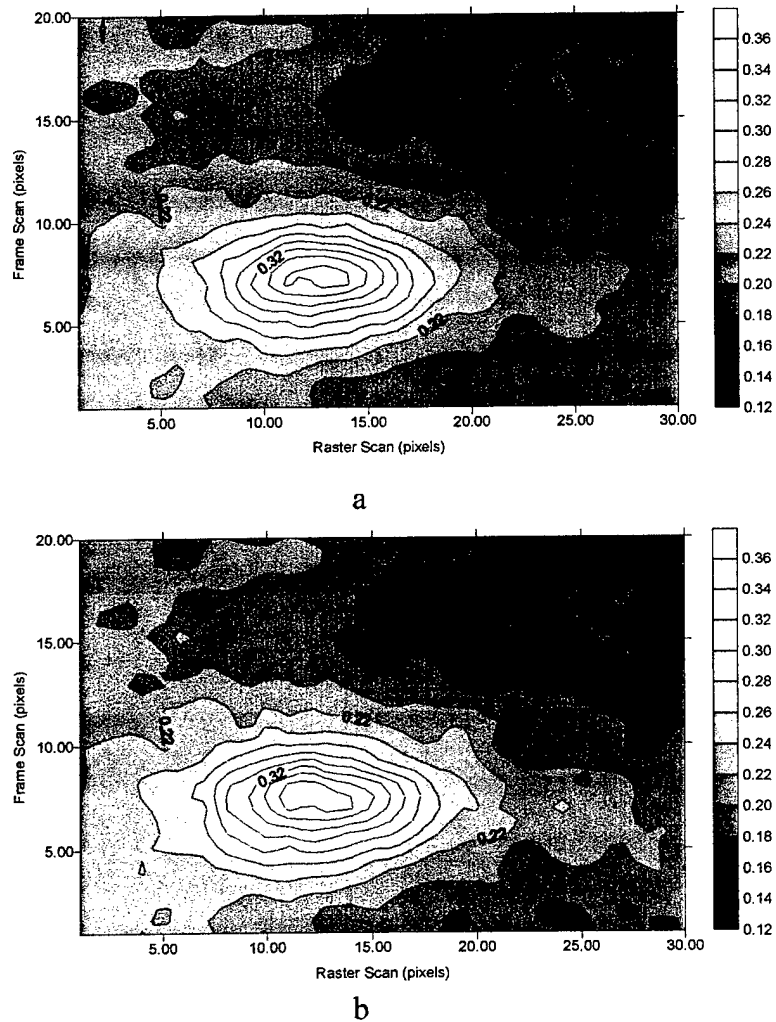


Figure 24. Comparison of collimated detector images of before and after linear asymmetric weighting filter. a) Image of data before linear asymmetric weighting filter; b) Image of data after linear asymmetric weighting filter.

### **Comparisons of Measurement Images and MCNP Images**

In Chapter 3, MCNP simulations show that there is a raster direction squeezing effect in images. However, there is no trace of this effect in any acquired measurement image (Figure 25). Reviewing the MCNP simulation algorithm and measurement parameters, two factors could lead to this difference. First, in MCNP simulations, the signal-to-noise ratio, to some extent, is controlled by the total number of illumination photons per pixel. The user can increase the ratio by increasing the number of photons per pixel. In the measurements, the leakage field strength of the x-ray generator dictates the signal-to-noise ratio. In the current measurement setup, about 2 % of the detected photons are from generator leakage. In the MCNP simulations, a “perfect” source with no leakage is used. The generator leakage effect makes it more difficult to observe raster direction squeezing effect in any acquired measurement image. Secondly, in the MCNP simulations, the raster scan is implemented as a stepping-coordinate pixel illumination rather than as a continuous illumination. In this case, a nominal pixel is a real pixel and there is no raster resolution definition difficulty. The geometric projection effect discussed in Chapter 3 is presented in simulation images without any distortion. However, in measurements, continuous movement of the x-ray illumination spot reduces the differences between adjacent pixel intensity, and therefore, reduces the contrast of the squeezing effect in the image raster direction of measurement images. Future MCNP simulations should simulate continuous movement of x-ray illumination spot on the scanned surface to examine the similarity and difference between the MCNP and measurement images.

In the MCNP simulation images in Chapter 3, there is an intensity increase along two sides of the uncollimated detector images for the three inch burial case. This is shown to be due to a Compton interaction angular difference. However, there is no intensity increase in the corresponding measurement images. The main factor is signal-to-noise ratio. The 2 % x-ray generator leakage field is strong enough to mask the Compton scatter angular difference which is less than two percent in the MCNP simulation images.

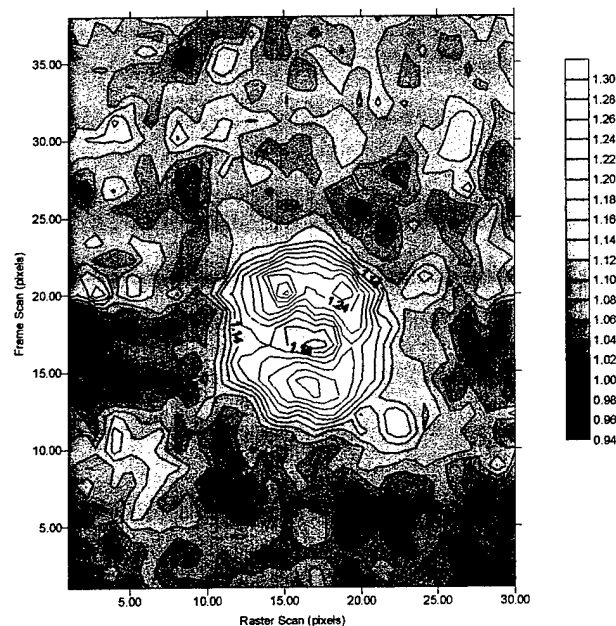
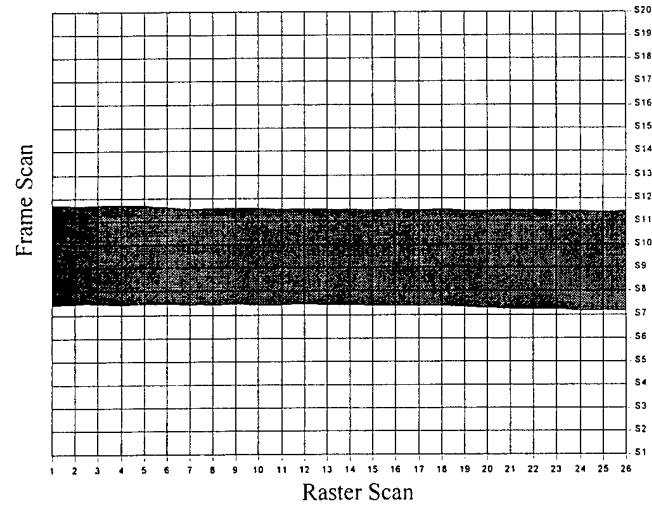


Figure 25. LMR uncollimated detector image of 15 cm diameter plastic surrogate mine buried at 2.5 cm.

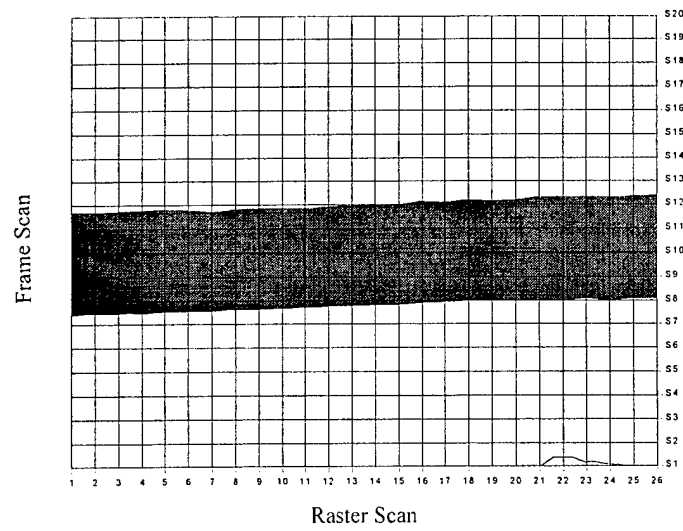
### Image Processing

The combined motion of the rotating collimator and the x-ray generator and detector assembly leads to a slant scan trace of the x-ray illumination spot. This should lead to every object in the plotted images shifting towards the lower right corner. In order to get data points on a rectangular grid, interpolation correction of the original image data

is employed. A 4 cm wide steel bar is laid on the soil surface and its orientation is orthogonal to the assembly motion direction. It is scanned to generate an LMR uncollimated detector image. Both the original data image and the interpolation corrected data image are presented in Figure 26. As indicated in the original data image, the slant scan trace leads to maximum half pixel tilt to the lower right corner compared to one pixel of theoretical value. Several factors can contribute to this difference. First, simple human error could result in the bar not being placed exactly orthogonal to the motion direction. Secondly, a certain fraction of multiple scattered photons is registered by the uncollimated detectors. Multiple scattered photons carry additional information from areas other than the x-ray illumination spot which blurs differences between the steel bar and its surrounding soil. So, in each raster scan, there is only a half pixel tilt to the lower right corner of the image. In the interpolation corrected image, there is no object tilting to the lower right corner. However, there is object tilting by half a pixel to the upper right corner of the image. This is from the image interpolation correction of which each raster scan line, from the leftmost to the rightmost pixel, has shifted the data one pixel length upwards in the frame scan direction. However, the image interpolation introduces a certain level of image averaging which results in blurring of image details. Furthermore, the level of tilting (rotation) is very small, for large object detection application, e.g., land mine detection, it is hardly noticed. Therefore, the images without image interpolation processing are also acceptable.



a



b

Figure 26. LMR images of a steel bar laid on soil surface. a) Original image; b) Interpolation corrected image.

## CHAPTER 5 GENERAL LMR IMAGE PROCESSING AND PATTERN RECOGNITION ALGORITHMS

### **Image Enhancement**

All real images contain noise, e.g., quantum noise, electronic noise, etc.. In LMR images, random noise and quantum noise are major reasons for the existence of image speckles.<sup>16</sup> During image acquisition, other photon sources compete with x-ray photons. They include gamma ray photons and cosmic rays. Compared to x-ray photons, gamma ray photons have a higher energy and cosmic rays have an extremely high energy level. Gamma rays are emitted from surrounding materials and cosmic rays come from outer space. For x-ray photons, because of the limited power of the x-ray generator and the nature of Compton backscattering, the total number of backscattered x-ray photons registered by the detectors is limited; therefore, photon statistical variation is noticed in some LMR images. Gamma rays and cosmic rays are impulse noises which cause high intensity image pixels at random positions. X-ray statistical variation causes pixel values either higher or lower than the mean value. These are salt and pepper noises which are random black and white spots in the acquired images. Electronic noise exists in the LMR system, but because of the design of the electronic system and modern technologies, this noise is suppressed to a very low level. Therefore, major noises in LMR images are “salt and pepper noise” and impulse noise. In order to remove or suppress these noises to improve image quality, image filtering is employed. The employed filters include mean filter or local averaging filter, median filter and Weiner filter.<sup>17</sup>

The local averaging filter is a linear filter. In a 4-connected or 8-connected neighborhood window of an image pixel, certain weights are assigned to these pixels and the weighted sum of these pixel values is the filtered value of the center pixel. This filter is spatially invariant which means that the same weight assignment applies to each connected neighborhood window. In Figure 27, there are two typical local averaging filters: one is a 4-connected neighborhood filter, the other is a 8-connected neighborhood filter.

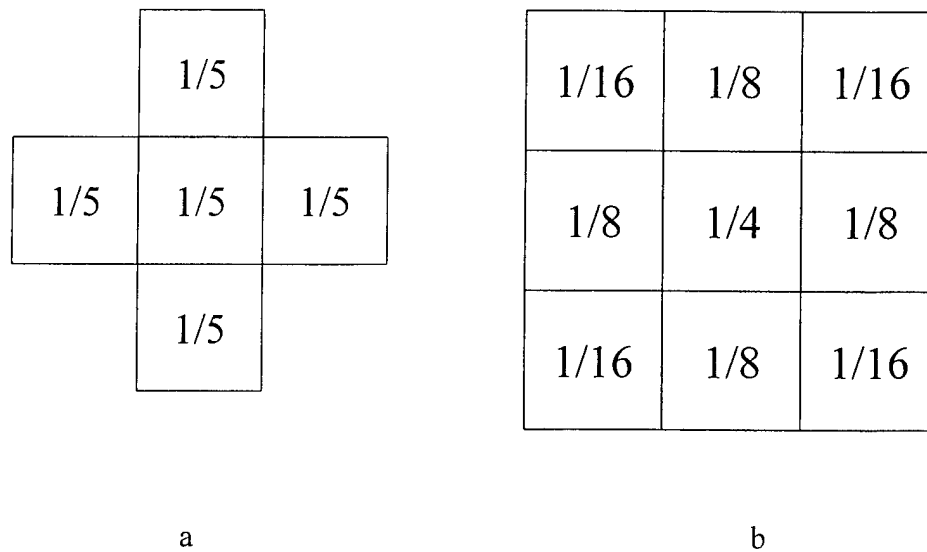


Figure 27. Local averaging filter masks. a) 4-connected neighborhood mask; b) 8-connected neighborhood mask.

In Figure 28, a 15 cm diameter plastic surrogate mine is buried one inch deep in soil. There are a number of isolated intensity increases and intensity decreases in the image. These are salt and pepper noise and impulse noises. After applying 4-connected and 8-connected neighborhood filters, some of the noises are removed, but

there is still a certain level present in the images. The filtered images are in Figure 29 and Figure 30.

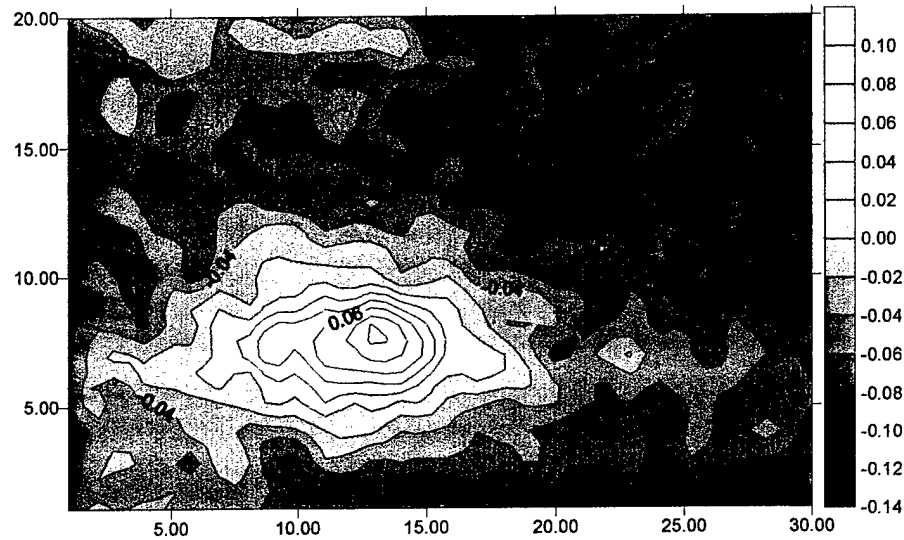


Figure 28. Original LMR uncollimated detector image of a 15 cm diameter plastic surrogate mine buried 2.5 cm deep in soil.

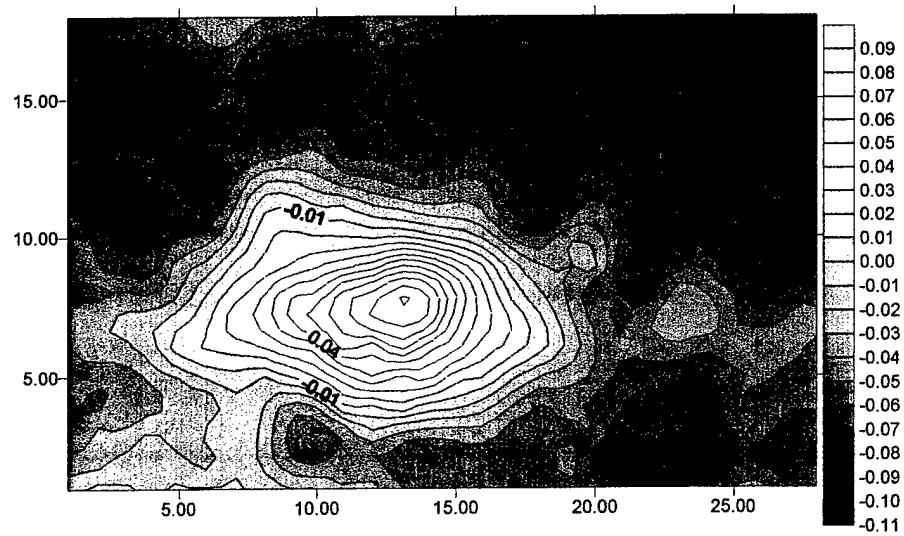


Figure 29. Local averaging filtered images of image of Figure 26. The image filter is 4-connected neighborhood local averaging filter.



Comparing the two different local average filters, the 8-connected neighborhood local average filter removes more noise than the 4-connected neighborhood local averaging filter. This is within expectation, since the 8-connected neighborhood local averaging filter averages pixel values from a larger area than the 4-connected neighborhood local averaging filter. Comparing unfiltered image and filtered images, certain sharp intensity changes from the object to the background in the original image are blurred into gradual changes in filtered images. This is a drawback of the local averaging filter.

When salt and pepper noise and impulse noise exist in an image, a local averaging filter can only remove a certain level of these noises. One of the best filters to remove these noises is a median filter. A median filter is a nonlinear filter which means that it is not a weighted sum of pixels in successive windows like the local averaging filter. In a median filter, within a certain size neighborhood, the median of all the pixel values is selected and assigned to the center pixel. Applying the median filter, isolated pixel intensity value increases and decreases are removed efficiently and the sharp discontinuities in the original image are preserved (Figure 31). Another effective filter applied to LMR images is the Wiener filter. The Wiener filter is a linear adaptive filter. When variance of a selected neighborhood is large, the filter does little smoothing; when variance of a selected neighborhood is small, the filter performs more smoothing. Therefore, it performs better than a comparable local averaging filter (Figure 32). Even though the Wiener filter performs best when noise is constant power additive noise, it still removes the majority of the salt and pepper and impulse noise in the LMR image.

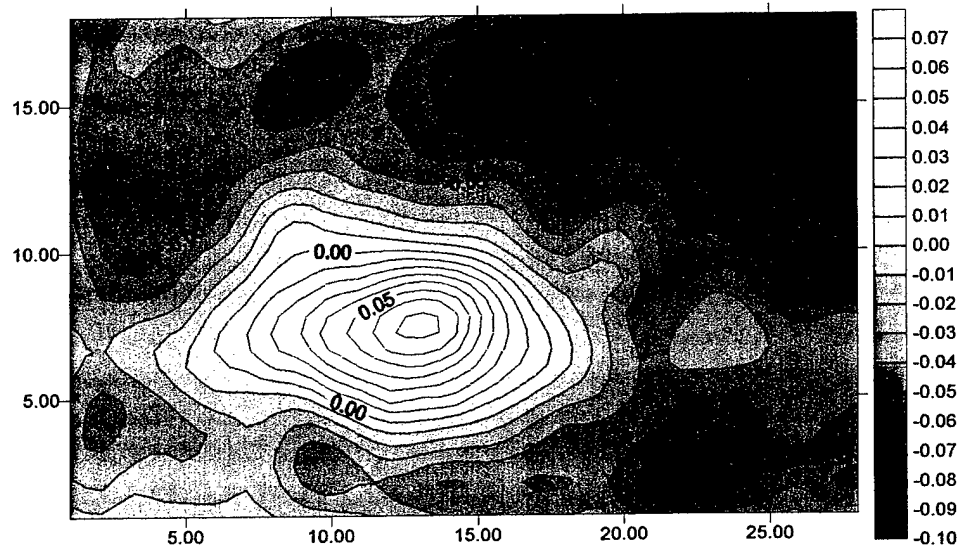


Figure 30. Local averaging filtered image of image in Figure 28. The image filter is 8-connected neighborhood local averaging filter.

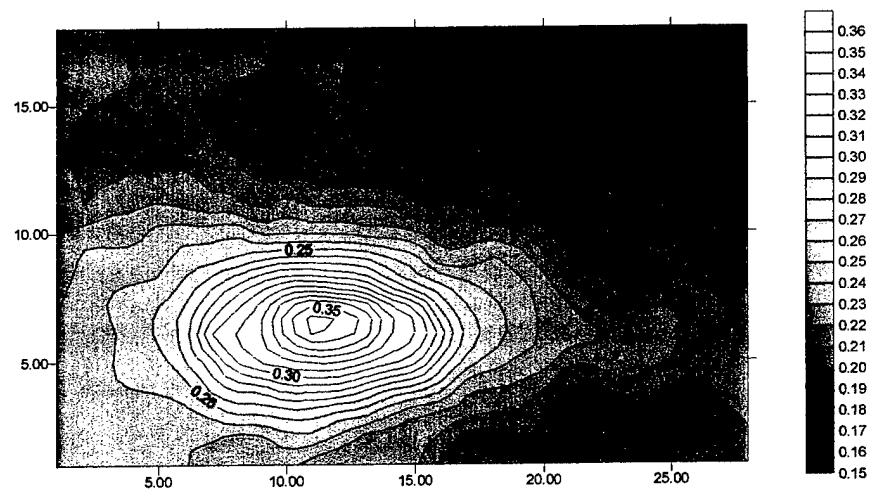


Figure 31. Median filtered image of image of Figure 28.

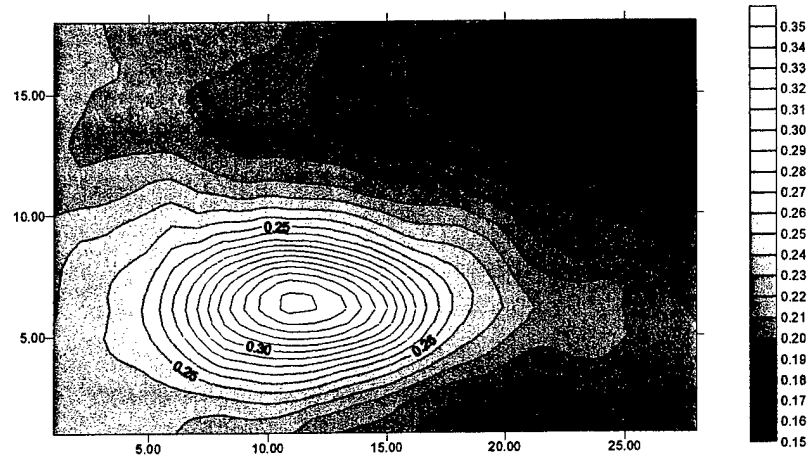


Figure 32. Wiener filtered image of image of Figure 28.

### Image Segmentation

After image filtering, objects in filtered images are usually well-defined and can be processed further to acquire more information from the images. Image segmentation is an effective method to separate different objects in the images into different regions for individual processing. Segmentation can be accomplished through various methods; thresholding is one of these techniques. In this section, an iterative threshold selection algorithm<sup>18</sup> is used to obtain a threshold to separate objects from background.

Iterative threshold selection algorithm:

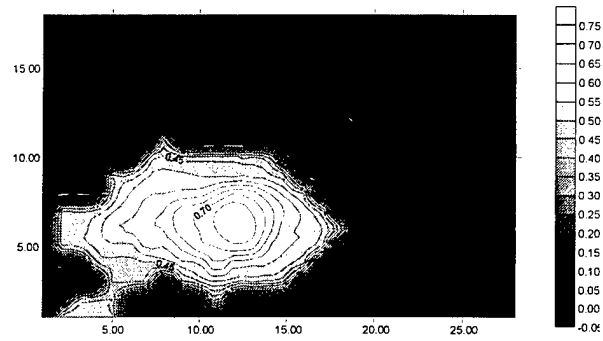
1. An initial threshold is selected to partition an image into two parts. Here the initial threshold is an average value of the image intensity.
2. Then an average of each part of the image is computed, the higher value average is  $\mu_1$  and lower value average is  $\mu_2$ .
3. A mean of these two averages is calculated as a new threshold to re-partition the image.

4. Repeat steps 2 and 3 until the new threshold is the same value as the old threshold.

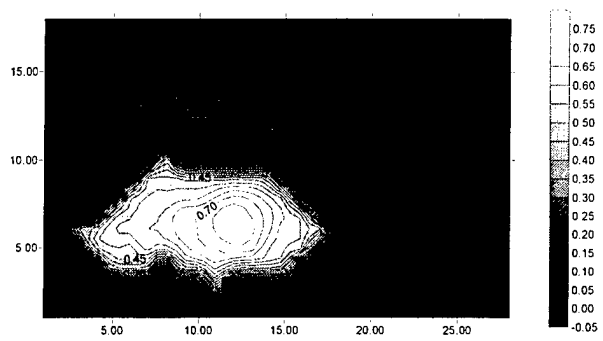
Using the image in Figure 31 as input, the above algorithm is applied and the segmented image is shown in Figure 33a. In the segmented image, the background is eliminated and assigned zeros.

After image filtering and segmentation, some LMR images may have small artifacts such as isolated peaks or lingering tails. These artifacts usually can be eliminated through image morphology operations. The erode operation is used in the image processing program for artifact elimination. Since the morphology operations usually work on black and white images, a black and white copy of the segmented image is obtained as an image map in the erode operation. In this operation, a certain size neighborhood block is specified and used as an eraser to remove any similar shape in the black and white image. After the erode operation, the original segmented image is updated based on changes in the eroded black and white image. The neighborhood block used in the program is shown in Figure 34. Using this block shape, both isolated peaks and lingering tails are usually removed from the filtered and segmented images (Figure 33b).

The above iterative threshold selection algorithm partitions a single image into two images. One is an image with objects and the other is background. When objects with high Compton scatter cross sections and objects with high photoelectric effect cross sections are both present in the same imaged area, one of them will be incorrectly classified into the background image. A small modification of the above algorithm can partition images correctly when both types of objects are present.



a



b

Figure 33. Median filtered image and its corresponding segmentation image of a 6 inch diameter surrogate mine buried 1 inch deep in soil. a) Segmentation image; b) Neighborhood eroded image of segmented image.

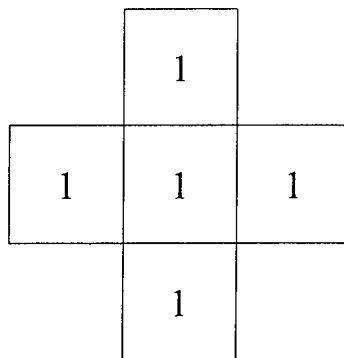
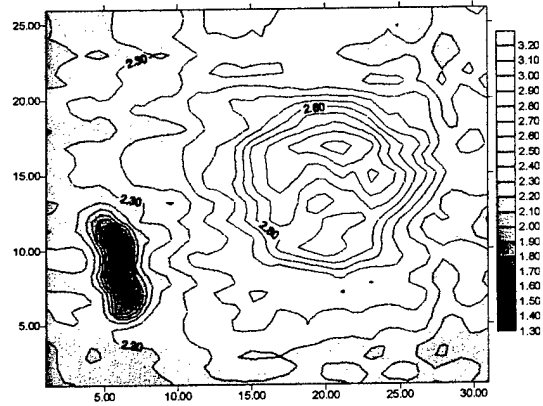


Figure 34. Neighborhood block used in image morphology operation.

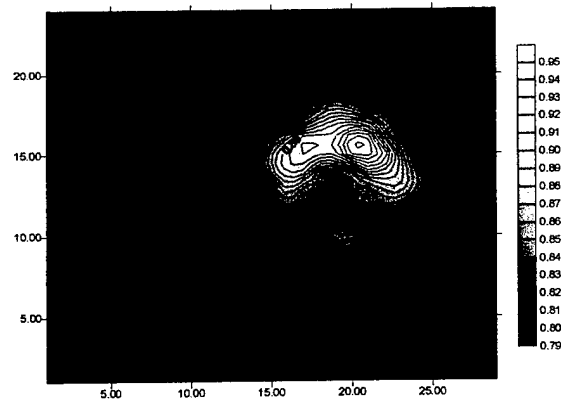
Modified iterative threshold selection algorithm:

1. An initial threshold is selected to partition an image into two parts. Here the initial threshold is an average value of the image intensity.
2. Then an average of each part of the image is computed, the higher value average is  $\mu_1$  and lower value average is  $\mu_2$ .
3. A mean of these two averages is calculated as a new threshold to re-partition the image.
4. Repeat steps 2 and 3 until the new threshold is the same value as the old threshold.
5. Using  $\mu_1$  as threshold number one, values higher than the threshold are classified into the first image which includes high intensity objects, e.g., a plastic land mines in the land mine detection application. Using  $\mu_2$  as threshold number two, values lower than the threshold are classified into the second image which includes low intensity objects, e.g., metallic land mines. The rest of the image is classified into the third image which is the background.

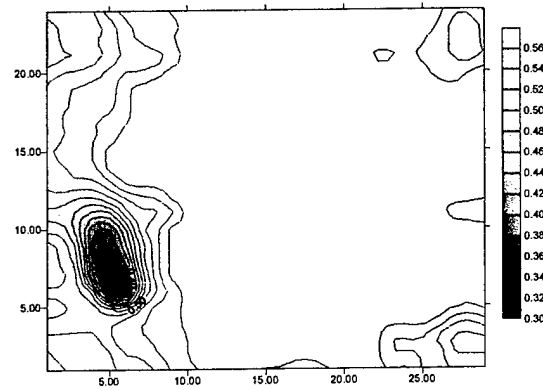
In Figure 35a, an LMR uncollimated detector image of a steel bolt and plastic surrogate mine is presented. Applying the modified iterative threshold selection algorithm, three images are obtained and the segmented images of object with higher intensity and object with lower intensity than the background are presented in Figure 35b and 35c. The high intensity object, the plastic surrogate mine, is partitioned into the first image; the low intensity object, the steel bolt, is partitioned into the second image.



a



b



c

Figure 35. Uncollimated detector image and segmented images of a 15 cm diameter plastic surrogated mine buried 2.5 cm deep with a steel bolt laid on soil surface. a) Original uncollimated detector image; b) Segmented high intensity object image; c) Segmented low intensity object image.

## Image Calculation

### Surface Feature Removal

From each LMR image scan, there are three images of the scanned area: uncollimated detector image, front collimated detector image and rear collimated detector image. Because of the LMR detector array configuration, these images have strong correlations between them.<sup>19</sup>

$$N(x,y) = (P_c(x,y) - \text{Min}_c) / (\text{Max}_c - \text{Min}_c) * 255 - (P_u(x,y) - \text{Min}_u) / (\text{Max}_u - \text{Min}_u) * 255$$

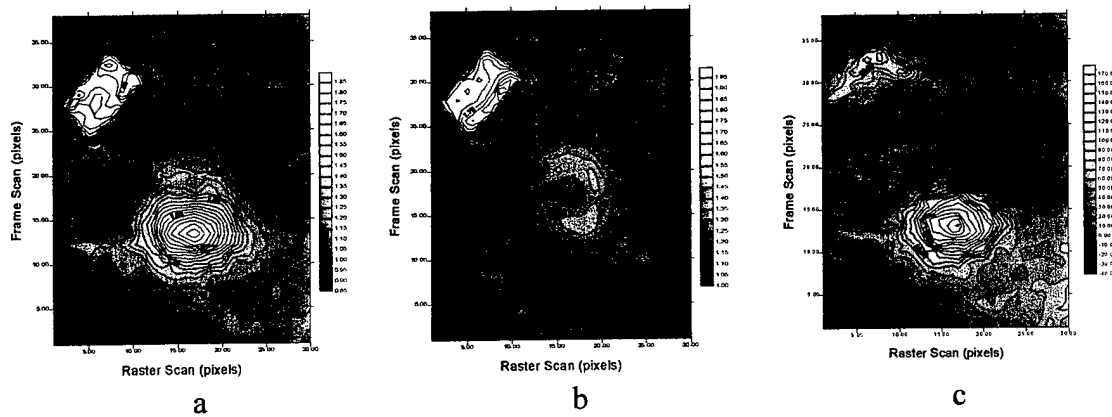


Figure 36. Surface features removal illustration. In the experiment, a 15 cm diameter plastic surrogate mine buried 2.5 cm deep and a 12.5 cm by 8.8 cm by 3.8 cm wood block laid on soil surface. a) Collimated detector image; b) Uncollimated detector image; c) Surface feature removed image.

The uncollimated detector image has primarily surface and near-surface features and the collimated detector images have both surface features and subsurface features. Therefore, surface feature removal can be accomplished by manipulating the collimated and uncollimated images. For example, in Figure 36, there is one plastic surrogate mine buried 2.5 cm deep and a surface laid wood block. Using image subtraction, the surface laid wood block is removed in the resulting image.



In Figure 37, there is a negative soil surface slope of 2.5 cm per 30.5 cm of travel in the frame scan direction. The intensity responses of the slope in the collimated and uncollimated detector images are opposite. This slope can be minimized by image addition. If a mine buried in an area with a surface slope, the previous discussed image segmentation algorithms may not work properly, part of the high intensity area of the soil surface may be classified as a part of mine. However after the elimination of the slope in the LMR images, the image segmentation algorithms can perform as desired.

$$N(x,y) = (P_u(x,y) - \text{Min}_u) / (\text{Max}_u - \text{Min}_u) * 255 + (P_c(x,y) - \text{Min}_c) / (\text{Max}_c - \text{Min}_c) * 255$$

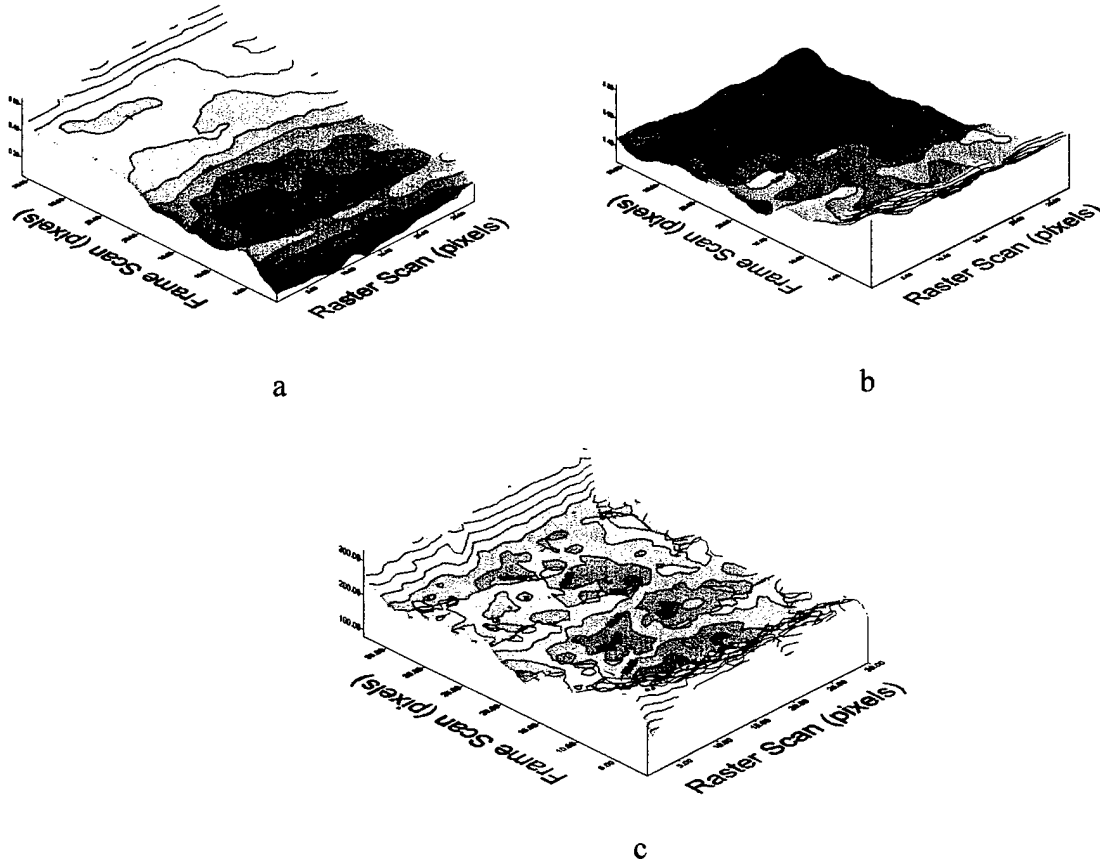


Figure 37. LMR images of soil with slope surface. a) Collimated image; b) Uncollimated image; c) Addition image.

Because of the LMR detector design and the different photon interaction cross sections of different objects, the responses of the same object can be different in the uncollimated and collimated detectors. In the land mine detection application, for plastic mines, the responses in all detector images are higher intensity than the responses of the soil. In contrast, metallic mines have lower intensities in all detector images. For potholes, the response in uncollimated detector images is an intensity decrease while in collimated detector images there is an intensity increase (see Figure 38). Therefore, a correlation between uncollimated detector images and collimated detector images can be used to minimize the false positives in land mine detection.

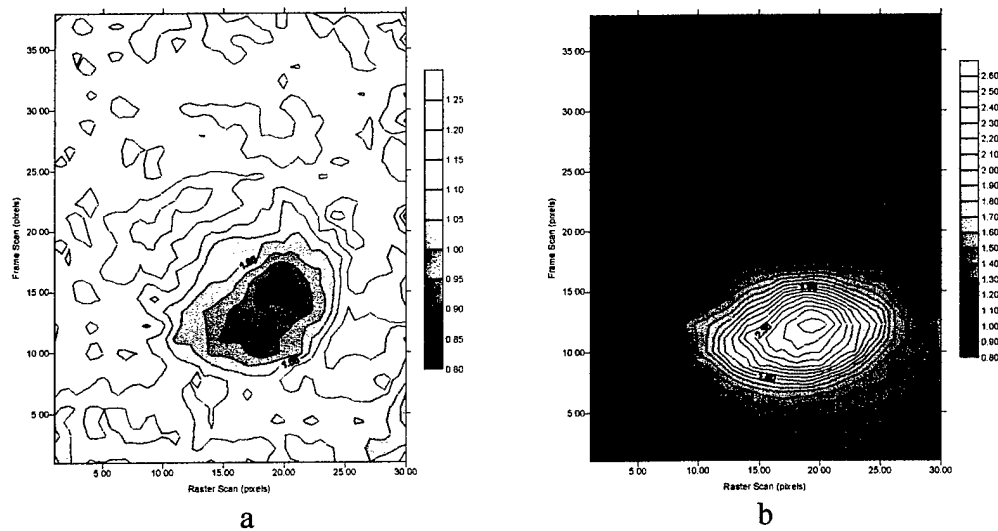


Figure 38. LMR images of a pothole. a) Uncollimated detector image; b) Collimated detector image.

### Subsurface Object Location and Depth Estimation

After image filtering and image correlation, both random noises and surface features are removed. Image segmentation partitions an image into several individual

sub-images that each contain one object. In each sub-image, object and background are relatively well-defined and can be further processed for object information extraction and pattern recognition. Subsurface object location and depth can be estimated, since the object depth is related to the degree of lateral migration shifting between front and rear collimated detector images. As an application example, a total of twelve real land mine LMR collimated detector images are used to develop algorithms to estimate land mine locations and their depth-of-burials. These collimated detector image data are presented in Table 3. In these real mine image data, one of them (TM-62P3, 2 inch burial) may have been corrupted electronically during the data acquisition, and because of limited access of these real mines, reexamination of this mines has not been done.

Using the above data, land mine location and depth-of-burial estimation algorithms are developed.

Algorithm 1: The coordinates of the maximum intensity pixels in the segmented front and rear collimated detector images are used to calculate lateral migration shifting and then calculate the center location of the land mine.

Algorithm 2: The geometric center of the segmented front and rear collimated detector images are used to calculate lateral migration shifting and then calculate the center location of the landmine.

Algorithm 3: The coordinate of the raster scan direction is that of the maximum image intensity pixel. The coordinate of the frame scan direction is obtained as that of the pixel of the intensity moments center along the column of the maximum intensity pixel in the front and rear collimated detector images. These coordinates are used to calculate lateral migration shifting and then calculate the locations of the land mines.

Algorithm 4: The coordinate of the raster scan direction is that of the geometric center pixel. The coordinate of the frame scan direction is obtained as pixel location of the average intensity moments center along the column of the maximum intensity pixel and its two adjacent columns in the front and rear collimated detector images. These coordinates are used to calculate lateral migration shifting and then calculate the locations of the land mines.

Table 3. The ratio of maximum to minimum intensity of uncollimated detector and collimated detector response for 12 real land mines.

Mine	Type	Dimensions (cm)	Uncollimated Detector Response Ratio		Collimated Detector Response Ratio		Depth-of-burial (cm)
			Front	Rear	Front	Rear	
M19	AT	33.3x33.3	1.20	1.19	3.83	3.50	2.5
			1.06	1.06	1.71	1.47	5.0
PTMI-BA3	AT	D=32.8	1.30	1.30	5.00	4.67	2.5
			1.07	1.08	1.91	1.83	5.0
TM-62P2	AT	D=30.7	1.33	1.34	2.33	2.36	2.5
			1.25	1.32	1.72	1.78	5.0
TM-62P3	AT	D=30.7	1.94	1.76	1.56	1.64	2.5
			1.71	1.71	1.5	1.79	5.0
TYPE 72	AT	D=26.9	1.09	1.09	2.60	2.27	2.5
			1.08	1.08	1.54	1.50	5.0
VS-2.2	AT	D=24.1	1.07	1.06	2.40	2.09	2.5
			1.06	1.06	1.48	1.45	5.0
TMA-4	AT	D=28.4	1.24	1.26	1.79	1.77	2.5
			1.08	1.08	1.47	1.38	5.0
TMA-5	AT	31x27.4	1.22	1.20	5.50	5.25	2.5
			1.07	1.07	1.76	1.60	5.0
VS-1.6	AT	D=22.1	1.68	1.71	4.75	5.00	2.5
			1.09	1.08	1.56	1.58	5.0
VS-MK2	AP	D=8.9	1.58	1.56	2.00	2.11	SURFACE
			1.19	1.18	1.37	1.35	FLUSH
VS-50	AP	D=8.9	2.05	2.16	2.44	2.44	SURFACE
			1.79	1.89	1.61	1.69	FLUSH
TS/50	AP	D=8.9	1.60	1.79	3.43	3.00	SURFACE
			1.24	1.30	1.40	1.37	FLUSH

AT = Antitank    AP = Antipersonnel

Table 4. Land mine center location and lateral migration shifting estimation obtained through four estimation algorithms. h, algorithm 1; p, algorithm 2; w1, algorithm 3; w, algorithm 4.

Mine Name	X,Y	X <sub>h</sub> ,Y <sub>h</sub>	L <sub>h</sub>	X <sub>p</sub> ,Y <sub>p</sub>	L <sub>p</sub>	X <sub>w1</sub> ,Y <sub>w1</sub>	L <sub>w1</sub>	X <sub>w</sub> ,Y <sub>w</sub>	L <sub>w</sub>
M-19 (1)	13,13	15,13	5	15,13	4.5	15,14	6	15,14	5.7
(2)	13,13	14,12	7	14,12	5	14,13	6	14,13	6
PTMi-BaIII (1)	13,13	13,13	5	13,13	5	13,14	5	13,14	4.7
(2)	13,13	14,13	6	13,13	5.5	14,13	5	13,13	5
TM-62P2 (1)	13,13	13,13	4	13,13	4.5	13,14	4	13,14	4.3
(2)	13,13	14,7	10	13,13	0	14,11	11	13,11	11.3
TM-62P3 (1)	13,13	17,12	5	14,11	0.5	17,14	4	14,13	5
(2)	13,13	19,6	7	13,12	2.5	19,11	11	13,11	0
TYPE72 (1)	14,12	14,12	5	13,12	5.5	14,13	5	13,13	5
(2)	14,12	13,12	5	14,13	6.5	13,13	6	14,13	6
VS-2.2 (1)	12,11	11,11	5	11,11	4.5	11,12	5	11,12	5
(2)	11,11	11,12	6	12,12	5.5	11,13	6	12,13	5.7
TMA-4 (1)	12,12	12,12	6	12,12	3.5	12,13	4	12,13	4
(2)	12,12	15,10	3	13,10	1.5	15,11	5	13,12	4.3
TMA-5 (1)	13,13	13,13	8	12,13	5	13,14	6	12,14	6
(2)	13,13	11,13	8	12,13	6	11,14	7	12,14	6.3
VS-1.6 (1)	12,11	11,11	5	11,11	4.5	11,11	5	11,11	5
(2)	12,11	11,11	5	12,11	6.5	11,11	5	12,11	5
VS-MK2 (s)	8,8	8,7	3	7,7	1	8,8	1	7,8	1.7
(f)	8,8	9,7	5	8,8	6	9,9	6	8,9	6
VS-50 (s)	8,8	9,8	2	8,8	0.5	9,9	2	8,9	2
(f)	5,5	6,5	3	6,5	3.5	6,5	3	6,6	3.3
TS/50 (s)	5,5	5,5	1	5,5	0	5,6	0	5,6	0.3
(f)	8,8	8,9	4	7,9	4.5	8,10	4	7,10	4.7

(1) 1 inch depth-of-burial      (2) 2 inch depth-of-burial  
(s) surface laid                      (f) flush buried

The results from these algorithms and comparisons with the true land mine center locations are presented in Table 4. Comparing these results, algorithm 2 and algorithm 4 perform better than the other two algorithms. Their predictions of the center locations of these land mines are very similar to the true locations and majority of the data show there is a relationship between lateral migration shifting length and the depth-of-burial (correlation coefficients between levels of lateral migration shifting and depth-of-burials for the four algorithms are 0.9875, 0.7626, 0.7794 and 0.9882). However, the amount of shifting between different land mines for a given depth-of-burial is different, which

means that lateral migration shifting distance alone can not be used to estimated the depth-of-burials of land mines. The type of mine has to be taken into account (as does the type of soil). Division of the lateral migration shifting distance by its corresponding collimated detector image mine-to-soil ratio creates a feature that can be used to estimate depth-of-burial of a land mine. This is presented in Table 5.

Table 5. Real mine data and their depth-of-burial estimation classifier.

Mine	Depth-of-burial (cm)	$L_p$	$L_w$	Collimated Detector Average Response Ratio R	$L_p/R$	$L_w/R$
M19	2.5	4.5	5.7	3.67	1.23	1.55
	5.0	5	6	1.59	3.14	3.77
PTMI-BA3	2.5	5	4.7	4.84	1.03	0.97
	5.0	5.5	5	1.87	2.94	2.67
TM-62P2	2.5	4.5	4.3	2.35	1.91	1.83
	5.0	0	11.3	1.75	0	6.46
TM-62P3	2.5	0.5	5	1.60	0.31	3.13
	5.0	2.5	0	1.65	1.52	0.00
TYPE 72	2.5	5.5	5	2.44	2.25	2.05
	5.0	6.5	6	1.52	4.28	3.95
VS-2.2	2.5	4.5	5	2.25	2.00	2.22
	5.0	5.5	5.7	1.47	3.74	3.88
TMA-4	2.5	3.5	4	1.78	1.97	2.25
	5.0	1.5	4.3	1.43	1.05	3.01
TMA-5	2.5	5	6	5.38	0.93	1.12
	5.0	6	6.3	1.68	3.57	3.75
VS-1.6	2.5	4.5	5	4.88	0.92	1.02
	5.0	6.5	5	1.57	4.14	3.18
VS-MK2	SURFACE	1	1.7	2.06	0.49	0.83
	FLUSH	6	6	1.36	4.41	4.41
VS-50	SURFACE	0.5	2	2.44	0.20	0.82
	FLUSH	3.5	3.3	1.65	2.12	2.00
TS/50	SURFACE	0	0.3	3.22	0	0.09
	FLUSH	4.5	4.7	1.39	3.24	3.38

In the table, for algorithm 2, the majority of land mines buried at 2.5 cm deep in soil have division of lateral migration shifting and collimated detector mine-to-soil ratio ranging between approximately 0.2 and 2.4 (9 out of 9), and the majority of land mines

buried at 5.0 cm deep in soil have the division above 2.6 (6 out of 9). For algorithm 4, the majority of land mines buried at 2.5 cm deep in soil have division of lateral migration shifting and collimated detector mine-to-soil ratio ranging between approximately 0.9 and 2.25 (8 out of 9), and the majority of land mines buried at 5.0 cm deep in soil have the division above 2.6 (8 out of 9, 8 out of 8 if TM-62P3 5 cm burial does not count). If this pattern presents in more real mine data, land mine depth-of-burials can be estimated by using this product as a classifier.

### Object Recognition

With certain objects presented in the acquired LMR images, object recognition algorithms are necessary to classify or identify the objects. Template matching is one of these essential approaches. A preliminary examination is presented because of limited real mine data. Template matching requires the original object image data to be stored in a computer in a certain format and that each acquired image is checked by image template matching. An image with a template matching output value above a certain threshold value is expected to have the object in it. One possible template matching function is given by

$$M[I, J] = C_{fg}[I, J] / \{ \sum_{K=1}^m \sum_{L=1}^n F^2[I+K, J+L] \}^{1/2}$$

where  $C_{fg} = \sum_{K=1}^m \sum_{L=1}^n T[K, L] * F[I+K, J+L]$  is a cross-correlation function

$T[I, J]$  represents the object template,  $F[I, J]$  is the acquired image

Calculations of  $M$  yield maximum values in the acquired image. By applying a certain threshold value for the local maxima, an object match is found.

In the LMR system, the uncollimated detector has the ability to detect land mines buried at a maximum of 3 cm or 4 cm and its image shows the geometric shape of the

mine and its air volume. This image can significantly help land mine detection personnel to distinguish a land mine from other non-mine objects and probably identify what type of mine it is. When a land mine is buried deeper than 3 cm but less than 10 cm, uncollimated detector images are overwhelmed by soil surface variation and random noises, but the collimated detectors can still detect the land mine. Therefore, in the land mine recognition process, uncollimated detector images are examined first; if there is an air volume combined with a geometric-shaped object, a land mine is recognized. If there is no land mine recognized in the uncollimated detector image, collimated detector images are examined for land mine recognition.

Since there are limited real land mine data, a database of templates of various land mines buried at different depth-of-burial can not be setup. In order to experiment with the template matching technique, An LMR image of one of the real mines is used as a template to apply to similar shaped and sized land mine LMR images. The image template is from the collimated detector image of the VS-1.6 and the test image is from the VS-2.2 antitank mine collimated detector image. Applying the above template matching function, one local maximum value is present in the acquired image and its location is at the object intensity peak location in the image.

LMR image template matching needs a great number of real mine data to generate image templates for all kinds of mines. When the land mine LMR image template database is built up, an empirical threshold for the template matching function can be obtained and a land mines can be distinguished from non-mine objects through image template matching.



## CHAPTER 6 MOBILE FAST-SCAN LMR MODULE

### **General Mechanical Design and System Composition**

The mobile fast-scan LMR module has been fabricated and will be tested in an outdoor land mine field laid by the US Army. As illustrated in Figures 39, 40 and 41, this module includes an x-ray generator, an x-ray beam rotating collimator, detector panels, an aluminum mounting platform, a Unistrut steel frame structure and motion positioning and control components. An off-the-shelf industrial x-ray generator is used to provide the x-ray source. The x-ray beam rotating collimator is mounted on the x-ray generator to facilitate image raster scan. The x-ray generator is mounted on the aluminum platform. Plastic scintillator detectors are mounted under the aluminum platform to register the backscattered x-ray field. The whole platform rides on two steel rails whose ends are mounted on a steel frame which provides a rigid and compact structure. The rotating collimator is driven by a servo motor through a pulley belt and the platform is driven by another servo motor through a lead screw. The module is carried by a fork lift when employed in the mine field scan. The module is designed to work as a confirmation sensor for other fast scan devices because of its relatively fine image resolution. If necessary, it can work as an independent land mine detection device discontinuously examining adjacent patches of the land mine field.

### X-ray Generator

Since the module will be used in land mine detection, a compact, robust, constant potential and full duty cycle x-ray generator is needed. The module will need to work in

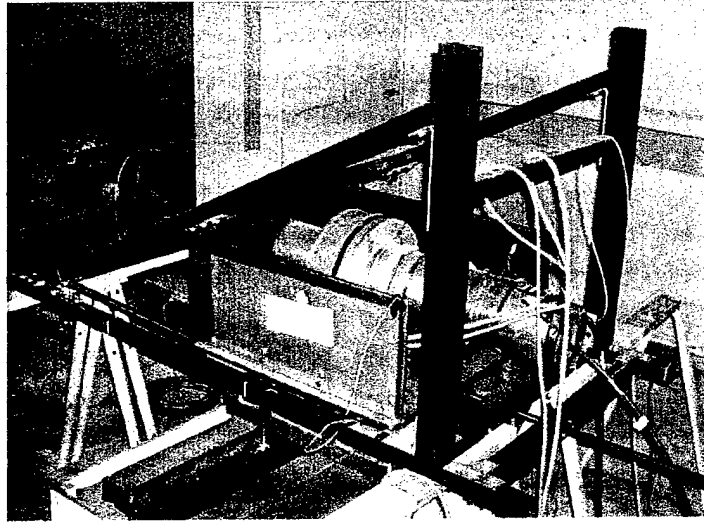


Figure 39. Side view of LMR mobile fast-scan LMR module.

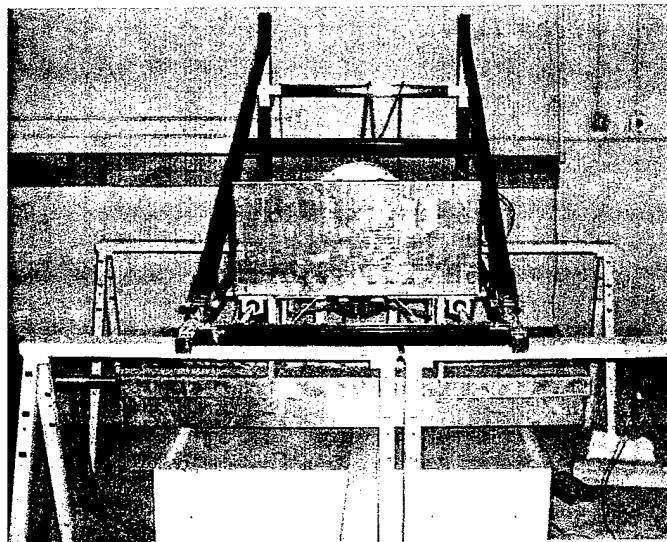


Figure 40. Front view of LMR mobile fast-scan LMR module.

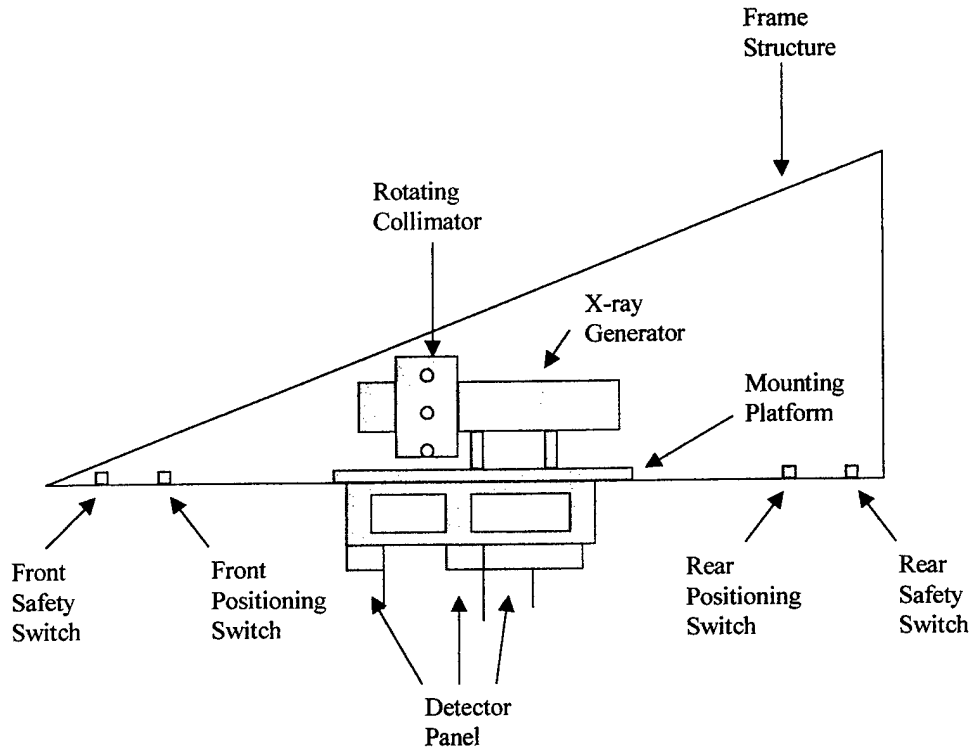


Figure 41. Drawing of the LMR mobile land mine detection module.

various environments to detect land mines. The generator is moved with the module and is moved within the module, so compactness and robustness of the x-ray generator are necessities for a flexible and long lasting LMR module. During each image scan, the x-ray generator tube head is set at a certain voltage and current and they should not vary significantly; otherwise, artificial patterns will appear in acquired images because of non-uniform illumination of different pixels. A constant potential x-ray generator can maintain almost constant voltage on the x-ray tube head and has very little voltage ripple. In a land mine detection mission for the Army, a path needs to be cleared in a certain amount of time. Only a full duty cycle x-ray generator can accomplish the job. Any non-

full duty cycle x-ray generator needs time to cool off the anode. Given all the above requirements of the x-ray generator, the LORAD LPX-160 is selected as the x-ray generator for the mobile LMR module. Its specifications are listed in Table 6.

Table 6. LORAD LPX-160 x-ray generator specifications

Tube Head (Physical Specifications)	7.25 inch diameter 28 inch length	30 pounds
Tube Head (Electronical Specifications)	10 - 160 kV (1 kV increment)	0.1 – 5.0 mA (0.1 mA increment)
Control Unit	12" x 18" x 12"	35 pounds

### **X-ray Beam Rotating Collimator**

Within this mobile LMR module, the rotating collimator is a key component to realize a fast image scan. As explained in Chapter 3, the rotating collimator has a stator and a rotor. The rotor slides on the stator and the stator is mounted on two aluminum end pieces which each connect to a brass ring. The brass rings are mounted on the x-ray generator body by set screws (Figure 42). On the stator, there is a 1 cm wide slot which subtends 38 degrees to the center of the stator. This slot, combined with lead shielding inside the stator, generates an x-ray fan beam by confining a cone beam from the x-ray generator output window (Figure 43). On the rotor, ten equally separated holes align on one section circle (Figure 44 and Figure 45). A rectangular lead strip whose circumference is the same as that of the inside of the rotor has ten equally separated slits corresponding to the hole positions of the rotor. This lead strip is glued on the inside of the rotor to define a suitable x-ray illumination spot on the scanned surface. To minimize the friction between the stator and the rotor, three Teflon strips are glued on the inside edges and center of the rotor. On the outside of the rotor, a series of pulley belt grooves

are machined which accommodate a pulley belt to drive the rotating rotor (Figure 46). Beside each hole of the rotor and aligned with each slit, a magnet is glued on as a trigger to start each raster scan. When the LMR module does image acquisition, the stator collimates x-ray output into a fan beam; the rotor rotates the slits to sample the fan beam continuously. Therefore, there is no dead time during image acquisition. This yields faster image scans than that of the previous LMR systems.

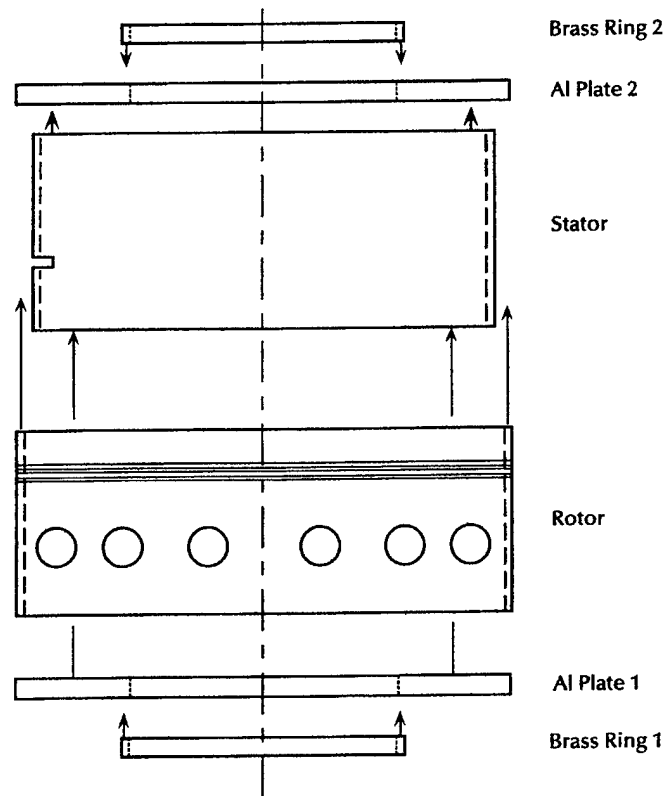


Figure 42. Rotating collimator assembly components.

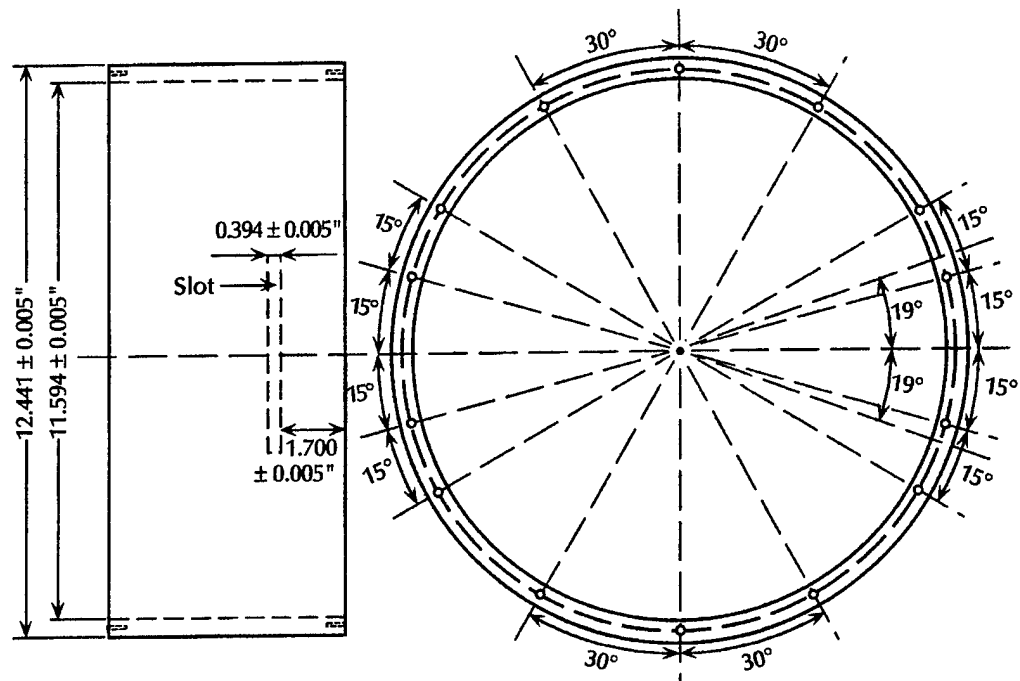


Figure 43. Rotating collimator stator.

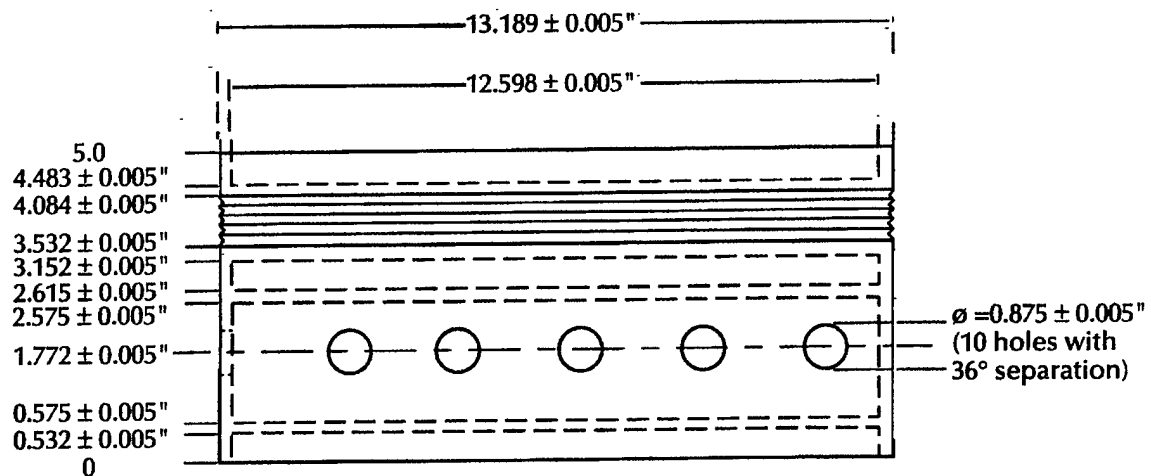


Figure 44. Rotating collimator rotor.

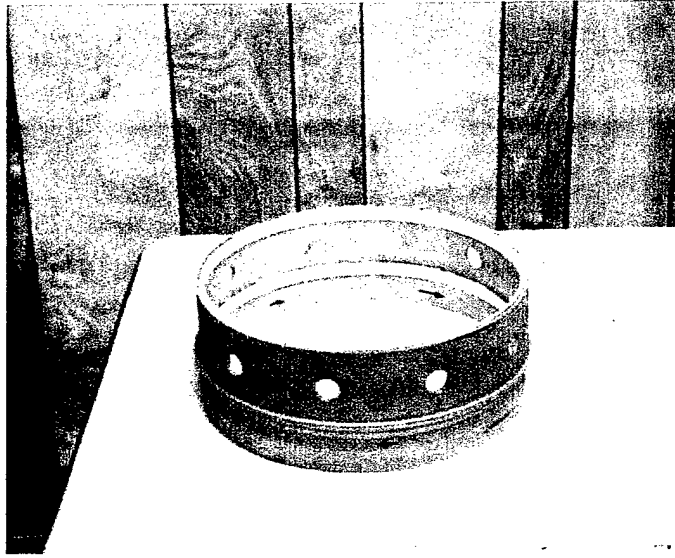
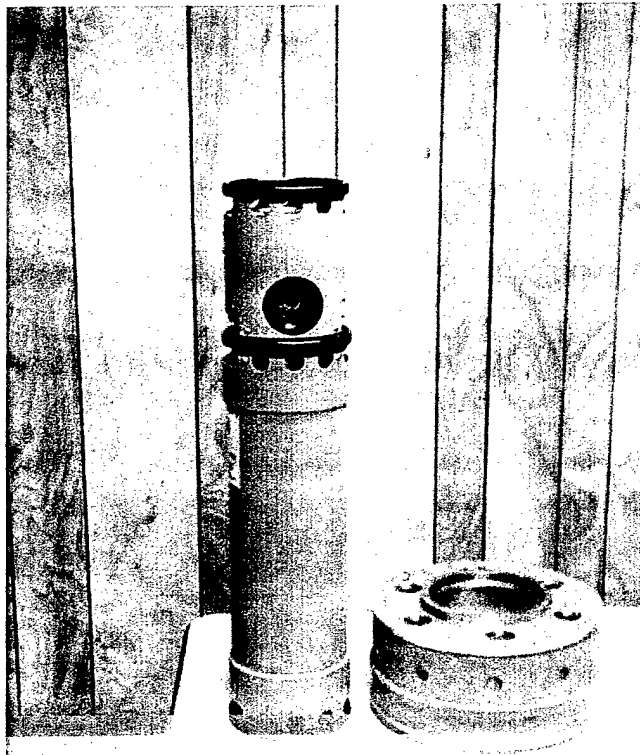


Figure 45. X-ray beam rotating collimator rotor.



## **Detector Position, Material and Dimension**

### **Detector Material: Scintillator vs Sodium Iodine**

In x-ray photon detection, popular detectors are the plastic scintillator detector and the sodium iodide detector. Of these two kinds of detectors, the plastic scintillator is organic and the sodium iodide is an inorganic crystal. They have different scintillation light output, different mean-free-path for x-ray photons, different weight per unit volume, different durability and availability.

For a given detector thickness, different mean-free-paths in the two kinds of detectors for the same x-ray photon spectrum will result in different photon energy deposition. Furthermore, because the terrain of a land mine field might be quite bumpy which leads to severe concussion and vibration of the system, durable detector material is a key consideration for a successful land mine detection system. The detector material's specific gravity is also a very important factor because the detectors have dimensions of 140 cm in length and 5 to 20 cm in width.<sup>20</sup> A low density of detector material will significantly lighten the system's weight. Availability of such large area detectors is also a significant factor when choosing the detector material. The mean-free-paths of a typical LMR backscatter x-ray photon spectrum in both plastic scintillators and sodium iodide have been acquired through MCNP simulations and all the major comparisons of the two detector materials are shown in Table 7.

In the comparisons of Table 7 and 8, the sodium iodide detector has the advantages of high energy deposition of x-ray photons and high light output. This means that the sodium iodide detector has a higher signal strength than the plastic scintillator does. But there are two practical disadvantages of the sodium iodide detector in an LMR



module for land mine detection, availability and durability. The use of sodium iodide detectors involves a relatively high initial expense and requires frequent replacement as they get damaged. In contrast, the plastic scintillator can be easily manufactured in large pieces and works fine when it has small cracks inside. Furthermore, the energy deposition disadvantage of plastic scintillator to the sodium iodide is greatly reduced if the thickness of the detector is a few centimeters or more. Therefore, the LMR module uses the plastic scintillator as the detector material.

Table 7. Comparisons of plastic scintillator detector and sodium iodide detector.

	Plastic Scintillator	Sodium Iodide
Density (g/cm <sup>3</sup> )	1.032	3.67
Durability	Performance not greatly affected by cracks	Impaired performance with cracks
Availability(140x20x5 cm)	Easy	Not easy
Light output(relative scale)	1	3.5
Mean-free-path (cm) (typical LMR backscatter x-ray spectrum)	4.7—4.8	0.04—0.046

Table 8. Energy deposition ratio of sodium iodide detector to plastic scintillator at different thickness

Detector thickness(cm)	Energy deposition ratio (Sodium Iodide / Plastic Scintillator)
0.1	230
0.5	49
1.0	25
3.0	8.5
5.0	5.7

### Uncollimated Detector Positioning

In the usual setup of LMR system, the uncollimated detector is at the same height above the ground as the collimated detectors, as shown in Figure 1. A lower height for

the uncollimated detector can increase the solid angle subtended by the detector to the x-ray interaction volumes. This can be achieved if the bottom side of the uncollimated detector is positioned at the same level as the bottom edge of the longest lead collimator of the collimated detectors. This repositioning of uncollimated detector height does not affect the signal strength of the collimated detectors because of the unchanged x-ray backscattered field for the collimated detectors. MCNP simulations are carried out to examine this repositioning and the results of the height changes on the uncollimated detector are shown in Table 9.

Table 9. Signal strength ratios of uncollimated detector at different heights.

Detector height (cm)	21.7	26	30	35
Signal strength (relative scale)	1.5	1.3	1.15	1

By lowering the uncollimated detectors to the above lowest height from the height of the collimated detector (30.5 cm), the signal strength of the uncollimated detector can be increased by about 30 percent; this improvement is significant and nothing has been compromised. In the mobile LMR module, for mechanical design simplicity, lowering the uncollimated detector is not adopted.

### **Detector Electronics and Electromagnetic Interference Shielding**

The uncollimated and collimated detectors register some of the backscattered x-ray photons and convert them into visible photons in the plastic scintillators. To acquire these photons and convert them into detector signals, photomultiplier tubes are employed. The photo-multipliers are HAMAMATSU R6095 which are designed to work in the

pulse mode for scintillator counting (Table 10). The project electrical engineer, Dan Ekdahl, modified them to work in current mode in this application (Figure 47). In Figure 47, a high voltage bias is applied to the photomultiplier tube to amplify the number of photoelectrons (Figure 48). A preamplifier is employed to convert the low-level, high-impedance current output of a photomultiplier tube into low-impedance voltage output (Figure 49). In the project, Dan Ekdahl designed and manufactured a miniature preamplifier circuit and a miniature high voltage bias circuit to provide a very compact detector electronic system. The preamplified signals from the photomultiplier tubes at both ends of the detector are input to a summing amplifier which sums and amplifies the detector signals and inputs them to the data acquisition system (Figure 50). In these circuits, miniature voltage regulators (Figure 51) and dual charge pumps are employed (Figure 52).

Table 10. Characteristics of R6095 photomultiplier tube.

Remarks	Spectral Response		Photo-cathode Material	Window Material	Anode to Cathode Voltage (Vdc)	Average Anode Current (mA)	Typical Gain
	Range (nm)	Peak Wavelength (nm)					
For visible range and scintillation counting	300-650	420	Bialkali	Borosilicate	1500	0.1	$2.1 \times 10^6$

During the system measurements, it was found that the x-ray generator emits a relatively strong electromagnetic wave at 50 kHz and at higher harmonics, and this interferes with the signal amplified by preamplifiers of the detectors. To eliminate this

electromagnetic interference, a brass housing assembly for each preamplifiers and high voltage bias circuits was fabricated for mounting on the end of the photo-multiplier tubes (Figure 53). The brass housing assembly includes the brass front sleeve, preamplifier and high voltage bias circuits house, and an end cap with connectors (Figure 54). The preamplifier circuit is mounted at the front end of the house (Figure 55a) and the high voltage bias is mounted at the back end of the house (Figure 55b). On the end cap, there are three connectors: one is a 12 V power input connector; one is a signal output connector; and the last one is an electronic ground connector.

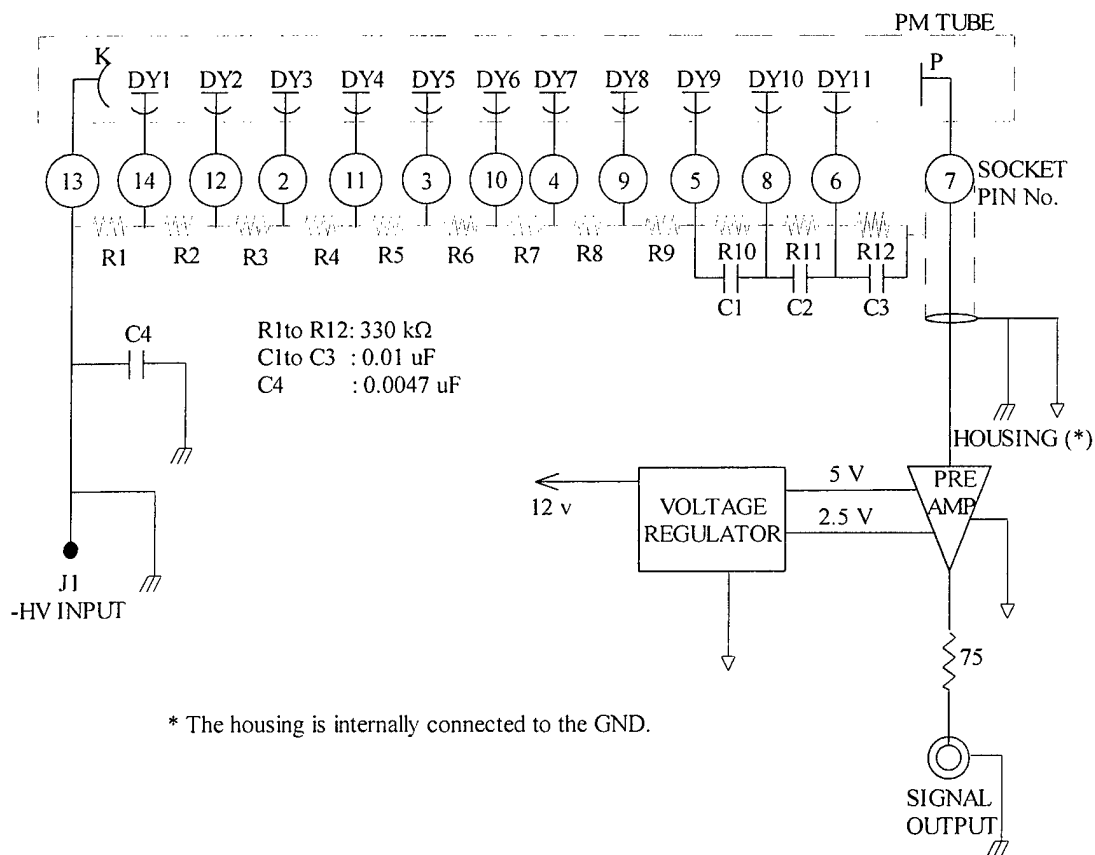


Figure 47. Circuit drawing of photomultiplier tube assembly.

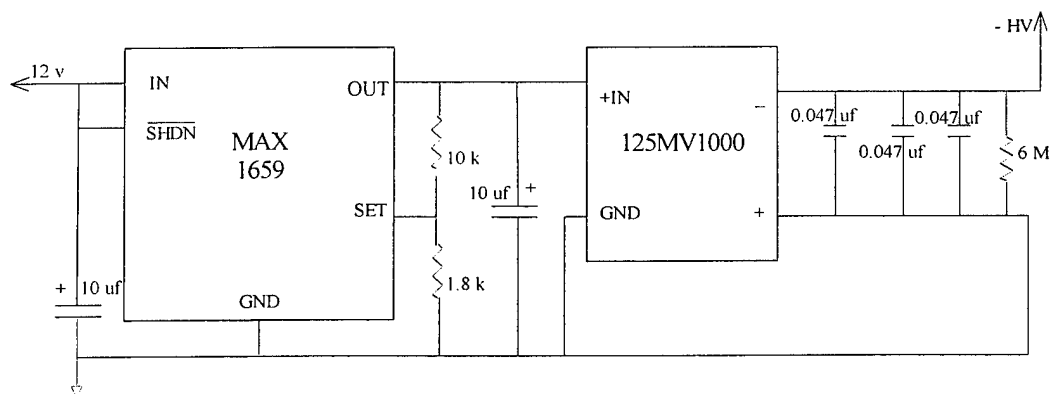


Figure 48. Circuit of high voltage bias to photomultiplier.

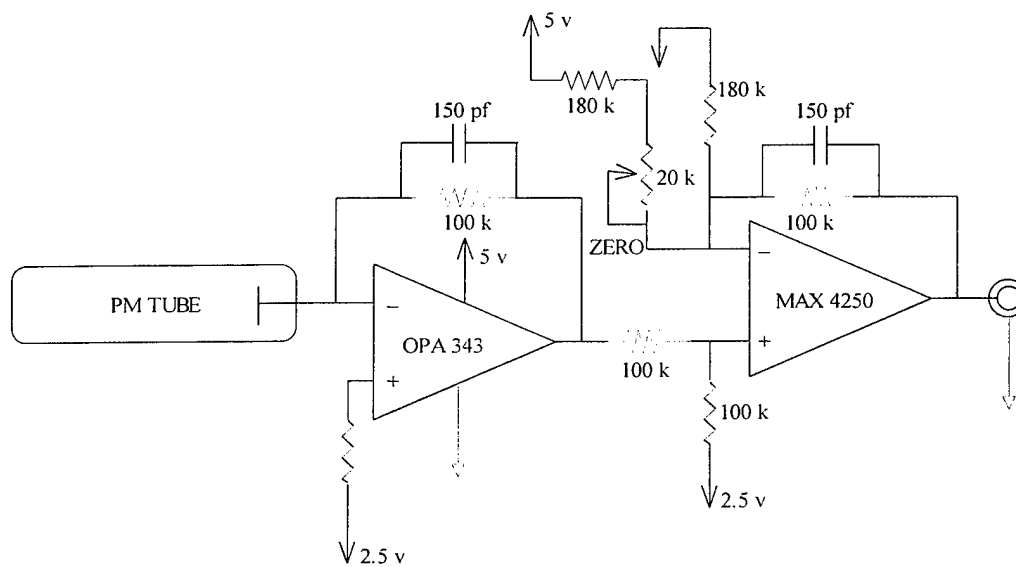


Figure 49. Circuit drawing of the preamplifier.

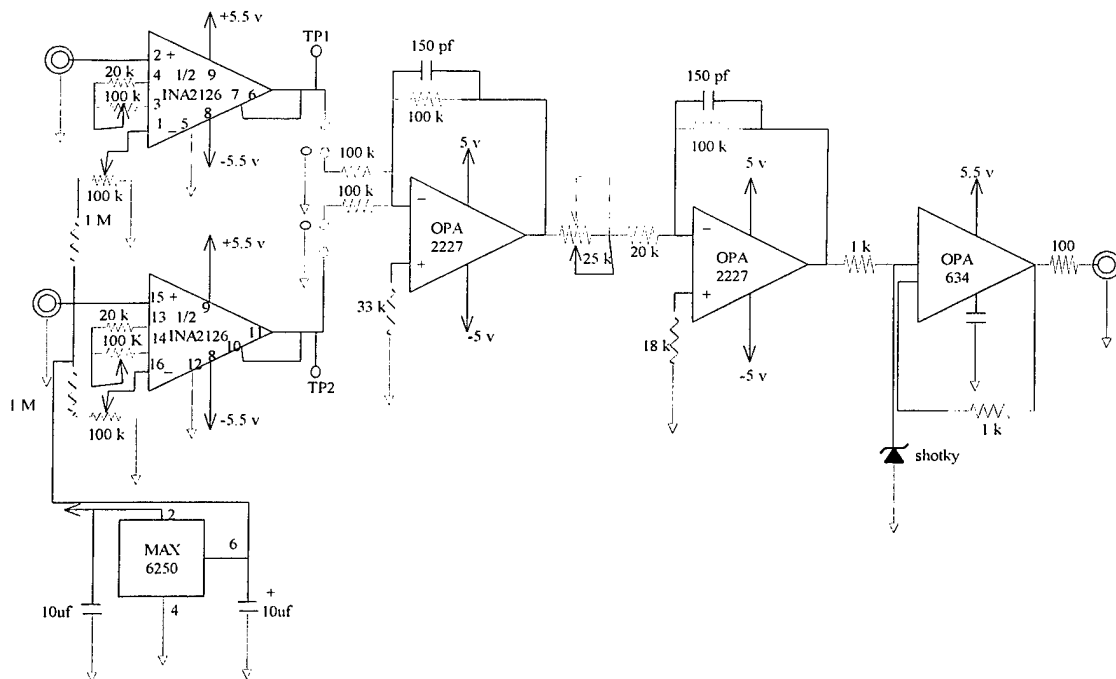


Figure 50. Circuit of summing amplifier.

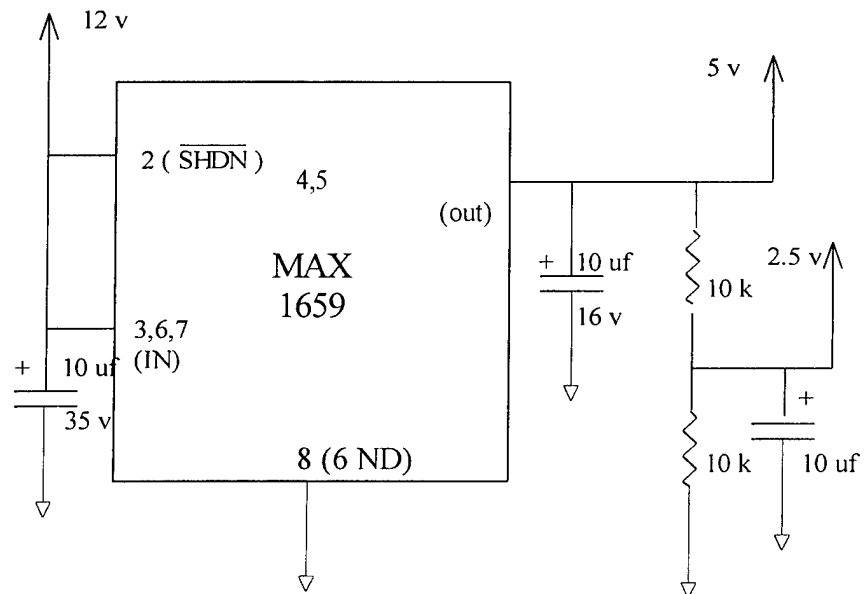


Figure 51. Circuit Drawing of the voltage regulator.

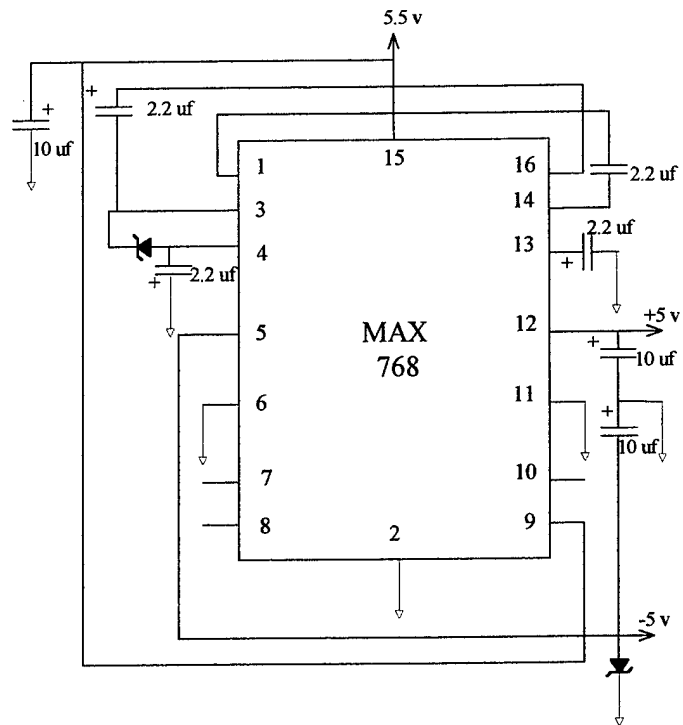


Figure 52. Circuit drawing of the dual charge pump.

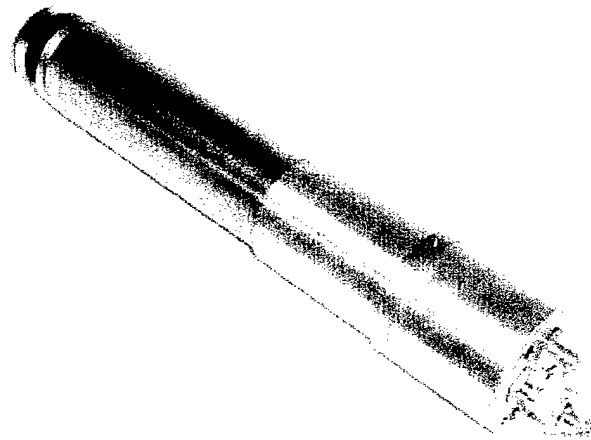


Figure 53. Assembly of photo-multiplier tube and brass housing of preamplifier and high voltage bias circuits.

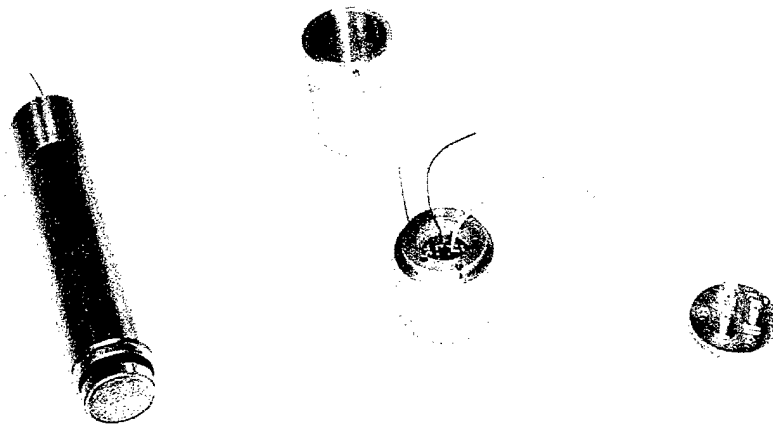


Figure 54. Photo-multiplier tube and brass housing components.

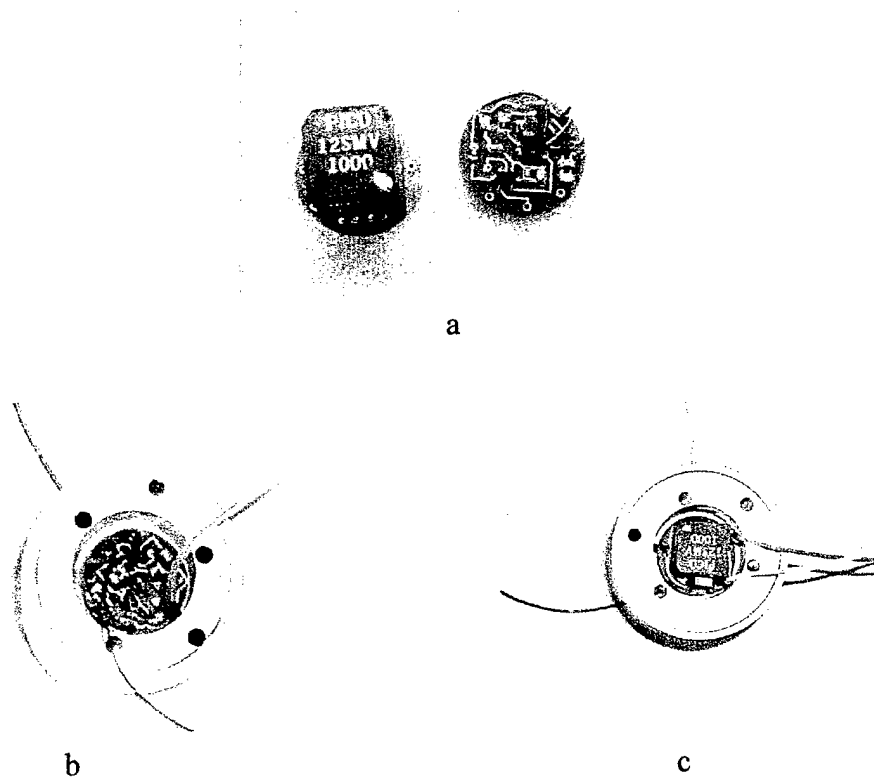


Figure 55. Photo-multiplier high voltage bias and preamplifier circuits and their locations in the brass housing. a) High voltage bias and preamplifier circuits; b) Preamplifier circuit in the front end of the brass housing; c) High voltage bias circuit in the rear end of the brass housing.



### Motion Control and Data Acquisition Synchronization

In the mobile LMR module, the image scan is accomplished by coordination between the rotating collimator speed and platform motion speed. The two components are driven by two servo-motors. Controllers for the two motors are daisy-chained together and one of them is connected to a computer RS232 serial port. A LABVIEW program is written to control the movement of the two motors through the serial port and to acquire image data through a data acquisition card which connects to the output of the x-ray detectors. A diagram of the system component connections is shown in Figure 56.

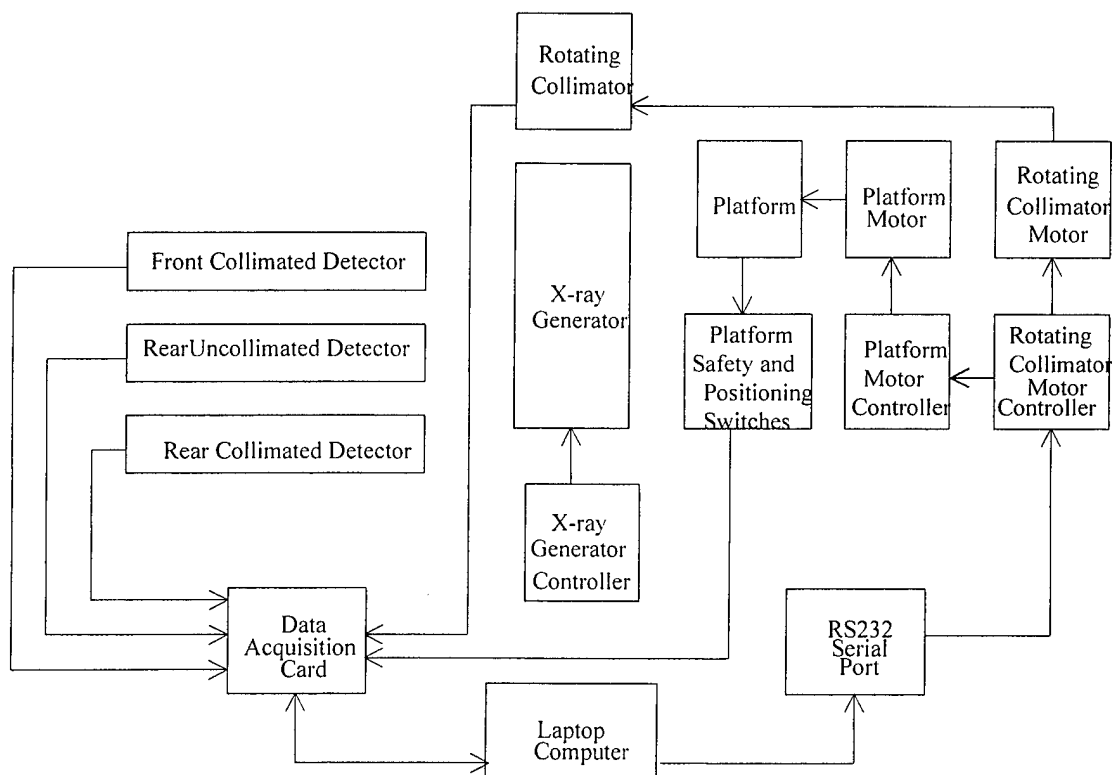


Figure 56. Diagram of LMR land mine detection assembly component connections.

In the LABVIEW program, motion control commands are sent to the controller of the rotating collimator motor to drive the rotating collimator at a certain speed. The speed of the rotating collimator is measured through a magnet sensor to acquire the period of magnetic impulses caused by the magnets on the rotating collimator. Based on this speed and the pixel size, the required platform motion speed is calculated and is sent to the controller of the platform motion motor. Then the platform carrying the x-ray generator and detector assembly is moved forward synchronously with the speed of rotating collimator. When each hole of the rotor sweeps through the fan beam defined by the stator, one raster scan of the image is accomplished. After a preset number of lines of raster scan, both motors stop moving and the resulting uncollimated and collimated detector images are presented on the computer screen. A moment later, a motion control command is issued to the platform motion motor to move the platform back to the starting position.

### **Platform Repositioning and Safety Switches**

With leadscrew motion methods, backlash is inevitable. Multiple direction changes of the platform motor could accumulate positioning error to a level such that normal image scanning cannot proceed. In land mine detection applications, multiple scans of many areas within a certain periods of time are very common. Therefore, a platform repositioning and safety mechanism is designed and implemented in the mobile LMR module.

Two safety switches are installed on the front and rear ends of a side bar of the frame to disable the platform motion motor in case the platform is in undesirable positions (Figure 41). These switches are contact switches. When the platform moves into

undesirable positions, one side of the platform presses a lever on the switch and the motor is disabled until the lever recovers its original position. Two positioning switches are mounted inside of the safety switches near the front and rear ends of a side bar of the frame. These two switches are the same type of contact switches as the safety switches and they work as two sensors. When the platform reaches these switches, physical contact causes an electronic impulse to be sent to the data acquisition card and the motion control program stops movement of the platform motor so the platform is at the right position for an image scan (Figure 41).

## CHAPTER 7

### SUMMARY AND CONCLUSIONS

In this dissertation, the fundamental physics of LMR have been analyzed and a new x-ray beam formation technique, using an x-ray beam rotating collimation/collimator, was proposed, analyzed, constructed and tested. The new x-ray beam formation technique significantly reduces the LMR image acquisition time and simplifies the LMR system. The physical effects and the imaging physics of the x-ray beam rotating collimator were thoroughly studied and corresponding image acquisition algorithms and image processing algorithms were developed and tested. Using this x-ray beam rotating collimator, a practical mobile LMR fast scan system was also developed and tested in one of the LMR applications, land mine detection.

LMR employs two types of detectors, uncollimated and collimated detectors, to detect the backscatter x-ray field. The uncollimated detector(s) mainly register once-collided photons which carry information from the examined surface and from about one half to one mean-free-path thick layer of subsurface. Collimated detector(s) predominantly detect multiple-collided photons which migrate through the scanned media and carry information from both the examined surface and from a two or three mean-free-path thick subsurface layer. Therefore, uncollimated detector images have well-defined surface features and some subsurface features; collimated detector images have significant subsurface features and a certain level of surface features. In the LMR image signatures, lateral migration shifting exists for subsurface features in the collimated detector images; a shadowing effect for objects protruding above the scanned

surface is present in both collimated and uncollimated detector images; and air volumes within examined objects greatly enhance image contrast and help in distinguishing different objects.

In contrast to the x-ray beam formation technologies of previous LMR systems, a new x-ray beam formation technique, x-ray beam rotating collimation/collimator, was thoroughly analyzed for its physical effects and imaging physics. The rotating collimator has a stator and a rotor. The stator with a slot on a section circle collimates the x-ray generator output into a fan beam, and the rotor, with equally separated slits on a same section circle plane, continuously samples the fan beam to implement image raster scans. The rotating collimator causes the x-ray beam to have a varying angular incidence on the scanned surface which introduces a number of physical effects that are not present when the x-ray beam has fixed perpendicular incidence on the scanned surface; however the LMR signatures still exist in the images of both cases. Image acquisition algorithms and image processing algorithms are developed to minimize the unwanted effects on the LMR images caused by the x-ray beam varying angular incidence or x-ray illumination spot movement during image data acquisition. These effects include:

1. Non-uniform speed of the x-ray illumination spot on the scanned surface.

When the rotating collimator rotates at a constant speed, the speed of the x-ray illumination spot on the scanned surface varies as the x-ray incidence angle relative to perpendicular incidence varies. The speed of the x-ray illumination spot on the scanned surface is a function of the x-ray beam incidence angle. The non-uniform speed of the x-ray spot introduces non-uniform x-ray illumination for each image pixel.

2. Variation of x-ray illumination spot size. As the x-ray beam incidence angle changes, the size of the x-ray illumination spot on the scanned surface also changes. The length of the spot in the raster scan direction is elongated which leads to the spot covering more area than for the case of an x-ray beam with fixed perpendicular incidence. An image data acquisition algorithm is developed to ensure uniform x-ray illumination for each pixel. This algorithm corrects the combined effects of x-ray illumination spot size variation and its non-uniform speed on the scanned surface.
3. Definition of resolution. To get relatively good photon statistics, a certain x-ray illumination time is required for each pixel. During data acquisition, the x-ray spot on the scanned surface is continuously moving. So the length of the x-ray illuminated area in the raster scan direction during this period of time is always greater than that of the image frame scan direction. Different resolutions in two orthogonal directions of the LMR images are inevitable. A linear asymmetric weighting algorithm to weight-sum sample points for each pixel intensity is used to minimize the resolution difference.
4. Raster direction squeezing effect. In the MCNP simulation images, subsurface object images have greater intensity changes in the raster direction than in the frame scan direction. This is caused by vertical geometric projection differences of the x-ray beam interaction locations relative to the x-ray surface illumination locations. This effect is not observed in the measured LMR images because it is masked by the x-ray leakage field.

5. Compton interaction angular difference. When a uniform material is scanned in the MCNP computer simulations, pixels at greater x-ray incidence angles have a slightly higher intensity. The Compton interaction anisotropic angular distribution leads to this effect. In experimental LMR images, this effect can not be seen because it is masked by the x-ray leakage field.
6. Skewed x-ray illumination spot traces. This is caused by the synchronized motion between the x-ray generator and detector assembly and the rotating collimator. It is corrected by interpolation of image data to a rectangular grid.

LMR images from both the x-ray angular incidence and the perpendicular incidence cases have common LMR image signatures, and these signatures are used to develop LMR image processing and pattern recognition algorithms to improve the LMR image quality and extract information of scanned objects or surfaces. The acquired LMR images are first processed by image filter(s) to suppress image noises and retain image data fidelity. Then the filtered images are segmented into separated objects for further image processing and pattern recognition. Since the collimated detector images and the uncollimated detector images each have a certain level of surface features and subsurface features, image correlation processing is employed to eliminate unwanted surface features or identify certain objects. Based on the lateral migration shifting distance and the object-to-background signal ratio of the collimated detector images, subsurface object depth can be estimated. As an example, in the LMR land mine detection application, depth-of-burials of land mines are estimated. A template matching technique is used for land mine recognition. Since there are only a limited numbers of real LMR land mine

images available, the algorithms for land mine depth-of-burial estimation and template matching need to be further tested with more extensive real mine data.

A practical fast-scan LMR system with x-ray beam rotating collimator was designed, fabricated and tested. A 45 cm by 45 cm area can be scanned by this system within 30 seconds. The scan time of the rotating collimator system is two orders-of-magnitude faster than previous LMR systems with x-ray beam perpendicular incidence and the acquired LMR images have similar quality. This fast scan system is also mobile, so it can be used in various locations, thereby providing a great advantage in some of the LMR applications, e.g., land mine detection and material defect detection in large immobile equipment or structures.

Even though the developed LMR system demonstrates good object detection capability, the system can be improved to lower the x-ray leakage field and reduce system weight. First, a liquid cooled x-ray generator could be used, so that the rotating collimator can be made without air flow holes in the end pieces. This will reduce the x-ray leakage field. Secondly, steel cylinders can be used to make the rotating collimator, so that gears can be mounted on it to provide smooth rotation of the rotor without any slippage (the current system uses a pulley belt to drive a rotating collimator made from PVC tubes). Finally, the detector length can be reduced from 150 cm to about 90 cm with no significant impact on the acquired LMR images. This will reduce the weight of the current detectors by about one-third and also their associated lead shielding which is one-sixth of the total system weight.

When applying the mobile fast-scan LMR system in other applications, e.g., material defect detection,<sup>21</sup> the current x-ray beam rotating collimator LMR system needs



some modifications. In material defect detection, a smaller size of the x-ray illumination spot is required to detect small material defects, e.g., air bubbles in aluminum sheets. Therefore, the slit size on the rotor of the rotating collimator should be made smaller than 2 mm (as used by the current system).

Of all the LMR applications, the constant potential of the x-ray generator is very important, since it introduces minimum variation of the x-ray output. In the modern technology of the x-ray generator, constant potential is implemented by applying high frequency three phase voltage between the x-ray cathode and anode. Higher frequency of the voltage results in lower variation in x-ray output. Therefore, depending on the level of acceptable x-ray output variation in a certain application, x-ray generator selection can be guided by the applied voltage frequency to the x-ray tube.

APPENDIX A  
MATLAB CODES OF IMAGE PROCESSING AND PATTERN RECOGNITION

Skewcorrection.mat

```
% Skewed image
fidA=fopen('detect2_Surfer_unistrutbar.txt');
[a, countn]=fscanf(fidA, '%f', [3,inf]);
fclose(fidA);

% Skew correction
dim = length(a);
maxa = max(a');
mina = min(a');
M = maxa(1);
N = maxa(2);
minx =mina(3);
maxx = maxa(3);
c(M,N) = zeros;
delta = maxx-minx;

% Normalize the pixel intensity
for count=1:dim
    x=a(1,count);
    y=a(2,count);
    c(x,y) = a(3, count);
end

% Calculate the skewed node Y coordinate
d(M,N) = zeros;
dr(M,N) = zeros;
del = 1.0/M;
for countm=1:M
    for countn=1:N
        d(countm, countn) = countn + (countm -1)*del;
        dr(countm, countn) = countn;
    end
end

% Spline to find values on the node of the rectangular grid
e(M,N) = zeros;
e(1,:) = c(1,:);
```

```

for i = 2:M
    e(i,:) = spline(d(i,:),c(i,:),dr(i,:));
end

```

```

% Output image before skew correction and after
save skewUNCorrect.out c -ASCII
save skewCorrect.out e -ASCII

```

Processing.mat

```

clear
close all

```

```

% Open image file in surfer format (x,y,z)

```

```

fidA=fopen('c2051521.367');
[a, countn]=fscanf(fidA, '%f', [3,inf]);
fclose(fidA);

```

```

fidB=fopen('c1051521.367');
[b, countn]=fscanf(fidB, '%f', [3,inf]);
fclose(fidB);

```

```

% Apply image filters
[ca1, ca2, cam, caw] = filters(a);
[cb1, cb2, cbm, cbw] = filters(b);

```

```

% Segmentation of filtered images
[segobja, segbacka] = segmentation(cam);
[segobjb, segbackb] = segmentation(cbm);

```

```

% Calculation of lateral migration shifting and object center location
% Max intensity, Geometric center, Single column momentum averaging
[xc, yc, Lc, xp, yp, Lp, xw1, yw1, Lw1] = shifting(segobja, segobjb);

```

```

% Multiple column momentum averaging technique
[xw, yw, Lw] = shifting2(segobja, segobjb);

```

```

% Compensate for the loss by one of the center location from image filtering
xh = xc+1
yh = yc+1
Lh = Lc
xp = xp+1
yp = yp+1
Lp
xw1=xw1+1

```

```

yw1=yw1+1
Lw1
xw=xw+1
yw=yw+1
Lw

```

Filters.mat

```

% Image filters:
% 4-connected neighborhood averaging
% 8-connected neighborhood averaging
% Median filter
% Wiener filter
function [fm1, fm2, fmd, fw] = filters(a)

```

```

dim = length(a);
maxa = max(a');
mina = min(a');
M = maxa(1);
N = maxa(2);
minx = mina(3);
maxx = maxa(3);
c(M,N) = zeros;
delta = maxx-minx;

```

```

% Normalize the pixel intensity
for count=1:dim
    x=a(1,count);
    y=a(2,count);
    c(x,y) = (a(3, count)-minx)/delta*1.0;
end
[counts,x] = imhist(c,60);
figure(1)
stem(x,counts);

```

```

% Local averaging masks
mask1 =[0, 0.2, 0; 0.2, 0.2, 0.2; 0, 0.2, 0];
mask2 =[0.0625,0.125, 0.0625;0.125,0.125,0.125;0.0625,0.125,0.0625];

```

```

ee= conv2(c, mask1);
ff= conv2(c, mask2);
cc= medfilt2(c);
dd= wiener2(c);

```

```

cm(M-2,N-2) = zeros;

```

```

dm(M-2,N-2) = zeros;
em(M-2,N-2) = zeros;
fm(M-2,N-2) = zeros;

% Eliminate distorted image values
for countm=1:M-2
    for countn=1:N-2
        cm(countm,countn) = cc(countm+1, countn+1);
        dm(countm,countn) = dd(countm+1, countn+1);
        em(countm,countn) = ee(countm+1, countn+1);
        fm(countm,countn) = ff(countm+1, countn+1);
    end
end

figure(2)
subplot(2,2,1)
x=1:M-2;
y=1:N-2;
meshc(em);

subplot(2,2,2)
x=1:M-2;
y=1:N-2;
meshc(fm);

subplot(2,2,3)
x=1:M-2;
y=1:N-2;
meshc(cm);

subplot(2,2,4)
x1=1:M-2;
y2=1:N-2;
meshc(dm);

dimout=(M-2)*(N-2);

cmo(3,dimout) = zeros;
dmo(3,dimout) = zeros;
emo(3,dimout) = zeros;
fmo(3,dimout) = zeros;

% Output filtered images
for countm=1:M-2
    for countn=1:N-2
        x = (countn-1)*(M-2) + countm;

```

```

    cmo(1,x) = countm;
    cmo(2,x) = countn;
    cmo(3,x) = cm(countm, countn);
    dmo(1,x) = countm;
    dmo(2,x) = countn;
    dmo(3,x) = dm(countm, countn);
    emo(1,x) = countm;
    emo(2,x) = countn;
    emo(3,x) = em(countm, countn);
    fmo(1,x) = countm;
    fmo(2,x) = countn;
    fmo(3,x) = fm(countm, countn);
end
end

```

```

outl=fopen('finalmean1.txt','w');
fprintf(outl,'%d %d %d\n',emo);
fclose(outl);

```

```

outk=fopen('finalmean2.txt','w');
fprintf(outk,'%d %d %d\n',fmo);
fclose(outk);

```

```

outm=fopen('finalmedian.txt','w');
fprintf(outm,'%d %d %d\n',cmo);
fclose(outm);

```

```

outn=fopen('finalweiner.txt','w');
fprintf(outn,'%d %d %d\n',dmo);
fclose(outn);

```

```

fm1 = em;
fm2 = fm;
fmd = cm;
fw = dm;

```

Segmentation.mat

```

% Image segmentations
function [Hobj,Lobj] = segmentation(cm)

```

```

[M,N] = size(cm);

```

```

cm1(M,N) = zeros;
cm2(M,N) = zeros;
cm3(M,N) = zeros;

```

```

% Iterative thresholding selection
avg2 = 0;
avg1 = 1;
avg = mean(mean(cm));
avgold = 0;
n1 = 0;
n2 = 0;
ttl1 = 0;
ttl2 = 0;
NN = 0;

while abs(avg-avgold)>0.00001
for countm=1:M
    for countn=1:N
        if cm(countm, countn) > avg
            n1 = n1 +1;
            ttl1 = ttl1 + cm(countm, countn);
        else
            n2 = n2+1;
            ttl2 = ttl2 + cm(countm, countn);
        end
    end
end
avg1 = ttl1/n1;
avg2 = ttl2/n2;
avgold = avg;
avg = (avg1+avg2)/2;
n1 = 0;
n2 = 0;
ttl1 = 0;
ttl2 = 0;
NN = NN +1;
end

% Image segmentation
for countm=1:M
    for countn=1:N
        if cm(countm, countn) > avg1
            cm1(countm,countn) = cm(countm, countn);
        else if cm(countm, countn) < avg2
            cm2(countm,countn)=cm(countm, countn);
        else
            cm3(countm,countn)=cm(countm, countn);
        end
    end
end

```

```
end
```

```
for countm=1:M
    for countn=1:N
        if cm2(countm, countn) == 0
            cm2(countm,countn) = avg2;
        end
        if cm1(countm, countn) == 0
            cm1(countm,countn) = avg1;
        end
    end
end
end
```

```
figure(3)
subplot(3,1,1)
x=1:M;
y=1:N;
meshc(cm1);
```

```
subplot(3,1,2)
x=1:M;
y=1:N;
meshc(cm2);
```

```
subplot(3,1,3)
x=1:M;
y=1:N;
meshc(cm3);
```

```
% Output segmented images
dimout=M*N;
```

```
cmo1(3,dimout) = zeros;
cmo2(3,dimout) = zeros;
cmo3(3,dimout) = zeros;
for countm=1:M
    for countn=1:N
        x = (countn-1)*(M) + countm;
        cmo2(1,x) = countm;
        cmo2(2,x) = countn;
        cmo2(3,x) = cm2(countm, countn);
        cmo3(1,x) = countm;
        cmo3(2,x) = countn;
        cmo3(3,x) = cm3(countm, countn);
        cmo1(1,x) = countm;
```



```

        cmol(2,x) = countn;
        cmol(3,x) = cm1(countm, countn);
    end
end

```

```

Hobj = cm1;
Lobj = cm2;

```

```

outsegHobj=fopen('finalsegHobj.txt','w');
fprintf(outsegHobj,'%d %d %d\n',cmol);
fclose(outsegHobj);

```

```

outsegLobj=fopen('finalsegLobj.txt','w');
fprintf(outsegLobj,'%d %d %d\n',cmo2);
fclose(outsegLobj);

```

```

outsegback=fopen('finalsegback.txt','w');
fprintf(outsegback,'%d %d %d\n',cmo3);
fclose(outsegback);

```

```

end

```

SurfaceFeatureRemoval.mat

```

clear
close all

```

```

% Input uncollimated detector image
fidA=fopen('D:\research\dissertationDATA\mine wood\Surfer\detect3_Surfer_mine wood.txt');
a=fscanf(fidA, '%f', [3, inf]);
fclose(fidA);
% Input collimated detector image
fidB=fopen('D:\research\dissertationDATA\mine wood\Surfer\detect2_Surfer_mine wood.txt');
b=fscanf(fidB, '%f', [3, inf]);
fclose(fidB);

```

```

% Normalize the images and using image addition and subtraction
% with empirical coefficients to execute surface feature removal
dimA=length(a)
c(3,dimA)=zeros;
Avec=max(a');
M = Avec(1);
N = Avec(2);
maxA=Avec(3);
Avec=min(a');
minA=Avec(3);

```

```

Bvec=max(b');
maxB=Bvec(3);
Bvec=min(b');
minB=Bvec(3);
dataC=zeros(M,N);
dataD=zeros(M,N);
for count=1:dimA
    c(1,count)=b(1,count);
    c(2,count)=b(2,count);
    d(1,count)=b(1,count);
    d(2,count)=b(2,count);
    val1=(b(3,count)-minB)/(maxB-minB)*255;
    val2=(a(3,count)-minA)/(maxA-minA)*255;
    c(3,count)=val1- val2;
    d(3,count)=val1+val2;
    i=a(1,count);
    j=a(2,count);
    dataC(i,j)=c(3,count);
    dataD(i,j)=d(3,count);
end

```

```

x=1:M;
y=1:N;
meshc(dataC);

```

```

x=1:M;
y=1:N;
meshc(dataD);

```

```

outm=fopen('Add.txt','w');
fprintf(outm,'%f %f %f\n',c);
fclose(outm);

```

```

outd=fopen('Subtract.txt','w');
fprintf(outd,'%f %f %f\n',d);
fclose(outd);

```

Shifting.mat

```

% Lateral migration shifting calculation and object center location
% Algorithm1: Max intensity location
% Algorithm2: Geometric center location
% Algorithm3: Momentum center location

```

```

function [xc,yc,Lc,xp,yp,Lp,xw1,yw1,Lw1] = shifting(a, b)

```

```

maxa = max(max(a));
maxb = max(max(b));

[M,N] = size(a);

x1pa = 0;
x2pa = 0;
x1pb = 0;
x2pb = 0;

% Calculation of X coordinate of the geometric center
for countm=1:M
    for countn=1:N
        if x1pa == 0 & a(countm,countn) ~= 0
            x1pa = countm;
        end
        if x1pb == 0 & b(countm,countn) ~= 0
            x1pb = countm;
        end
    end
end

for countm=1:M
    for countn=1:N
        if x2pa == 0 & a(M-countm+1,countn) ~= 0
            x2pa = M-countm+1;
        end
        if x2pb == 0 & b(M-countm+1,countn) ~= 0
            x2pb = M-countm+1;
        end
    end
end

xa = abs(x1pa-x2pa)/2.0 + min(x1pa, x2pa);
xb = abs(x1pb-x2pb)/2.0 + min(x1pb, x2pb);
xp = floor(abs(xa-xb)/2.0 + min(xa,xb));

y1pa = 0;
y2pa = 0;
y1pb = 0;
y2pb = 0;

% Calculation of Y coordinate of the geometric center and
% Maximum intensity location
for countn=1:N
    for countm=1:M

```

```

    if maxa == a(countm, countn)
        xa = countm;
        ya = countn;
    end
    if y1pa == 0 & a(countm, countn) ~= 0
        y1pa = countn;
    end
    if maxb == b(countm, countn)
        xb = countm;
        yb = countn;
    end
    if y1pb == 0 & b(countm, countn) ~= 0
        y1pb = countn;
    end
end
end

for countn=1:N
    for countm=1:M
        if y2pa == 0 & a(countm, N-countn+1) ~= 0
            y2pa = N-countn+1;
        end
        if y2pb == 0 & b(countm, N-countn+1) ~= 0
            y2pb = N-countn+1;
        end
    end
end

xc = abs(xa-xb)/2.0 + min(xa, xb);
yc = abs(ya-yb)/2.0 + min(ya, yb);
Lc = abs(ya-yb);

ypa = abs(y1pa-y2pa)/2.0 + min(y1pa, y2pa);
ypb = abs(y1pb-y2pb)/2.0 + min(y1pb, y2pb);
yp = abs(ypa-ypb)/2.0 + min(ypa, ypb);
Lp = abs(ypa-ypb);

% Calculate moment center
ttla = 0;
ttlb = 0;
x = floor(xc);
for countn = 1:N
    ttla = ttla + a(x, countn);
    ttlb = ttlb + b(x, countn);
end

```

```

ttlbn = 0;
ttlbn = 0;

ttla = ttla/2.0;
ttlb = ttlb/2.0;
for countn = 1:N
    if ttlan < ttla
        ttlan = ttlan + a(x, countn);
    else
        ywa = countn;
        break;
    end
end

for countn = 1:N
    if ttlbn < ttlb
        ttlbn = ttlbn + b(x, countn);
    else
        ywb = countn;
        break;
    end
end

xw1 = x;
yw1 = abs(ywa-ywb)/2.0 + min(ywa,ywb);
Lw1 = abs(ywa-ywb);

```

Shifting2.mat

```

% Algorithm 4:
% Lateral migration shifting and object center location calculation by
% Multiple column moment averaging
function [xw,yw,Lw] = shifting2(a, b)

```

```

[M,N] = size(a);

x1pa = 0;
x2pa = 0;
x1pb = 0;
x2pb = 0;

% Calculation X coordinate of geometric center
for countm=1:M
    for countn=1:N
        if x1pa == 0 & a(countm,countn) ~= 0
            x1pa = countm;

```

```

        end
        if x1pb == 0 & b(countm,countn) ~= 0
            x1pb = countm;
        end
    end
end

for countm=1:M
    for countn=1:N
        if x2pa == 0 & a(M-countm+1,countn) ~= 0
            x2pa = M-countm+1;
        end
        if x2pb == 0 & b(M-countm+1,countn) ~= 0
            x2pb = M-countm+1;
        end
    end
end

xa = abs(x1pa-x2pa)/2.0 + min(x1pa, x2pa);
xb = abs(x1pb-x2pb)/2.0 + min(x1pb, x2pb);
x = floor(abs(xa-xb)/2.0 + min(xa,xb));

% Multiple column moment averaging to calculate Y coordinate
ttla = 0;
ttlbn = 0;
ttlal = 0;
ttlbl = 0;
ttlarn = 0;
ttlbrn = 0;
for countn = 1:N
    ttla = ttla + a(x, countn);
    ttlbn = ttlbn + b(x, countn);
    ttlal = ttlal + a(x-1, countn);
    ttlbl = ttlbl + b(x-1, countn);
    ttlarn = ttlarn + a(x+1, countn);
    ttlbrn = ttlbrn + b(x+1, countn);
end

ttlan = 0;
ttlbn = 0;
ttlaln = 0;
ttlbln = 0;
ttlarn = 0;
ttlbrn = 0;

ttla = ttla/2.0;

```

```

ttlbn = ttlbn/2.0;
ttlal = ttlal/2.0;
ttlbl = ttlbl/2.0;
ttlarn = ttlarn/2.0;
ttlbr = ttlbr/2.0;

for countn = 1:N
    if ttlan < ttla
        ttlan = ttlan + a(x, countn);
    else
        ywa = countn;
        break;
    end
end
for countn = 1:N
    if ttlaln < ttla
        ttla = ttla + a(x-1, countn);
    else
        ywal = countn;
        break;
    end
end
for countn = 1:N
    if ttla < ttla
        ttla = ttla + a(x+1, countn);
    else
        ywar = countn;
        break;
    end
end
ywa = (ywa + ywal + ywar)/3.0;

for countn = 1:N
    if ttlbn < ttlb
        ttlbn = ttlbn + b(x, countn);
    else
        ywb = countn;
        break;
    end
end
for countn = 1:N
    if ttlbln < ttlbl
        ttlbln = ttlbln + b(x-1, countn);
    else
        ywbl = countn;

```

```

        break;
    end
end
for countn = 1:N
    if ttlbrn < ttlbr
        ttlbrn = ttlbrn + b(x, countn);
    else
        ywbr = countn;
        break;
    end
end
end

ywb = (ywb + ywbl + ywbr)/3.0;

xw = x;
yw = abs(ywa-ywb)/2.0+min(ywa,ywb);
Lw = abs(ywa-ywb);

```

#### Recognition.mat

```

clear
close all

% Open template candidate image and
% image to be checked by template matching
fidA=fopen('c2052112.547');
[a, countn]=fscanf(fidA, '%f', [3,inf]);
fclose(fidA);

fidB=fopen('c2052012.457');
[b, countn]=fscanf(fidB, '%f', [3,inf]);
fclose(fidB);

% Image filtering
[ca1, ca2, cam, caw] = filters(a);
[cb1, cb2, cbm, cbw] = filters(b);

% Image Segmentation
[segobja, segbacka] = segmentation(cam);
[segobjb, segbackb] = segmentation(cbm);

% Template matching
M = Tmatching2(segobja, segobjb);

```



TemplateMatching.dat

% Template Matching to check existence of the object  
function mat = Tmatching2(a, b)

[M,N] = size(a);

% Defining image template from real mine image

% Calculate template length

x1pa = 0;

x2pa = 0;

x1pb = 0;

x2pb = 0;

for countm=1:M

for countn=1:N

if x1pa == 0 & a(countm,countn) ~= 0

x1pa = countm;

end

if x2pa == 0 & a(M-countm+1,countn) ~= 0

x2pa = M-countm+1;

end

end

end

y1pa = 0;

y2pa = 0;

y1pb = 0;

y2pb = 0;

% Calculate template width

for countn=1:N

for countm=1:M

if y1pa == 0 & a(countm,countn) ~= 0

y1pa = countn;

end

if y2pa == 0 & a(countm,N-countn+1) ~= 0

y2pa = N-countn+1;

end

end

end

xa = abs(x1pa-x2pa);

zx= min(x1pa,x2pa);

ya = abs(y1pa-y2pa);

zy= min(y1pa,y2pa);

% Create image template

```

▼▼▼▼dmc
dmc

$Sdlok`sd▼l`sbghmf▼sgqntfg▼mnql`khydc▼bqnrr▼bnqqdk`shnm
cw<▼L,w`*0:
cx<▼M,x`*0:
l`s<yqnr'cw+cx(:
sskbqn▼<▼/:
ssk`ts▼<▼/:
enq▼k<09cw
▼▼▼▼enq▼l<09cx
▼▼▼▼▼▼▼▼enq▼h<09w`
▼▼▼▼▼▼▼▼▼▼enq▼i<09x`
▼▼▼▼▼▼▼▼▼▼▼▼sskbqn▼<▼sskbqn▼*▼s'h+i()a'h*k,0+i*1,0(:
▼▼▼▼▼▼▼▼▼▼▼▼ssk`ts▼<▼ssk`ts▼*▼a'h*k,0+i*1,0()a'h*k,0+i*1,0(:
▼▼▼▼▼▼▼▼▼▼dmc
▼▼▼▼▼▼▼▼dmc
▼▼▼▼▼▼▼▼ssk`ts▼<▼

```

```
ldrgb'l`s(:
```

APPENDIX B  
LABVIEW MOTION CONTROL AND DATA ACQUISITION PROGRAM  
ILLUSTRATIONS

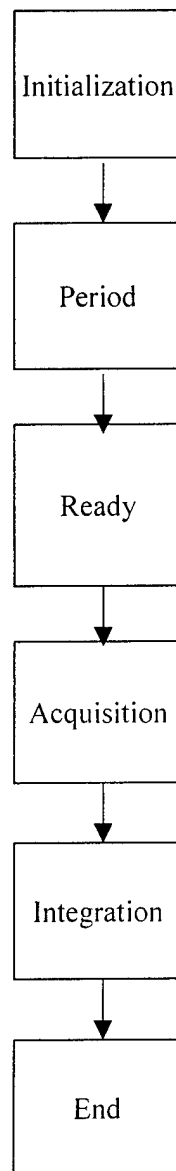


Figure C-1. Main program.

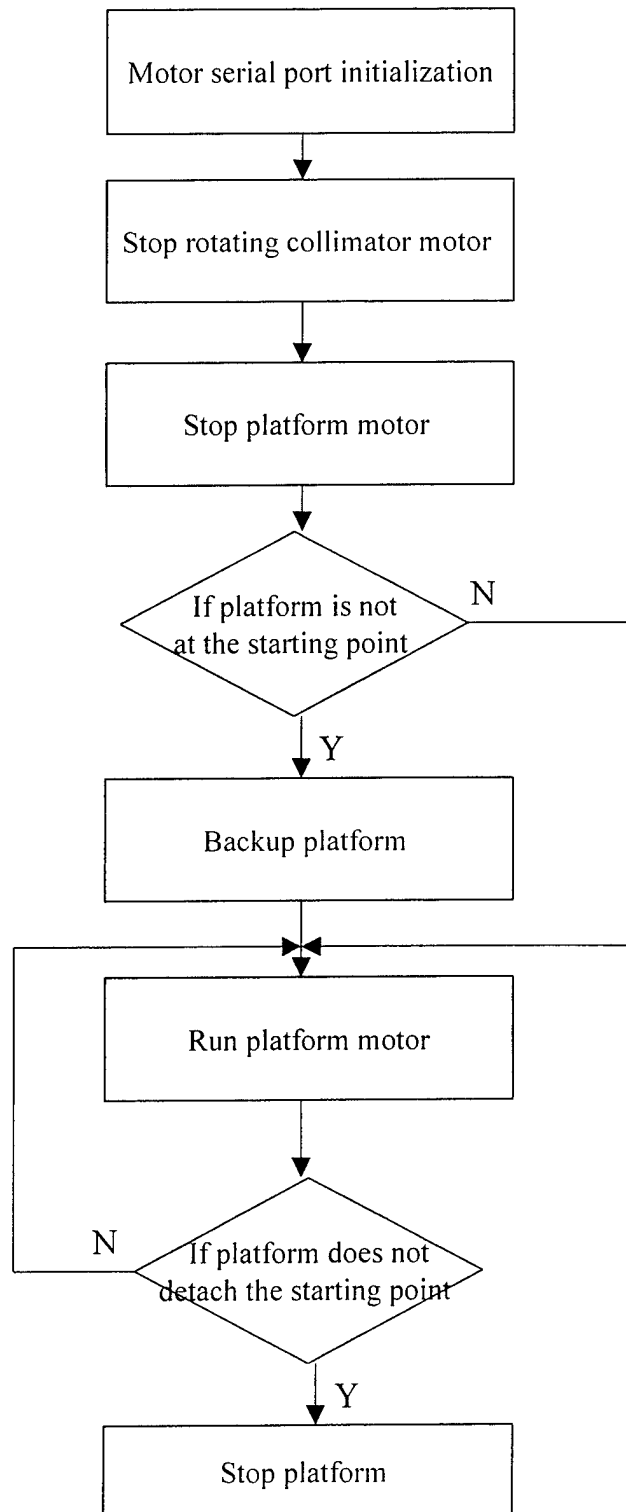


Figure C-2. Functions of initialization subroutine.

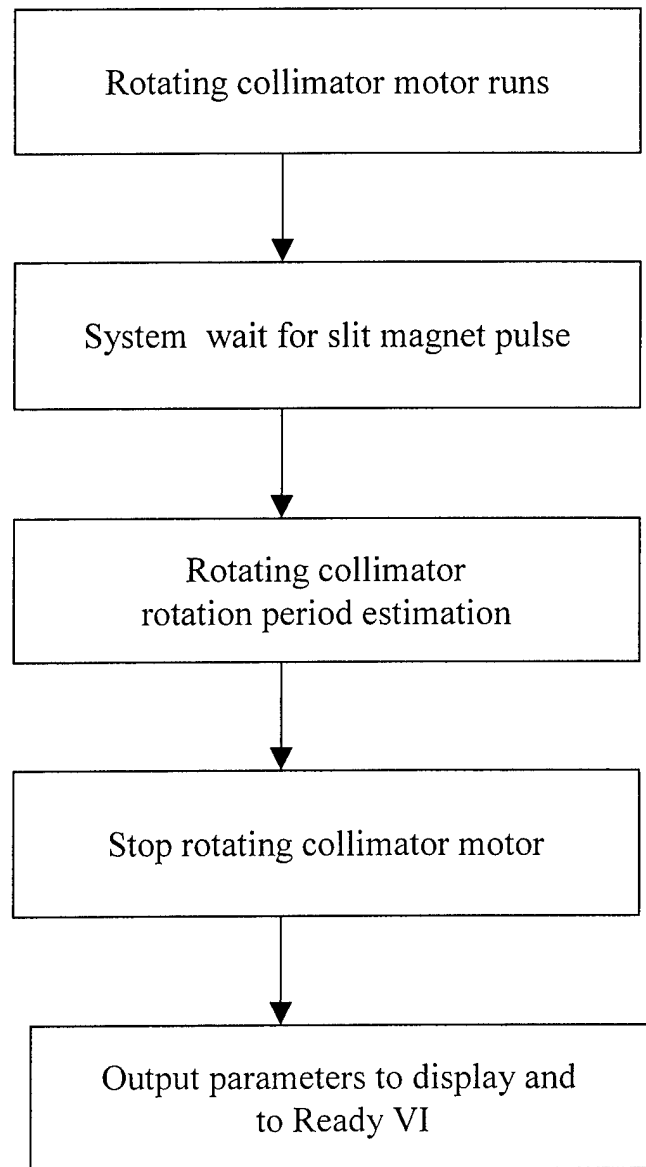
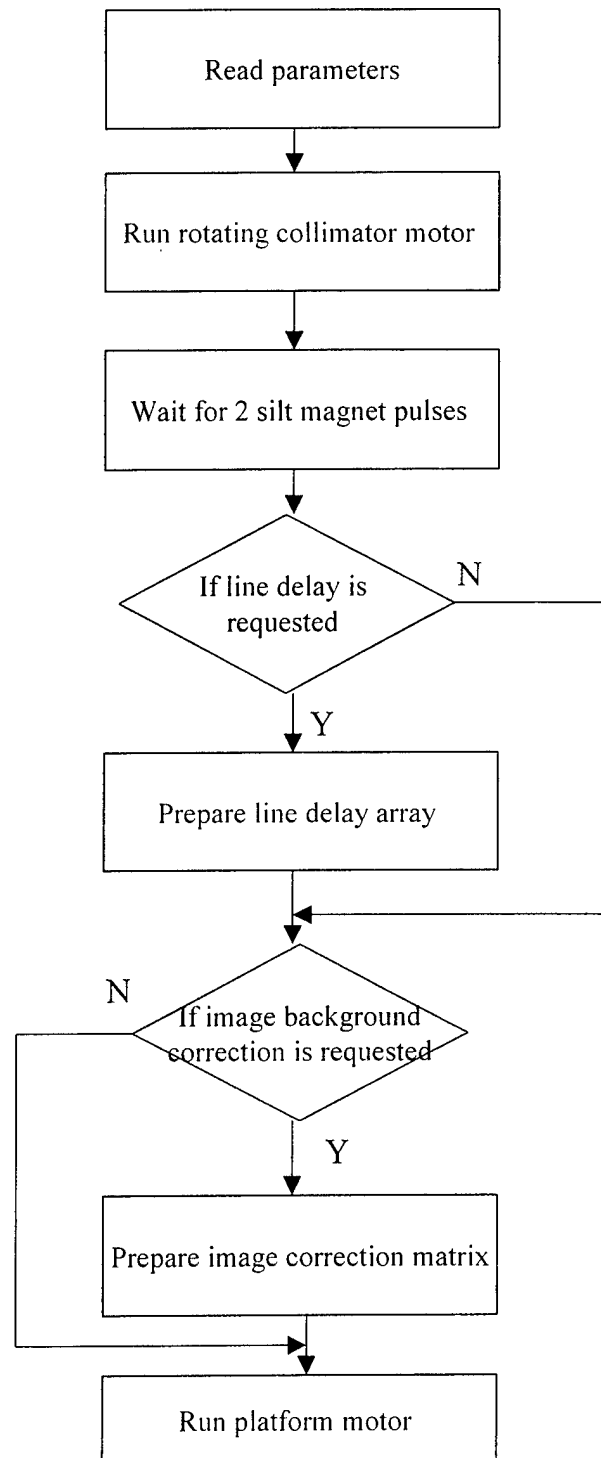


Figure C-3. Functions of period subroutine.



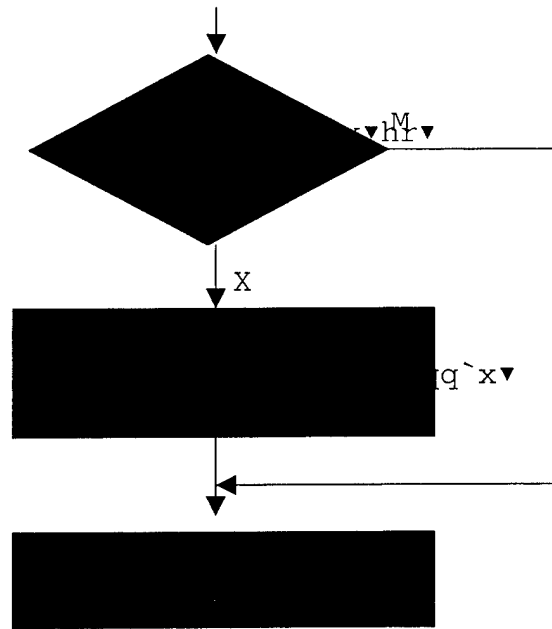
F:

F c t i o n s o f a d y s b o t





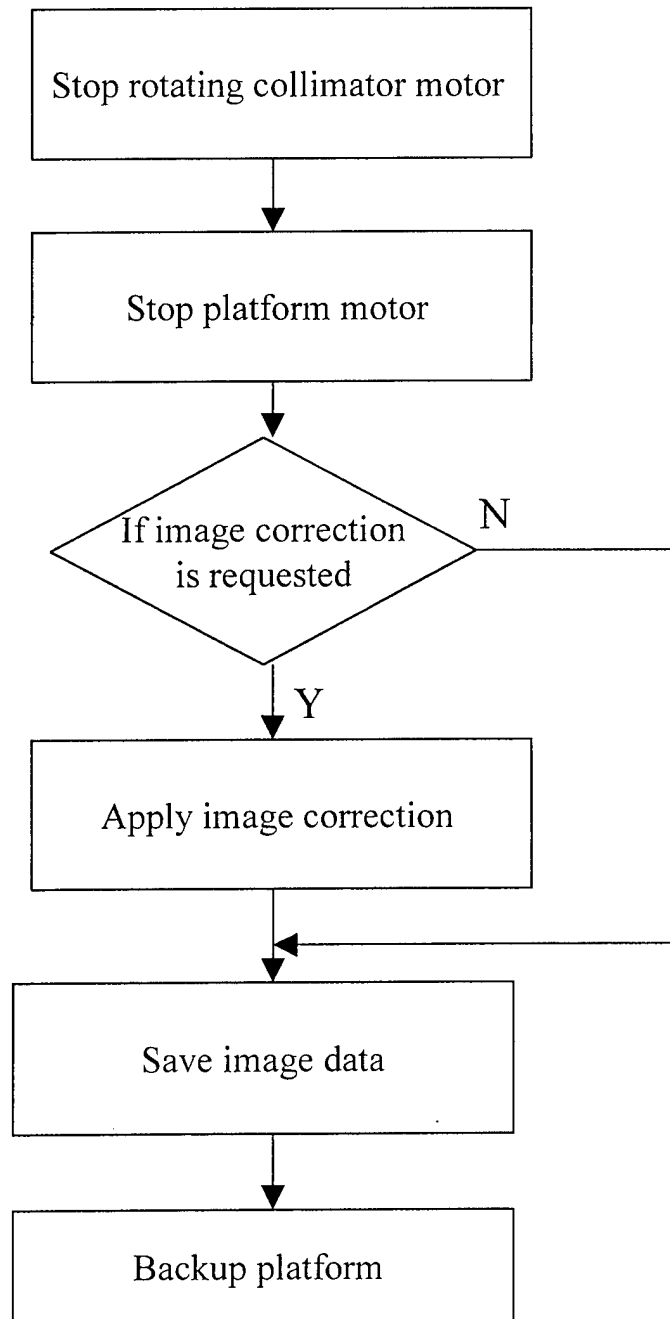
Qd`c▼o`q`ldsdqr



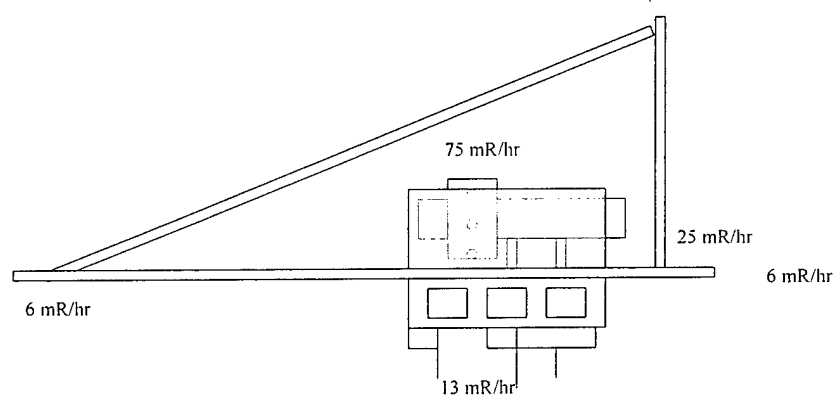
Qd`c▼o`q`ldsdqr

Ohwdk▼hmsdfq`shnm

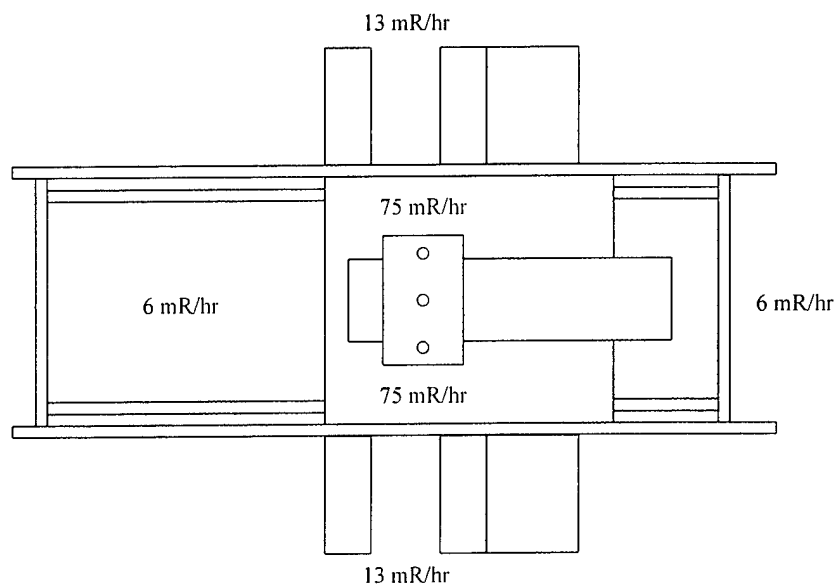




APPENDIX C  
RADIATION FIELD SURVEY OF THE LMR MOBILE FAST-SCAN MODULE



a



b

Figure B-1. Radiation field survey. a) Side view; b) Top view.

## APPENDIX D RASTER SCAN RESOLUTION IMPROVEMENT ALGORITHMS

Though the linear asymmetric algorithm discussed in Chapter 4 does improve the image resolution in the raster scan direction, it is not the best algorithm. An inverse filter technique and a least square solution are studied and a linear symmetric algorithm is developed based on a least square solution of a set of linear equations.

### Inverse Filter

During the data acquisition, data are acquired at a certain frequency  $f$ . Thus, the x-ray illumination spot newly covers a certain subpixel area. Imagining there is a datum  $x_i$  for each subpixel, the data  $d_i$  acquired for each raster line are the convolution of the x-ray illumination spot  $b$  to a train of data from each subpixel area.

$$d_i = \text{convolution}(x_i, b)$$

An inverse filter can be found through a Z-transform, its reciprocal and an inverse Z-transform to deconvolute the above process and recover the data from subpixels.

$$Z(d) = Z(x) Z(b)$$

$$Z(x) = Z(d)/Z(b)$$

$$Z^{-1}(x) = \text{convolution}(Z^{-1}(d), Z^{-1}(1/Z(b)))$$

$$x_i = \text{convolution}(d_i, Z^{-1}(1/Z(b)))$$

$Z(b) = (1 - z^{-1})/(1 - z^{-m})$ , where  $m$  is the number of pixel data points for width of a pixel.

$1/Z(b) = (1 - z^{-m})/(1 - z^{-1})$  is an IIR filter which needs to be truncated for computer calculation.

After acquiring the  $x_i$ , averaging them to get each pixel value is necessary. The pixel averaging is essentially a convolution and subsampling which each pixel value is essentially one measured datum of the raster line. However, since the system works almost at the photon statistical limit, each measured datum of the raster line is affected by the Poisson noise. Therefore, the inverse filter technique works only if noise free or very low noise data acquired from the system which is not the case of the developed system.

### Least Square Solution

Another algorithm, linear equation least square solution, provides a measurement data averaging template to improve the raster direction resolution. Dividing each raster line into a number of pixels of the size of the x-ray beam illumination spot, for each measured datum of the raster line, it is considered to be linear contribution from values from two adjacent pixels.

$$1*A + 0*B + 0*C + \dots + 0*Z = d_1 + n_1$$

$$0.9*A + 0.1*B + 0*C + \dots + 0*Z = d_2 + n_2$$

.....

$$0*A + 0*B + 0*C + \dots + 0.1*Y + 0.9*Z = d_{i-1} + n_{i-1}$$

$$0*A + 0*B + 0*C + \dots + 0*Y + 1*Z = d_i + n_i$$

$$C*V = D$$

where  $C$  is the coefficient matrix,  $V$  is pixel value vector and  $D$  is measurement data vector.

$$V = (A'A)^{-1}A'D \rightarrow V = PD, P \text{ is the pseudo-inverse matrix.}$$

Each row of matrix P is a template for data processing to improve image resolution in raster direction. Templates for the edge pixels may have boundary effect. The least square solution program and its acquired template are presented in the following section. The result shows that the template is a linear symmetric weighting template.

```
close all
%number of pixels in the calculation
n=31;
%number of moves from one pixel location the next
m=500;
%coefficient matrix
N=(n-1)*m+1;
A= zeros(N,n);
for i=1:N-1
    j=floor((i-1)/m)+1;
    A(i,j)=1-rem((i-1),m)*(1.0/m);
    A(i,j+1)=1-A(i,j);
end
A(N,n)=1;
r=rank(A)
%pseudo-inverse of coefficient matrix A
c=pinv(A);
%select middle pixel template, since no boundary effect
t=floor(n/2)+1;
plot(c(t,:), 'b')
```

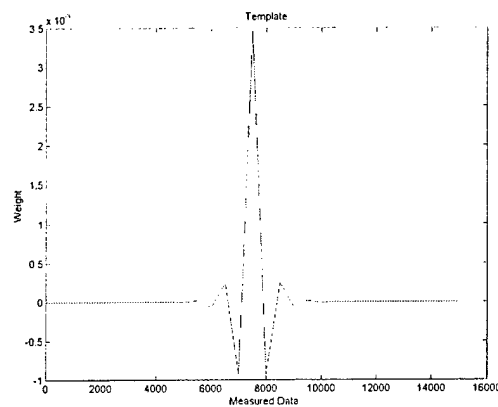


Figure D-1. Plot of the image template acquired through least square solution of a set of linear equations.

## REFERENCES

1. Campbell, J., Jacobs, A. M., "Detection of Buried Land Mines by Compton Backscatter Imaging," Nuclear Science and Engineering, 110, 417-424, 1992.
2. Harding G., Kosanetsky J., "Status and Outlook of Coherent X-ray Scatter Imaging," J Optical Society of America, A4 (5), 933-944, 1987.
3. Harding G., Kosanetsky J., "Scatter X-ray Beam Nondestructive Testing," Nuclear Instrumentation and Methods in Physics Research, A280, 517-528, 1989.
4. Herr M. D., McInerney J. J., Lamser D. G., Copenhaver G. L., "A Flying Spot X-ray System for Compton Backscatter Imaging," IEEE Transactions on Medical Imaging, 13 (5), 461-469, 1994.
5. Schonfelder V., Diehl R., Lichti G. G., Steinle H., "The imaging Compton Telescope COMTEL on the Gamma Ray Observatory," IEEE Transactions on Nuclear Science, NS-31 (1), 766-770, 1984.
6. Anghaie S., Baker A. G., Jacobs A.M., Kondic N. N., "Spatial Distribution of Phase in Flow Channels by Analysis of Compton Profile Measurements" in Measurements in Polyphase Flows, Ed., Hendrick T. R. and Patel B. R., ASME, New York, 13-17, 1982.
7. McInerney J. J., Lamser D. G., Herr M. D., "A Device for Non-invasive Evaluation of Coronary Bypass Grafts," IEEE Transactions on Medical Imaging, 13 (4), 658-665, 1994.
8. Su, Z., Jacobs, A., Dugan, E., Howly, J., Jacobs, J., "Lateral Migration Radiography Application to Land Mine Detection, Confirmation and Classification," Optical Engineering, 39 (9), 2472-2479, 2000.
9. Su, Z., Concept and Application of a Vehicle-mounted Land Mine Detection System Based on Lateral Migration Radiography, Master of Science Thesis, University of Florida, 1998.
10. Keshavmurthy, S., Development of a Lateral Migration Backscatter Radiography and Associated Image Enhancement Algorithms, Doctor of Philosophy Dissertation, University of Florida, 1996.

11. Watanabe Y., Monroe J., Keshavmurthy S., Jacobs A. M., Dugan E. T.,  
"Computational Methods for Shape Restoration of Buried Objects in Compton Backscatter Imaging," Nuclear Science and Engineering, 122, 55-67, 1996.
12. Jacobs, A., Dugan, E., "Landmine Detection by Scatter Radiation Radiography: Optimizing of Detector Array and Imaging Performance," Bi-monthly Performance and Cost Report for the Belvoir Research, Development and Engineering Center at Ft. Belvoir, Covering April, 1997 to May 1997.
13. Dugan E. T., "Analytical Calculations in Support of Research on a Land Mine Detection System Using Scatter Radiation Radiography," Scientific and Technical Final Report to U.S. Army Night Vision and Electronic Sensors Directorate, Covering December, 1992 to February 1995.
14. Fox, T. R., Jacobs, A. M., "Mobile X-ray Backscatter System for Underground Mine Detection," White Paper to U.S. Army Night Vision and Electronic Sensors Directorate, Bio-Imaging Research, Inc., 1996.
15. Briesmeister, J., "MCNP: A General Monte Carlo Code for Neutron and Photon Transport," Version 3A, LA-7396-M, Rev. 2, Los Alamos National Laboratory, 1987.
16. Fracke, T., An Analysis of Digital Filters Applied to Compton Backscatter Images, Master of Science Thesis, University of Florida, 1995.
17. Hanselman D., Littlefield B., The MATLAB: Version 4.0: User's Guide, Mathworks Inc., Prentice-Hall, Englewood Cliffs, NJ, 1995.
18. Jain, B., Kasturi, R., Schunck, B., Machine Vision, McGraw-Hill, Inc., New York, 1995.
19. Wehlburg, J., Development of a Lateral Migration Radiography Image Generation and Object Recognition System, Doctor of Philosophy Dissertation, University of Florida, 1997.
20. Jacobs, A., Dugan, E., "Landmine Detection by Scatter Radiation Radiography: Optimizing of Detector Array and Imaging Performance," Bi-monthly Performance and Cost Report for the Belvoir Research, Development and Engineering Center at Ft. Belvoir, Covering December, 1996 to January, 1997.
21. Jacobs, A., Dugan E., Moore, J., Su, Z., Wells, C., Ekdahl, D., Brandy, J., "Imaging Subsurface Defects Using X-ray Lateral Migration Radiography / A New Backscatter Technique," Proceedings of ANST Conference on Real-Time Radioscopy and Digital Imaging, 1999.

### **BIOGRAPHICAL SKETCH**

Zhong Su is from Beijing, China. He obtained his bachelor's degree in applied physics from the National University of Defense Technology, China. From 1992 to 1994, he worked in the Xinli Factory of the China Aerospace Industry Corporation as an engineer. From 1994 to 1996, he worked in Wogen Technology Ltd., Beijing Representative Office, as an engineer. He obtained his Master of Science degree in nuclear engineering (engineering physics option) in August of 1998. He will complete his Doctor of Philosophy degree in nuclear engineering (engineering physics option) in May of 2001.